Nuclear Fission Weapon Yield, Type, and Neutron Spectrum Determination Using Thin Li-ion Batteries

by

Taipeng Zhang

A Dissertation Presented in Partial Fulfillment
of the Requirements for the Degree
Doctor of Philosophy

Approved April 2017 by the
Graduate Supervisory Committee:

Keith Holbert, Chair
George Karady
Jiangchao Qin
Robert Metzger

ARIZONA STATE UNIVERSITY

May 2017

ABSTRACT

With the status of nuclear proliferation around the world becoming more and more complex, nuclear forensics methods are needed to restrain the unlawful usage of nuclear devices. Lithium-ion batteries are present ubiquitously in consumer electronic devices nowadays. More importantly, the materials inside the batteries have the potential to be used as neutron detectors, just like the activation foils used in reactor experiments. Therefore, in a nuclear weapon detonation incident, these lithium-ion batteries can serve as sensors that are spatially distributed.

In order to validate the feasibility of such an approach, Monte Carlo N-Particle (MCNP) models are built for various lithium-ion batteries, as well as neutron transport from different fission nuclear weapons. To obtain the precise battery compositions for the MCNP models, a destructive inductively coupled plasma mass spectrometry (ICP-MS) analysis is utilized. The same battery types are irradiated in a series of reactor experiments to validate the MCNP models and the methodology. The MCNP nuclear weapon radiation transport simulations are used to mimic the nuclear detonation incident to study the correlation between the nuclear reactions inside the batteries and the neutron spectra. Subsequently, the irradiated battery activities are used in the SNL-SAND-IV code to reconstruct the neutron spectrum for both the reactor experiments and the weapon detonation simulations.

Based on this study, empirical data show that the lithium-ion batteries have the

potential to serve as widely distributed neutron detectors in this simulated environment to (1) calculate the nuclear device yield, (2) differentiate between gun and implosion fission weapons, and (3) reconstruct the neutron spectrum of the device.

ACKNOWLEDGMENTS

First of all, I would like to express my deepest appreciation to my committee chair, Professor Keith Holbert. The past five years as your graduate student has been a precious journey that I will remember forever. You are always patient and nice to me. You taught me not only the methods to solve problems, but also how to be a qualified engineer and a better person, which will benefit me for life.

Thank you Dr. George Karady, Dr. Jiangchao Qin, and Dr. Robert Metzger for being my committee member. I appreciate all your suggestions and your valuable time.

I would also like to thank my colleagues, Dr. Eric Johnson, Tyler Stannard, and Anthony Christie for your contribution to this research. Thank you researchers at Oregon State University and University of Massachusetts Lowell for your assistance in the reactor experiments, and Dr. Stephen Romaniello for your support in the ICP-MS analysis.

Last, but not the least, I would like to thank my family. My parents Tongqin Zhang and Shuang Su, thank you for your generous support. It will be impossible for me to accomplish this without all your support. My wife Huijun Tan, thank you for your accompany all these years.

TABLE OF CONTENTS

Page

LIST OF TABLES vii

LIST OF FIGURES ix

LIST OF SYMBOLS xvi

CHAPTER

1 INTRODUCTION 1

2 BACKGROUND 5

2.1 Nuclear Forensics 5

2.2 Lithium-ion Battery as Radiation Detector 6

2.3 Activation Foils 7

2.4 JCO Criticality Accident 9

2.5 Post Detonation Analysis 10

2.5.1 Damage Zones 11

2.5.2 Brode Equation 13

2.5.3 Neutron Transport from Detonation 14

2.5.4 Monte Carlo Methodology 16

2.5.5 Gamma Spectroscopy 18

3 COMPOSITION AND MCNP MODELING OF LI-ION BATTERIES 20

CHAPTER Page

3.1 Battery Samples Information 21

3.2 Battery MCNP Models 25

4 REACTOR EXPERIMENTS 30

4.1 Battery Irradiation Experiments 30

4.2 MCNP Modeling of Battery Reactor Irradiation 36

4.3 Reactor Spectra Reconstruction 38

4.3.1 Reactor Spectra Reconstruction using Foil Results 39

4.3.2 First UMass Reactor Experiment Spectra Reconstruction using Battery Results 42

4.3.3 Second UMass Reactor Experiment Spectra Reconstruction using Battery Results 49

4.3.4 Summary 52

5 NUCLEAR WEAPON CHARACTERISTICS DETERMINATION 55

5.1 Nuclear Weapon Background 55

5.2 Nuclear Weapon Spectra Modeling 57

5.3 Nuclear Weapon Yield Calculation 61

5.4 Nuclear Weapon Spectra in Humid Air 64

5.5 Nuclear Weapon Type Determination 67

CHAPTER Page

5.5.1 Ratio Method 68

5.5.2 Slope Method 72

5.6 Nuclear Weapon Spectra Reconstruction 75

5.6.1 Weapon Spectra Reconstruction with Ultrathin Battery 76

5.6.2 Weapon Spectra Reconstruction with Thin Battery 79

5.6.3 Weapon Spectra Reconstruction with Combined Battery 81

5.6.4 Weapon Spectra Reconstruction with Battery Next to a Water Cube 84

5.7 Summary 88

6 CONCLUSIONS AND FUTURE WORK 89

REFERENCES 94

APPENDIX

A ICP-MS RESULTS FOR LI-ION BATTERIES 100

B GAMMA SPECTRA OF BATTERIES EXPOSED IN OSU EXPERIMENTS 106

C INDUCED ACTIVITIES FOR BATTERIES EXPOSED IN EXPERIMENTS 111

D ACTIVITY EQUATIONS DERIVATION 114

LIST OF TABLES

Table Page

2-1 Timeline of Nuclear Forensics after Nuclear Weapon Detonation 11

3-1 List of Batteries and Their Specifications. 21

3-2 ICP-MS Results for a ML-2020 $LiMnO_2$ Battery (in ppm) 23

3-3 Weight of Commonly Used Activation Foil Elements in Li-ion Batteries 24

4-1 Description of Four Reactor Experiments 31

4-2 Battery Model / Foils and Quantity Irradiated in Each Experiment 33

4-3 List of Foils Irradiated in UMass Experiments and Their Specifications 33

4-4 Induced Activities for Batteries Exposed in the First UMass Experiment 36

4-5 MCNP Simulation Results of the LIR2032 $LiCoO_2$ Battery in the Second OSU Experiment 38

4-6 SNL-SAND-IV Output for Foils in UMass Experiments 41

4-7 SNL-SAND-IV Output for Batteries from the First UMass Experiment 43

4-8 SNL-SAND-IV Output for the Combined MEC201 and ML-2020 Batteries from the First UMass Experiment 45

4-9 SNL-SAND-IV Output for Batteries from the Second UMass Experiment 49

4-10 Induced Activities for iPod and iPod Battery Exposed in the Second OSU Experiment 53

Table Page

4-11 Induced Activities for iPod and iPod Battery Exposed in the Second UMass Experiment..... 54

5-1 Density, Water Vapor Weight Percentage in Air, and MCNP Input Material Fraction for Different Humidity Levels..... 66

5-2 Total Fluence with and without $S(\alpha,\beta)$ Cross Section for Hydrogen in 100% Humidity for Little Boy and Fat Man Type Weapons at Different Distances..... 69

5-3 Activity Ratios of Selected Radionuclides at 1 km from Detonation Point from CR2032 $LiMnO_2$ Battery..... 69

6-1 Best Battery Choice to Determine Different Nuclear Weapon Features..... 92

LIST OF FIGURES

Figure Page

2-1. Different Damage Zones after a 10 kiloton Nuclear Weapon Detonation. 13

2-2. The Neutron Spectrum from ^{235}U Fission Reaction. 15

2-3. Flowchart of a Monte Carlo Calculation. 18

3-1. Disassembled Parts of ML-2020 Battery. 24

3-2. MCNP Geometry of the ML-2020 $LiMnO_2$ Battery. 26

3-3. MCNP Geometry of the MEC201 $LiCoO_2$ Battery. 27

3-4. MCNP Geometry of the CR2032 $LiMnO_2$ Battery. 28

3-5. MCNP Geometry of the LIR2032 $LiCoO_2$ Battery. 29

4-1. Gamma Ray Spectra of a CR2032 $LiMnO_2$ Battery Obtained 1 Day and 3 Days after the First OSU Reactor Experiment in the 10^{14} n/cm^2 Fluence, Counting Time of 1 Hour. 35

4-2. Relationship Between the Activity Level and the Irradiation Time. 40

4-3. SNL-SAND-IV Reconstructed Source Neutron Spectrum Comparison of the Two Experiments using Ten Activated Foils at the UMass FNI Facility. 41

4-4. SNL-SAND-IV Reconstruction of Source Neutron Spectrum Using Foils and Batteries in the First Experiment at UMass. 46

Figure Page

4-5. SNL-SAND-IV Reconstruction of Source Neutron Spectrum using Foils and Batteries in the First Experiment at UMass without Considering $^{58}Fe(n,\gamma)$ and $^{23}Na(n,\gamma)$ Reactions in the ML-2020 and the Combined Batteries. 48

4-6. SNL-SAND-IV Reconstruction of Source Neutron Spectrum Using Foils and Batteries in the Second Experiment at UMass. 50

4-7. $^{197}Au(n,\gamma)$ Cross Section. 51

5-1. Diagrams of Gun-Type and Implosion-Type Fission Nuclear Weapon Designs. 56

5-2. MCNP Simulation Geometry to Obtain the Nuclear Weapon Neutron Spectra from 0.2 to 2.5 km Away from the Source. 58

5-3. MCNP Simulated Neutron Spectra from a 10 kt Little Boy Type Device at Distances of 200 m and 800 to 1500 m from the Detonation Point. 59

5-4. MCNP Simulated Neutron Spectra from a 10 kt Fat Man Type Device at Distances of 200 m and 800 to 1500 m from the Detonation Point. 59

5-5. MCNP Simulated Neutron Spectra Comparison from 10 kt Little Boy and Fat Man Type Devices at 1000 m from the Detonation Point. 60

5-6. Comparison of Brode Equation Calculated and MCNP Computed total Fluence for 10 kt Little Boy and Fat Man Type Devices. 62

Figure Page

5-7. Comparison of Brode Equation Calculated and MCNP Computed total Fluence for 10 kt Little Boy and Fat Man Type Devices Along With Fits to the MCNP Results..... 63

5-8. Comparison of Brode Equation Calculated and MCNP Computed total Fluence for 10 kt Little Boy and Fat Man Type Devices in Dry Air, 20%, 40%, 60%, 80%, and 100% Humidity in Air. 66

5-9. $^{59}Fe/^{51}Cr$ Activity Ratio for 10 kt Little Boy and Fat Man Type Devices as a Function of Time 1 km from the Detonation Point. 70

5-10. $^{24}Na/^{51}Cr$ Activity Ratio for 10 kt Little Boy and Fat Man Type Devices as a Function of Distance One Day after Exposure. 71

5-11. Comparison of the total Number of $^{55}Mn(n,\gamma)$ Reactions as Computed By MCNP (Symbols), the Fitted Equation (Lines), and the total Fluence as a Function of Distance from 800 to 1500 m for 10 kt Little Boy and Fat Man Type Devices. 73

5-12. Comparison of the Slope of the Number of $^{55}Mn(n,\gamma)$ Reactions from 800 m to 1500 m for 10 kt Little Boy and Fat Man Type Devices in Dry, 20%, 40%, 60%, 80%, and 100% Humid Air. 75

Figure Page

5-13. Neutron Spectrum from SNL-SAND-IV Reconstruction of Fat Man Type Weapon from MEC201 Battery Using the MCNP Simulated Activities but Different Initial Spectra, With a Comparison to the MCNP Estimated Reference Weapon Spectra for 10 kt Little Boy and Fat Man Type Devices at 1 km. 78

5-14. Neutron Spectrum from SNL-SAND-IV Reconstruction of Little Boy Type Device from MEC201 Battery Using the MCNP Simulated Activities but Different Initial Spectra, with a Comparison to the MCNP Estimated Reference Weapon Spectra for 10 kt Little Boy and Fat Man Type Weapons at 1 km..... 79

5-15. Neutron Spectrum from SNL-SAND-IV Reconstruction of Little Boy Type Device from ML-2020 Battery Using the MCNP Simulated Activities but Different Initial Spectra, with a Comparison to the MCNP Estimated Reference Weapon Spectra for 10 kt Little Boy and Fat Man Type Weapons at 1 km. 80

5-16. Neutron Spectrum from SNL-SAND-IV Reconstruction of Fat Man Type Device from ML-2020 Battery Using the MCNP Simulated Activities but Different Initial Spectra, with a Comparison to the MCNP Estimated Reference Weapon Spectra for 10 kt Little Boy and Fat Man Type Weapons at 1 km. 81

Figure Page

5-17. Neutron Spectrum from SNL-SAND-IV Reconstruction of Little Boy Type Device from MEC201 and ML-2020 Combined Battery Using the MCNP Simulated Activities but Different Initial Spectra, with a Comparison to the MCNP Estimated Reference Weapon Spectra for 10 kt Little Boy and Fat Man Type Weapons at 1 km. 82

5-18. Neutron Spectrum from SNL-SAND-IV Reconstruction of Fat Man Type Device from MEC201 and ML-2020 Combined Battery Using the MCNP Simulated Activities but Different Initial Spectra, with a Comparison to the MCNP Estimated Reference Weapon Spectra for 10 kt Little Boy and Fat Man Type Weapons at 1 km. 83

5-19. MCNP Simulation Model of Battery Exposed in Weapon Spectrum with Water Cube. 84

5-20. Neutron Spectrum from SNL-SAND-IV Reconstruction of Little Boy Type Device from MEC201 Battery Using the MCNP Simulated Activities with and without Water Cube, with a Comparison to the MCNP Estimated Reference Weapon Spectra for 10 kt Little Boy and Fat Man Type Weapons at 1 km. 85

Figure Page

5-21. Neutron Spectrum from SNL-SAND-IV Reconstruction of Fat Man Type Device from MEC201 Battery Using the MCNP Simulated Activities with and without Water Cube, with a Comparison to the MCNP Estimated Reference Weapon Spectra for 10 kt Little Boy and Fat Man Type Weapons at 1 km. 86

5-22. Neutron Spectrum from SNL-SAND-IV Reconstruction of Little Boy Type Device from ML-2020 Battery Using the MCNP Simulated Activities with and without Water Cube, with a Comparison to the MCNP Estimated Reference Weapon Spectra for 10 kt Little Boy and Fat Man Type Weapons at 1 km. 87

5-23. Neutron Spectrum from SNL-SAND-IV Reconstruction of Fat Man Type Device from ML-2020 Battery Using the MCNP Simulated Activities with and without Water Cube, with a Comparison to the MCNP Estimated Reference Weapon Spectra for 10 kt Little Boy and Fat Man Type Weapons at 1 km. 87

B-1. Gamma Ray Spectra of a LIR2032 $LiCoO_2$ Battery Obtained 1 Day and 3 Days after the First OSU Reactor Experiment. 107

B-2. Gamma Ray Spectra of a LIR2032 $LiCoO_2$ Battery Obtained 1 Day and 2 Days after the Second OSU Reactor Experiment. 107

B-3. Gamma Ray Spectra of a CR2032 $LiMnO_2$ Battery Obtained 1 Day and 2 Days after the Second OSU Reactor Experiment. 108

Figure Page

B-4. Gamma Ray Spectrum of a MEC201 $LiCoO_2$ Battery Obtained 1 Day after the First UMass Reactor Experiment. 107

B-5. Gamma Ray Spectra of a ML-2020 $LiMnO_2$ Battery Obtained 1 Day after the First UMass Reactor Experiment. 107

B-6. Gamma Ray Spectra of a LIR2032 $LiCoO_2$ Battery Obtained 1 Day after the Second UMass Reactor Experiment.. 108

B-7. Gamma Ray Spectra of a CR2032 $LiMnO_2$ Battery Obtained 1 Day after the Second UMass Reactor Experiment.. 108

LIST OF SYMBOLS

A	Activity
R	Number of reactions
N	Number of atoms of the radioactive nuclide
t	Time
λ	Decay constant
Φ	Neutron fluence
Y	Weapon yield
r	Distance from the point of detonation
ρ	Density
n	Total number of target nuclei
ϕ	Steady-state neutron flux
σ	Microscopic capture (absorption) cross section
$\sum$	Macroscopic cross section
ϕ_T	Total neutron flux

CHAPTER 1

INTRODUCTION

With the threats by radical ideological groups and continued proliferation around the world, it is crucial to provide a deterrent to the use of nuclear weapons. Especially with the growing development of nuclear power all around the world, the propagation of nuclear materials raises people's concerns, because some of those nuclear materials could be used to manufacture a nuclear weapon. Even though countries such as the United States of America and the People's Republic of China which ratified the Treaty on Non-Proliferation of Nuclear Weapons are reducing their stockpiles, other nations are actively seeking to establish a nuclear arsenal. For example, by January 2016, North Korea has already carried out four nuclear weapons tests [1]. In May 2015, they claimed that they have the nuclear weapons that are capable of reaching the United States of America [2]. On one hand, leaders from fifty-six countries and international organizations joined together at the fourth Nuclear Security Summit 2016 hosted in Washington D.C. from March 31st to April 1st to reinforce the commitment at the highest levels to securing nuclear materials [3]. On the other hand, the supreme leader of North Korea, Kim Jung Un, ordered his country that their "nuclear warheads need to be ready for use at any time" in March 4th, 2016 [4] and more nuclear weapon tests should be conducted [5].

To develop and deploy a nuclear weapon is not an easy task. This means that multiple parties may participate in this process either purposely or unwittingly. Take the

terrorist organization Islamic State of Iraq and Syria (ISIS), which is actively seeking to acquire nuclear weapons, as an example. A report says that they have seized nearly 88 lbs of nuclear materials used for scientific research at a university in Mosul, Iraq [6], which could be used in developing nuclear weapons [7]. ISIS also claims that they are in a position to buy a nuclear weapon from Pakistan [8]. Therefore, it is essential to develop nuclear forensics methods that can pinpoint the source of a nuclear weapon.

Nuclear forensics are techniques that could determine the characteristics about the nuclear weapon, such as the yield, type, neutron spectrum, and manufacture in a weapon detonation incident. Therefore, adequate information could be provided for attribution to all parties for illegal activities. Lithium-ion batteries are potential tools that can accomplish these goals. This research originates the methods of using thin Li-ion batteries as widely distributed detectors to determine the type, yield, as well as the neutron spectrum of a nuclear device.

First in Chapter 2, background information about this research is presented.

Chapter 3 explains why Li-ion batteries are chosen as the detector in this research. The detailed information about the batteries that have been used in this research are also presented, including the preparation of the batteries for the inductively coupled plasma mass spectrometry (ICP-MS) analysis as well as their results. After that, three-dimensional MCNP computer models of these batteries are built and shown in this chapter as well.

In order to validate the approach of using irradiated batteries as sensors, multiple batteries and foils are irradiated in four reactor experiments, as discussed in Chapter 4. The MCNP models are also built to assess the experiments. The actual irradiated batteries are analyzed using gamma spectroscopy. The induced activities of irradiated foils are first used to reconstruct the reactor neutron spectra via the SNL-SAND-IV code. After that, the research focused on reconstructing the reactor neutron spectra using the battery activities. The results from foils and batteries are then compared to demonstrate the feasibility of using battery as the neutron detector.

The nuclear weapons information that this research extracted are presented in Chapter 5. MCNP Monte Carlo simulations are utilized to mimic a nuclear weapon detonation incident in an open space in dry air. The simulated neutron spectra at different distances from the point of detonation are plotted and compared for two different types of fission weapons. By using the MCNP weapon denotation simulations, two equations to calculate the yield for Little Boy and Fat Man type fission weapons are developed. The MCNP simulated results and equation calculated results are plotted and compared in order to examine the performance of the equations. After that, two different methods are demonstrated to determine fission nuclear weapon type by irradiating Li-ion batteries in the weapon neutron spectra using MCNP simulations. Lastly, these simulated irradiated batteries are used to reconstruct the incident neutron spectra. The SNL-SAND-IV

reconstructed results are compared with the reference spectra as well to validate the approach.

Lastly, Chapter 6 summarizes the current research work and proposes future works.

CHAPTER 2

BACKGROUND

This dissertation mainly focuses on using Li-ion batteries as a nuclear forensics tool to determine the nuclear weapon characteristics from a detonation incident. Therefore, in this chapter, basic information about nuclear forensics will be explained, as well as the rationale for using Li-ion batteries as radiation detectors. The long existing method of using activation foils as neutron detectors in reactor experiments, and studies pertaining to a nuclear fuel criticality accident are also presented. The principles as well as background information of post detonation analysis are also detailed in this chapter, including earlier efforts to calculate the weapon yield, neutron transport from detonation, fluence calculation from a point source, Monte Carlo methodology, gamma spectroscopy, and activity measurement.

2.1 Nuclear Forensics

Forensic science is a discipline that investigate substances involving criminal and civil laws by collecting, preserving, and analyzing scientific evidence [9]. Nuclear forensic science, which is often referred to as nuclear forensics, is a sub-subject of forensic science. It is defined as “the analysis of intercepted illicit nuclear or radioactive material and any associated material to provide evidence for nuclear attribution” [10]. In a specific nuclear weapon detonation incident, nuclear forensic methods could help officials to identify the

nuclear weapon characteristics, such as the yield, type and neutron spectrum, so that it could provide scientific evidence for the nuclear weapon attribution. The capability of nuclear forensics could also provide a deterrent to any individuals or groups who may intend to use nuclear materials in an illegal or immoral way [11].

In order to conduct nuclear forensics analysis, samples need to be collected and examined. Potential samples that could provide useful information includes radioactive materials, radiation contaminated items, biological samples, and environmental or geological samples [12]. This research chose to use irradiated Li-ion batteries as potential samples to perform nuclear forensics analysis. The massive presence of Li-ion batteries in consumer electronic devices assures the availability of samples at many locations, and a variety of distances from the detonation point after a nuclear explosion. With the assist of the advanced geography tools, such as the global positioning system (GPS), the coordinates of the battery samples can be pinpointed on a map accurately for later analysis. The detailed information and qualification of Li-ion batteries will be presented in Chapter 3.

2.2 Lithium-ion Battery as Radiation Detector

Prior to this work, a few other efforts have been performed to study the possibility of using Li-ion batteries as radiation detectors. Qiu et al. studied how the current of Li-ion batteries changes when exposed under radiation. They found out that as soon as the

batteries are placed or removed from near the radiation source, the current of the batteries changes instantaneously. They also discovered that the Li-ion batteries have different sensitivities to different radiation sources. Specifically, when exposed to gamma rays with a dose rate of 1.067 rad/h (reactor power 200 kW), the current increases ~40 pA through a 2.2 GΩ resistor; whereas when irradiated in a 3.8×10^{6} n/(cm^{2}·s) thermal neutron flux under the same reactor power, the current decreases ~5 pA [13].

Another research used cell phone (Li-ion) batteries as detectors to determine the retrospective thermal neutron fluence in a reactor [14]. According to Dorrell's research, the estimated thermal neutron fluences using activated battery samples have an average accuracy of 12%, compared to the actual fluences. He also found a highly linear relationship between the induced ^{60}Co activity in the irradiated cell phone batteries and the neutron fluence. This demonstrates that it is feasible to estimate thermal neutron fluence using Li-ion batteries exposed to neutrons.

All these previous works provide support for the concept of using Li-ion batteries as a nuclear forensics method after a nuclear weapon detonation incident.

2.3 Activation Foils

Long before this research studied whether Li-ion batteries can be used as neutron detectors, the method of using activated foils to measure neutron spectra was already well-established. Especially in nuclear reactor experiments, thin metal foils, such as Mg,

Al, Ti, Fe, Co, Ni, Cu, Zr, In, and Au, are typically utilized as detectors [15] [16]. Actually, most of the commonly used materials in the method can be found in the Li-ion batteries as well. Based on the activation foils methodology, the activity $A(t)$ of a radionuclide in an irradiated foil (as a function of the time t since starting the irradiation) can be calculated using [17],

$$A(t) = n\,\phi\,\sigma\,(1-e^{-\lambda t}) \tag{1}$$

where n is the total number of target nuclei that produce that radionuclide; ϕ is the steady-state neutron flux; σ is the microscopic capture (absorption) cross section of the target nuclide; and λ is the decay constant of the activation product. Usually, after the foil has been irradiated, it will be analyzed using gamma spectroscopy and thereafter, the activity can be calculated (details will be discussed later in section 2.5.5). Therefore, with the activity, radionuclide properties, foil mass, and decay time since the exposure terminated all known, the incident flux can be computed using the equation above.

In modern days, several computer based unfolding codes are available, such as SAND II. The SAND II code uses a computer automated iterative method to determine the neutron flux spectra by using measurement from activation foils [18]. By inputting the reaction types as well as the corresponding measured activities, SAND II can reconstruct the neutron spectrum. In this research, a beta version of updated SNL-SAND-IV is used, which will be discussed in detail in Chapter 4.

2.4 JCO Criticality Accident

In 1999, at Tokai-mura, Japan, a criticality accident occurred at a JCO Co. Ltd uranium conversion test plant. On September 30th, the accident happened when two workers (Mr. A and Mr. B) of the plant added more uranyl nitrate solution into a precipitation vessel than the critical solution mass. Neutrons and gamma-rays were generated uninterruptedly from the fission reactions for about nineteen hours before criticality could be stopped. As a result, those two workers were killed because of the deadly high amount of radiation dose. Another worker (Mr. C) who was working in the room next door was not killed onsite, however, he was exposed to a serious dosage [19].

After the accident, comparable efforts were made to assess the neutron dose caused by the accident. For example, by analyzing the victims' bone, blood, vomit, and urine, the amount of neutron doses that they were exposed to were calculated. Studies show that the estimated dose are >20 GyEq, 8 GyEq, and 3 GyEq for Mr. A, Mr. B, and Mr. C, respectively [20]. At the same time, the three victims' human body organs, such as tissue, hair, etc., as well as their personal items, such as belt buckle, coins found in the pocket, watch and its battery, etc., were measured using gamma spectroscopy analysis. The gamma spectrum detected from the watch battery, for example, showed that radionuclides such as ^{51}Cr, ^{54}Mn, ^{58}Co, ^{59}Fe, and ^{60}Co were present [20]. In another study, several 5-yen coin samples collected after the accident from the nearby buildings were utilized to evaluate the neutron dosage as well. The investigators found that the coins collected from different

locations can be used to estimate the neutron dose at the places where they were discovered [21]. These researches encouraged us to use Li-ion batteries as widely spread detectors, just like these coins, in a nuclear weapon denotation incident.

The study of this accident continued even more than two years later. Because of the longer half-life of ^{60}Co, spoons that had been irradiated by the accident were measured in years 2000 and 2001 to compute the accident neutron fluence. The results were compared with the earlier estimations using radionuclides that have shorter half-lives, such as ^{51}Cr and ^{59}Fe and they showed good agreement [22]. Similarly in our research, in irradiated Li-ion batteries, radionuclides such as ^{60}Co, which has a longer half-life (5.27 yr), as well as ^{51}Cr and ^{59}Fe, which are short-lived (27.7 days and 44.5 days, respectively), are also expected to be present. This means the suitable analysis time range of Li-ion batteries could be relatively wide, which is a big advantage.

2.5 Post Detonation Analysis

In a case of a nuclear weapon detonation, post detonation analysis should start within an hour to determine the nuclear weapon characteristics, as well as to help with rescue plans [23]. Table 2-1 shows a proposed typical post detonation analysis timeline. Usually, officials need to determine whether the explosion is from a nuclear device relatively quick (within one hour) so that a correct first aid response plan can be carried out. This can be done by, for example, measuring the radiation level in the environment to see if

it is abnormally high. Once it is confirmed that the incident is from a nuclear weapon, post detonation analyses should focus on classifying the characteristics of the nuclear weapon, including its type, yield and spectrum, chemical and physical signature. This could take days to weeks based on time needed to collect suitable samples, to prepare and perform the sample analyses, as well as the decay rates of different radionuclides. Once this has been done, it could take up to years to determine the attribution and assessment of further threat, based on the availability of the nuclear device data library. This means international cooperation and support is also important and desired in nuclear forensics.

Table 2-1 Timeline of Nuclear Forensics after Nuclear Weapon Detonation [23]

Timeline	Goal	Methods and Limitations
< 1 hour	Determine if the detonation is from nuclear weapon	Could measure the excess radiation level in a timely manner
Hours to weeks	Identify the signature characteristics, chemical and physical properties of the device	Due to time needed to collect samples, preparation for analyses, isotopes decay rates, and time needed for performing analyses
Hours to years	Attribution and assessment of further threat	Based upon availability of data bank

2.5.1 Damage Zones

In order to better perform the post denotation analyses later, it is very important to collect useful samples at reasonable distances. It is agreed by most experts that a 10 kiloton (kt) yield nuclear weapon is a useful assumption for research and planning purposes [24]. Therefore, this research is based on 10 kt nuclear weapons. After denotation of a 10 kt

nuclear weapon, the surrounding area can be divided into three different zones as shown in Figure 2-1:

1) Severe Damage (SD) Zone: the SD zone has a radius smaller than 0.8 km (0.5 miles) from the point of detonation (ground zero). Inside the SD zone, most things are expected to be destroyed by the blast of the explosion. Very few people would survive and a very high level of radiation is anticipated as well.
2) Moderate Damage (MD) Zone: the MD zone ranges from 0.8 km (0.5 miles) to 1.6 km (1 mile). Inside the MD zone, most objects will not be totally damaged by the blast and a significant amount of radiation is expected. Therefore, many of the people inside MD zone will survive and will benefit most if urgent medical treatment can be provided.
3) Light Damage (LD) Zone: the LD zone is the area that is more than 1.6 km (1 mile) away from the air zero. Limited physical damage is expected within this range and the radiation level is lower compared to the MD and SD zones.

This research will mainly focus on the distance range of 0.8 km to 1.5 km (inside the MD zone). Battery samples collected inside this zone are expected to be exposed to a high enough neutron flux to induce measurable activities for later analysis, yet they would not be overly physically damaged by the blast, nor be overly heated by the energy released from the weapon detonation. For a weapon that has a yield other than 10 kt, the MD zone distances will scale accordingly.

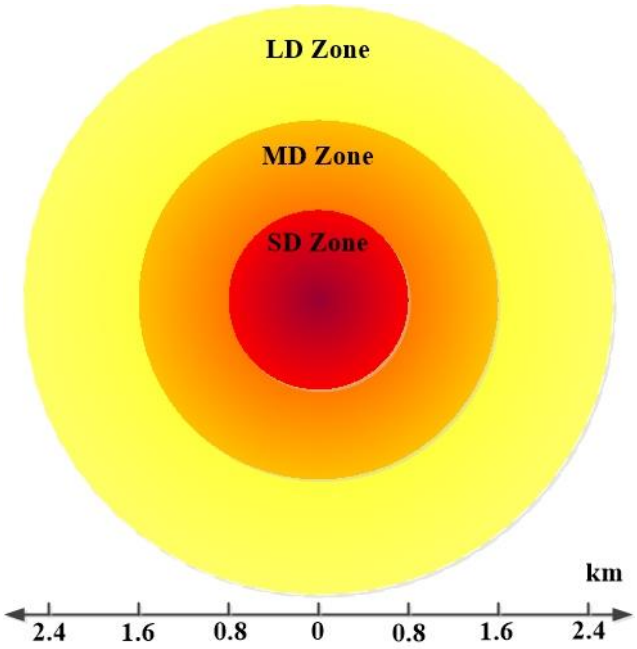

Figure 2-1. Different damage zones after a 10 kiloton nuclear weapon detonation [24].

2.5.2 Brode Equation

Efforts have been made throughout history to calculate the yield of a nuclear weapon. For example, in 1968, Brode related the weapon yield, neutron fluence, and distance from ground zero of a nuclear weapon to a rough approximation as shown below [25]:

$$\text{Brode}: \quad \Phi \cong \frac{\left(2\times10^{22}\ \text{n/kt}\right)Y}{r^2}\exp\left(\frac{-\rho r}{2.38\times10^{4}\ \text{g}\cdot\text{cm/L}}\right) \tag{2}$$

where Φ is the neutron fluence in neutrons/cm^2; Y is the weapon yield in kt; r is the distance from the point of detonation in cm; and ρ is the air density (~1.1×10^{-3} g/L). However,

Brode did not specify the type of nuclear weapon that he used to obtain this equation, and his antiquated equation only provides one significant digit. Since different types of nuclear weapons have different properties and characteristics, this provided an impetus for this research to develop separate equations for different weapon types with more significant digits, which will be presented in Chapter 5.

2.5.3 Neutron Transport from Detonation

When a fission nuclear weapon detonates, the heavy nucleus, such as ^{235}U, fissions, which releases a large amount of energy at the same time. The fission process also produces fission neutrons. These neutrons have different energies which distribute as shown in Figure 2-2. Note that the graph shows the neutron spectrum from ^{235}U fission reactions as an example. However, for other types of fissions, the spectra are similar with only slight changes. This spectrum is also called the Watt spectrum [26].

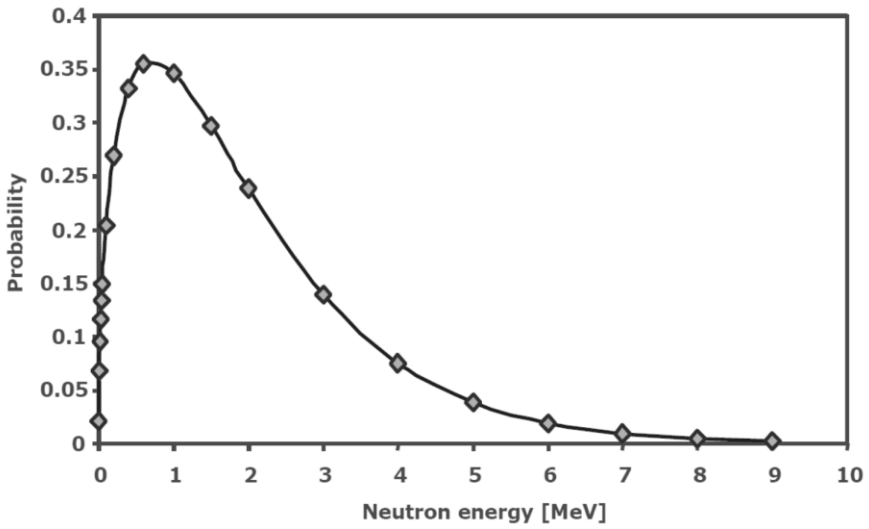

Figure 2-2. The neutron spectrum from ^{235}U fission reaction [27].

With the neutron source spectrum known, the uncollided fluence can be calculated using this attenuated point source model:

$$\Phi = \frac{S}{4\pi r^2} \exp(-\Sigma r) \tag{3}$$

where Φ is the neutron fluence; S is the source function; r is the radial distance from the source; and Σ is the macroscopic total cross section. By comparing Brode's equation (Eq. (2)) to the relation above, we recognize that Brode's equation also used this attenuated point source treatment with the presence of the air as the media. This is a reasonable assumption because by comparing the size of the nuclear weapon to the distances of interest (usually in kilometers), the weapon can be regarded as a point source. Therefore, in this dissertation, all the weapon sources are treated as point sources.

2.5.4 Monte Carlo Methodology

Monte Carlo methods are the many computational algorithms that are commonly used in solving complicated probabilistic problems. They utilize random numbers to obtain independent random samples from probability rules. They are mostly used to solve problems involving optimization, numerical integration, and generating draws from a probability distribution [28]. In order to make the Monte Carlo calculations more accurate, large numbers of high quality random numbers are desired. So far, there are mainly three different ways to get random numbers: 1) obtain samples from specially designed tables, 2) observe the output of random physical processes, or 3) calculate by applying certain mathematical algorithms [29]. The last method is generally used in today's computer based Monte Carlo calculations.

The Monte Carlo N-Particle (MCNP) transport code is a software package commonly used worldwide to simulate nuclear processes. It is developed and maintained by Los Alamos National Laboratory in New Mexico, USA. It is well designed to solve complicated three-dimensional problems. It applies the Monte Carlo method to analyze the transport of neutrons and gamma rays. It can also handle the coupled transport, as well as electron transport [30]. This research mainly focuses on the transport of neutrons after a nuclear weapon detonation.

Neutron transport studies the neutron movement and interactions with materials. It usually considers a straight line between different collision points. When a neutron collides

with another particle, it will be either 1) absorbed, or 2) scattered into another direction with a new energy level. The MCNP code can be used to simulate this transport process.

The input to MCNP includes: the source location and characteristics, the geometry, the material specification and corresponding cross section, tally or score type, etc. [31]. Figure 2-3 shows a simplified flowchart of how a Monte Carlo calculation works. It starts from the source where large numbers of particles (usually more than a million) are generated. Then, the particle track and history are computed, including its coordinates, direction, energy, and time (if needed), according to the source. Next, the path length to the next collision is selected using a random number. The geometry of the source, materials, and detectors must also be defined in the computer input prior to running the simulation. The cross sections of different materials need to be specified in the input as well. When a simulation starts, if a particle crosses the boundary of two materials, it is tallied or scored as part of the output calculation. However, if a particle goes through the outer boundary, then this particle has escaped. When the particle makes a collision, the computer decides if the particle is scattered or absorbed. If it is scattered, a new path (angle of scatter, direction, energy, etc.) is assigned using random numbers. If it is absorbed, this particle is tallied and the new source particle starts. Once all the particles have been processed, the program stops. Otherwise, a new particle is generated from the source to repeat this procedure, until all particles defined in the source term are used.

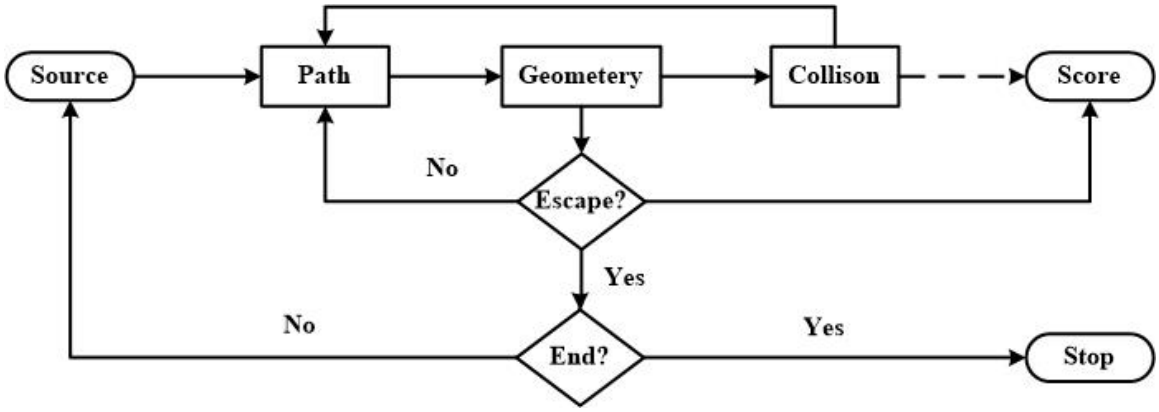

Figure 2-3. Flowchart of a Monte Carlo calculation [32].

2.5.5 Gamma Spectroscopy

Gamma spectroscopy studies the energy spectra of gamma-ray sources quantitatively. Once a nucleus has been irradiated to its excited state, it is possible for it to go through different decay modes, such as: beta decay, proton emission, alpha decay, fission, gamma ray emission, etc. In many cases, gamma ray emission is an important decay mechanisms. Therefore, a vast number of the radioactive elements emit gamma rays at different energy levels, as well as intensity, which can be measured by detectors. The results can be analyzed and produce a gamma spectrum. By studying the gamma spectrum, one can identify as well as quantify different radionuclides.

There are two general classes of radiation detectors: gas filled detectors, and solid state detectors. They utilize the ionization by radiation of the gas and solid material, respectively. Sodium iodide and germanium crystals are commonly used in solid state

detectors [33]. In our research, high purity germanium (HPGe) detectors are employed to measure the gamma spectra.

After the gamma spectrum has been measured by the detector, the activity (A) of the sample can be calculated using:

$$A = \frac{C}{\varepsilon \, \Delta t} \tag{4}$$

where C is the number of events detected by the detector in a period of time Δt, and ε is the efficiency of the detector [34]. The activity is defined as:

$$A = \frac{dN}{dt} = \lambda \, N \tag{5}$$

where N is the number of atoms of the radioactive nuclide, t is time, and λ is the decay constant [34]. In MCNP simulation, N can be tallied using the average cell flux tally (type F4) function. Therefore, the activity can be calculated by multiplying the decay constant.

CHAPTER 3

COMPOSITION AND MCNP MODELING OF LI-ION BATTERIES

Li-ion batteries are present extensively in consumer electronics nowadays. In fact, research shows that Li-ion batteries account for 80% of the global battery market share and the number is still growing [35]. They can be found inside the electronic devices, such as cell phones, watches, laptops, music players, electronic car keys, that people carry with them almost all the time. Also, with the development of the Li-ion battery technology, they are available in different sizes and shapes. They can be as thin as a foil, or as big as a building. Therefore, in the case of a nuclear weapon detonation incident, officials should be able to collect abundant samples in different sizes from a variety of distances from the detonation point for later forensic analyses. Also, materials such as Mg, Al, Fe, Co, Ni, Cu, etc., that are commonly used in the activation foils method are present in the Li-ion batteries as well. The half-lives of the radionuclides generated in the irradiated Li-ion battery range from hours to years, which gives a wide time window to the officials for the post detonation analyses. These facts provide justification for using Li-ion batteries as widely spread detectors for nuclear forensic analyses. In this chapter, detailed information about the Li-ion batteries being used in this research will be provided, as well as the preparation and the results of the inductively coupled plasma mass spectrometry (ICP-MS) in order to obtain the composition of the batteries. The MCNP battery models are also presented in this chapter.

3.1 Battery Samples Information

In this research, four different models of Li-ion batteries have been analyzed. Table 3-1 shows the detailed information about these batteries. The commonly used activation foils are usually disk shaped with masses ranging from 0.03 to 0.28 g, whereas the batteries are 1.4 to 100 times heavier. While the thickness of the MEC201 battery is within the thickness range of the foils (0.05 to 0.76 mm), the other three batteries are 2.6 to 64 times thicker compared to the foils.

Table 3-1 List of Batteries and Their Specifications.

Model No.	Type	Mass (g)	Shape	Dimensions (mm)
LIR2032	$LiCoO_2$	2.35	Coin Cell	D×H: 20.0×3.2
CR2032	$LiMnO_2$	3.00	Coin Cell	D×H: 20.0×3.2
ML-2020	$LiMnO_2$	2.30	Coin Cell	D×H: 20.1×2.0
MEC201	$LiCoO_2$	0.400	Thin Foil	L×W×H: 25.4×25.4×0.17

* D is diameter, H is height, L is Length, and W is width.

In order to obtain the accurate constituents of the Li-ion batteries, ICP-MS analysis was performed on each battery type. In order to prepare for the ICP-MS analysis, each battery was disassembled into parts. Each part was weighted by an electronic scale and measured by caliper to obtain the dimensions. Then, each part was dissolved into acids and the solution was used for ICP-MS analysis to acquire the mass (in ppm) of each chemical element in each part. The general detection limit of ICP-MS ranges between 0.01 to 0.00001 ppb depending on the analyte [36]. For example, the ICP-MS results for a

ML-2020 $LiMnO_2$ battery is shown as Table 3-2. Please note that only the elements with a concentration larger than 1 ppm are listed here, although other elements of lower concentration are also measured. This battery was disassembled into ten parts in total as shown in Figure 3-1, except for the electrolyte. The electrolyte evaporates once the battery is opened. Six out of the remaining nine parts were able to be dissolved into acids as shown in Table 3-2. The rest of the parts are separator, gasket, and plastic cover, which are made of organic compounds which are not measureable by ICP-MS. The ICP-MS results for the remaining three batteries listed in Table 3-1 can be found in Appendix A.

The ICP-MS results show that some of the most commonly used activation foil elements are also found in Li-ion batteries. Table 3-3 lists the weight percentage (wt%) of those elements inside the Li-ion batteries of interest. Those elements add up to 54% to 98% of the total weight of the four batteries we studied. Except for the MEC201 $LiCoO_2$ battery where Cu and Ni comprise the majority of the battery mass, Fe is the most abundant element (around 50%) in the other three batteries. Also, the mass fraction of a given element varies from one battery type to another. For example, the $LiCoO_2$ based batteries contain more Co compared to the $LiMnO_2$ based batteries; the LIR2032 and ML-2020 have more Al than the other two batteries. This indicates that in different post detonation analysis methods, certain types of Li-ion batteries may be more favorable compared to other types. Therefore, it is desired to collect a large variety of battery samples in a real nuclear weapon detonation incident to better assist latter post detonation analyses.

Table 3-2 ICP-MS Results for a ML-2020 $LiMnO_2$ Battery (in ppm)

Element	Panasonic Pellet	Positive Tab	Negative Tab	Metal Screen	Negative Casing	Positive Casing
MCNP Cell No.	4	1	9	7	8	2
Mass (mg)	36	11	8	18	68	84
Fe	BDL	1083796.50	914942.32	241749.35	723988.89	815287.16
Cr	BDL	269125.09	227349.07	61037.03	179927.42	186328.17
Mn	390000.00	14886.64	12344.82	13209.93	10062.45	2308.40
Al	BDL	166.35	161.12	706880.08	424.34	131.62
O	300000.00	BDL	BDL	BDL	BDL	BDL
Ni	BDL	146948.22	121810.03	39812.12	92664.12	3051.70
F	180000.00	BDL	BDL	BDL	BDL	BDL
C	120000.00	BDL	BDL	BDL	BDL	BDL
Mo	BDL	2735.35	2264.56	6954.11	1796.14	21276.68
Li	BDL	3.54	2.88	39170.31	80.65	26.83
Cu	BDL	4106.50	3386.14	850.51	3376.63	786.21
Co	BDL	1872.32	1551.96	835.61	1624.71	252.64
V	BDL	861.70	726.51	313.21	699.07	622.14
Sn	BDL	3173.36	5956.95	23.79	87.28	18.34
P	BDL	476.62	385.89	111.25	348.81	330.80
K	BDL	BDL	BDL	BDL	BDL	462.08
S	1000.00	BDL	BDL	BDL	BDL	BDL
Cl	750.00	BDL	BDL	BDL	BDL	BDL
W	BDL	201.89	165.79	101.74	319.76	13.67
Na	BDL	146.98	164.59	146.89	48.54	138.74
Ge	BDL	96.79	78.78	26.40	75.54	72.00
Ga	BDL	38.29	31.83	64.18	28.04	23.34
As	BDL	39.94	32.63	11.04	28.98	30.75
Sb	BDL	13.99	11.62	3.14	12.48	4.47
Ta	BDL	0.03	0.01	0.08	1.21	0.07
Au	BDL	0.76	0.56	0.34	0.29	0.31

* BDL: Below Detection Limit.

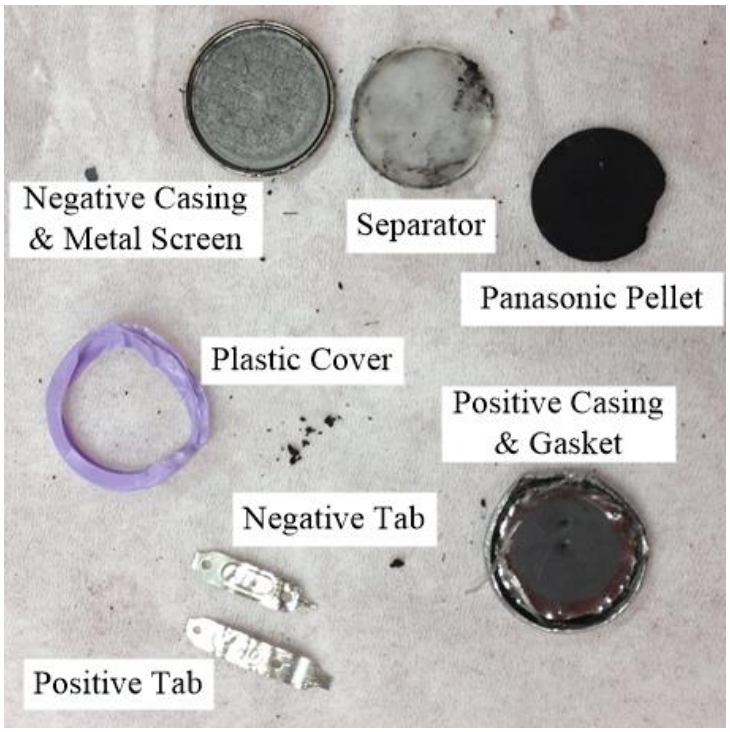

Figure 3-1. Disassembled parts of ML-2020 battery.

Table 3-3 Weight of Commonly Used Activation Foil Elements in Li-ion Batteries

Element	LIR2032 $LiCoO_2$	CR2032 $LiMnO_2$	ML-2020 $LiMnO_2$	MEC201 $LiCoO_2$
	Mass (mg) (wt%)	Mass (mg) (wt%)	Mass (mg) (wt%)	Mass (mg) (wt%)
Al	64 (2.7%)	1.0 (0.037%)	120 (5.2%)	0.41 (0.093%)
Ti	0.65 (0.027%)	0.076 (0.003%)	0.030 (0.001%)	0.55 (0.13%)
Fe	1100 (46%)	1500 (53%)	1300 (59%)	1.1 (0.25%)
Co	200 (8.7%)	0.16 (0.006%)	1.7 (0.074%)	6.2 (1.4%)
Ni	150 (6.2%)	28 (0.99%)	89 (3.9%)	130 (29%)
Cu	180 (7.7%)	0.22 (0.008%)	3.5 (0.16%)	300 (67%)

3.2 Battery MCNP Models

MCNP models for each of the batteries listed in Table 3-1 were built in order to perform later simulations. The input deck of the MCNP requires the definition of the following information:

1) Cell: the cell defines the geometry of the model. It defines which surfaces form each cell, as well as the material and its density in each cell.
2) Surface: the shape, whether it is a plane, cylinder, sphere, etc., and the coordinates of each surface is defined here.
3) Material: the detailed constituents of each material needs to be identified here. The weight or mole fraction, as well as the cross section information, of each nuclide inside the material needs to be defined. The cross section information can be chosen from the built-in library according to the appropriate conditions such as temperature, the maximum incident neutron energy, source library, and evaluation date.
4) Source: all the information about the source needs to be specified here, including the geometry and the location of the source, the type, direction, and number of the particles that the sources emits, as well as the spectrum of the source.
5) Tally: the type and the location of the desired tally is defined here. For example, a F4 tally measures the flux inside a certain cell, or a F2 tally detects flux on a

particular surface, etc. Multiple tallies of different types can be used, as there is no limitation of the number of the tallies that can be used.

During the preparation of the ICP-MS analysis, the geometry information of each battery is obtained. With the help of the ICP-MS, the detailed material information is also available. Therefore, MCNP battery models are able to be built. For example, Figure 3-2 shows the MCNP geometry of the ML-2020 $LiMnO_2$ battery presented in Section 3.1. The numbers in the figure represent each battery component, as well as the cell number in MCNP.

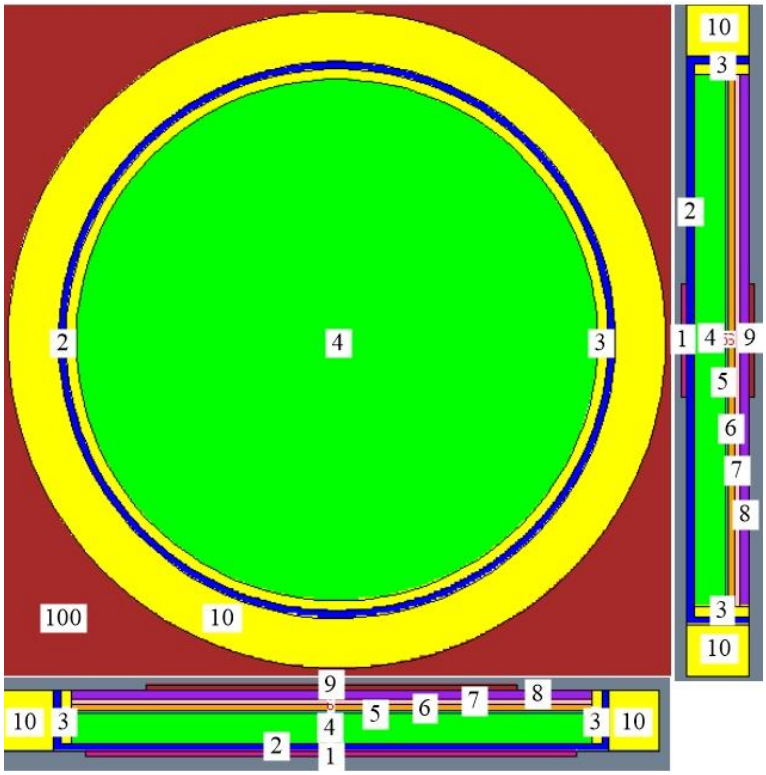

Figure 3-2. MCNP geometry of the ML-2020 $LiMnO_2$ battery.
Annotations in the diagram: 1 is the positive tab; 2 is the positive casing; 3 is the gasket; 4 is the Panasonic Pellet; 5 is the electrolyte; 6 is the separator; 7 is the metal screen; 8 is the negative casing; 9 is the negative tab; and 10 is the plastic cover. Material 100 is air.

The MEC201 is a foil like thin $LiCoO_2$ battery. The battery thickness is only 0.17 mm. The geometry of this battery is fairly simple. It was assembled as one thin green square sheet and one thin silver square sheet stacked together. The MCNP model for this battery is shown as Figure 3-3.

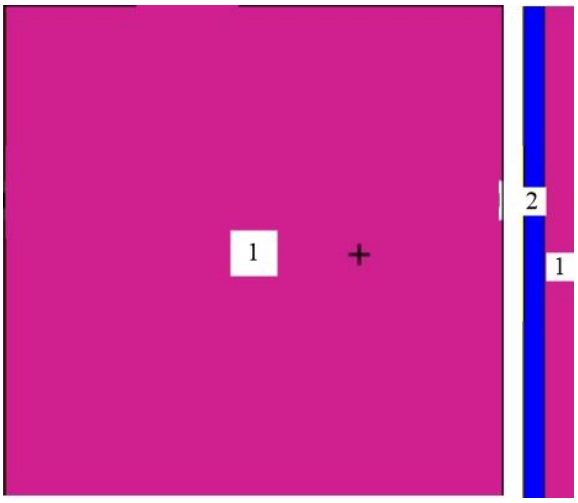

Figure 3-3. MCNP geometry of the MEC201 $LiCoO_2$ battery.
Annotations in the diagram: 1 is the silver side; and 2 is the green side.

The MCNP model for the CR2032 $LiMnO_2$ battery is shown as Figure 3-4. The CR2032 is also a coin cell sized battery. It was disassembled into nine parts as shown in the diagram. However, please note that there is a ring (cell number 2) around the MnO_2 (cell number 3) which is too thin to be seen in the figure.

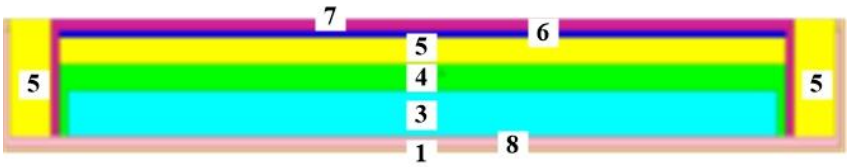

Figure 3-4. MCNP geometry of the CR2032 $LiMnO_2$ battery.
Annotations in the diagram: 1 is the positive casing; 3 is the MnO_2; 4 is the electrolyte; 5 is the separator; 6 is the lithium metal; 7 is the negative casing; and 8 is the gasket.

The geometry of the LIR2032 $LiCoO_2$ battery is a little challenging to construct because some of battery components, such as aluminum and copper foils, are wound together tightly. At first, all the elements from ICP-MS results were mixed together as a single whole homogeneous part. However, in order to minimize the difference between the MCNP simulation and later reactor experiments, a more accurate model was desired. Eventually, a "pie piece" heterogeneous model for the winding parts was used as a reasonable alternative scheme. The "pie piece" design kept the ability to build the geometry in a timely manner for the post detonation analysis, while maximally restoring the neutron self-shielding effect within the battery. Also, based upon the comparison of MCNP simulation results with the reactor experiment results from Chapter 4, the "pie piece" model is finally selected for use for this LIR2032 battery, as shown in Figure 3-5. The battery was disassembled into ten parts. Also note that not all parts can be seen in the figure because some parts, such as the aluminum foil (cell numbers 2) and the cobalt foil #1 (cell numbers 7), are too small to be seen in the diagrams.

With all the MCNP battery models built, they are ready to be used in later simulations. All that needed is to add the correct source information into the MCNP input

deck, for example the source of the reactor experiments, or the nuclear weapons, which will be presented in Chapters 4 and 5, respectively.

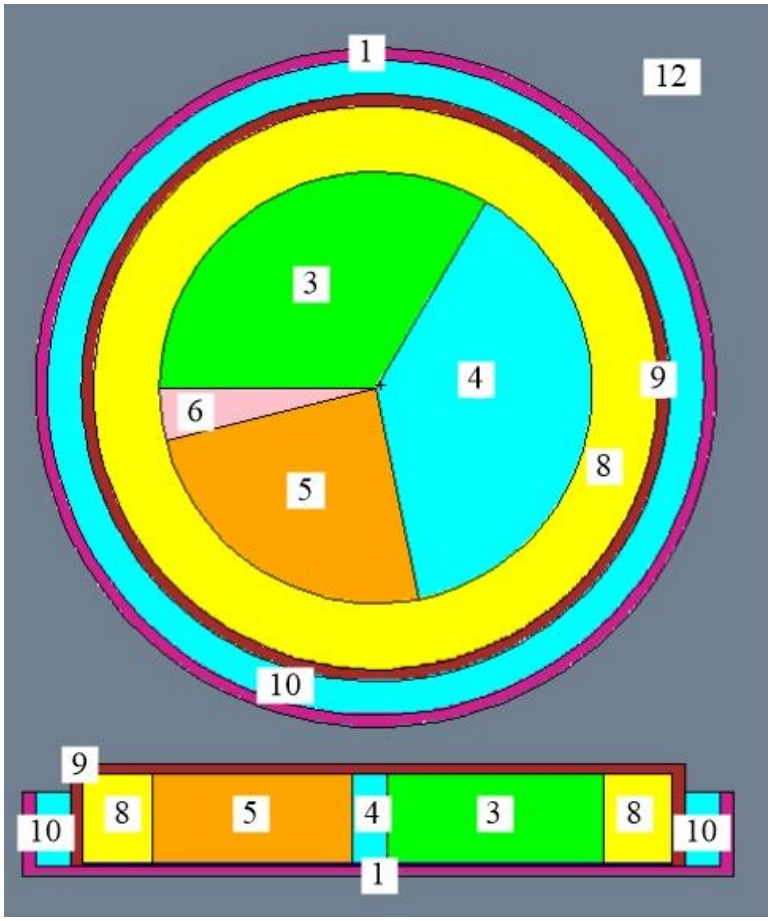

Figure 3-5. MCNP geometry of the LIR2032 $LiCoO_2$ battery.
Annotations in the diagram: 1 is the positive electrode; 3 is LiCo + cellulose and cobalt foil #2; 4 is the separator; 5 is the cathode; 6 is copper foil; 8 is the electrolyte; 9 is the negative electrode; and 10 is the gasket. Material 12 is air.

CHAPTER 4

REACTOR EXPERIMENTS

Since it is impractical to conduct a real nuclear weapon detonation for this research, several reactor experiments were performed in order to evaluate whether the activated batteries could be used as neutron detectors for post detonation analysis. This chapter presents detailed information about the reactor experiments. MCNP models with the reactor sources and the Li-ion batteries are also built to simulate the experiments. Lastly, the SNL-SAND-IV code is introduced and used to reconstruct the reactor spectrum using the activity of the irradiated batteries.

4.1 Battery Irradiation Experiments

Because it is unrealistic to perform experiments under a real nuclear weapon explosion situation, four reactor experiments were carried out. Two of the experiments were performed at the Oregon State University (OSU) TRIGA Reactor, while the remaining two tests were at the University of Massachusetts Lowell (UMass) Fast Neutron Irradiator (FNI). The OSU TRIGA Reactor is a water-cooled, pool-type research reactor that uses uranium/zirconium hydride fuel elements in a circular grid array. The reactor is capable of operating at a maximum steady state power of 1.1 MW and can also be pulsed up to a peak power of about 2000 MW [37]. The neutron facility at UMass is a 1-Megawatt research reactor producing thermal neutrons for radio-activation purposes and for digital

neutron radiography. Fast neutrons for atomic displacement research are produced by both the reactor and the 5.5 MV Pulsed van-de-Graaff accelerator [38]. The detailed information about the four experiments are listed in Table 4-1. During the experiments, the temperature of the samples are not expected to increase dramatically because of the relatively short irradiation period. Furthermore, for the OSU experiments, the TRIGA reactor is a pool-type water-cooled reactor, hence the moderator-coolant temperature is below 100°C.

Table 4-1 Description of Four Reactor Experiments

Location	Experi-ment	Facility	Maximum Neutron Flux [n/(cm^2·s)]			Irradiation Time
			Thermal	Epithermal	Fast	
Oregon State University	No. 1	TRIGA Reactor In-core Irradiation Tube	9.96×10^{12} $\pm1.95\times10^{12}$	2.23×10^{13} $\pm8.11\times10^{12}$	2.51×10^{13} $\pm4.75\times10^{12}$	27 mins
	No. 2	TRIGA Reactor Pneumatic Transfer Tube (Rabbit)	1.73×10^{13} $\pm3.03\times10^{12}$	5.91×10^{12} $\pm2.03\times10^{12}$	5.37×10^{12} $\pm9.52\times10^{11}$	30 sec
University of Mass-achusetts Lowell	No. 1	Fast Neutron Irradiator	4.85×10^{9}	2.45×10^{11}	1.83×10^{11}	1200 sec
	No. 2	Fast Neutron Irradiator	4.85×10^{9}	2.45×10^{11}	1.83×10^{11}	1235 sec

The four different types of Li-ion batteries presented in Chapter 3 were used as samples during the four reactor experiments, as shown in Table 4-2. In particular, during the first experiment at OSU, two LIR2032 $LiCoO_2$ and two CR2032 $LiMnO_2$ battery samples were irradiated in an in-core irradiation tube for 27 minutes, while the reactor was operated at 10 kW power level and generated a thermal neutron fluence of approximately 10^{14} n/cm^2. Later, in the second OSU experiments, those same models of (un-exposed) batteries were irradiated. This time, the reactor was operating at full power (1.1 MW), and the battery samples were put in a pneumatic transfer tube (rabbit) and exposed to the radiation for 30 seconds, to obtain the similar fluence level of 10^{14} n/cm^2, individually. In the first experiment performed at UMass, two ML-2020 $LiMnO_2$ and two MEC201 $LiCoO_2$ batteries were irradiated for 1200 seconds in the FNI. Two each of the LIR2032 $LiCoO_2$ and CR2032 $LiMnO_2$ battery types used in the OSU experiments were irradiated during the second UMass experiment for 1235 seconds. Because of safety considerations, all battery samples were fully discharged before being irradiated. Since the research is focused on neutrons, which are neutral, the charge status of the batteries should not affect the result. The detailed information about those four battery types can be found in Table 3-1.

Besides those batteries irradiated during the two UMass experiments, ten foils were also activated in each UMass experiment. The materials and the detailed specifications of the foils are listed in Table 4-3. All those foils are disk-shaped, with a diameter of 12.7 mm.

By comparing the weight and the thickness of the foils to the specifications of the batteries listed in Table 3-1, we find that the mass and size of the MEC201 battery are similar to that of the foils. However, the remaining three batteries are 8.2 to 100 times heavier, and 2.6 to 64 times thicker than the foils.

Table 4-2 Battery Model / Foils and Quantity Irradiated in Each Experiment

	First OSU Experiment	Second OSU Experiment	First UMass Experiment	Second UMass Experiment
LIR2032 $LiCoO_2$	2	1	N/A	2
CR2032 $LiMnO_2$	2	1	N/A	2
ML-2020 $LiMnO_2$	N/A	N/A	2	N/A
MEC201 $LiCoO_2$	N/A	N/A	2	N/A
Foils	N/A	N/A	10	10

Table 4-3 List of Foils Irradiated in UMass Experiments and Their Specifications

Material	Thickness (mm)	Mass (mg)
In	0.13	127
Au	0.051	125
Cu	0.13	142
Ti	0.25	140
Ni	0.25	283
Fe	0.13	138
Mg	0.13	31.8
Al	0.76	250
V	0.051	48.0
Zr	0.13	111

After each experiment, gamma spectroscopy analysis was performed for each of the batteries. High purity germanium (HPGe) detectors were used to measure the gamma spectra of the batteries after one to three days post irradiation. These time delays are chosen to lower the activity level of the batteries so that they are safer for the scientists to handle. This also mimics the expected time delay between the nuclear weapon explosion and the collection and measurement of the samples in a real detonation incident. As an example, Figure 4-1 shows the gamma ray spectra of a CR2032 $LiMnO_2$ battery obtained 1 day and 3 days after the first OSU reactor experiment. The day 1 spectrum shows that Na-24, Cr-51, Mn-56, and Fe-59 were clearly identified. The other peaks are caused by measurements effects such as X-rays, annihilation radiation, escape peaks and sum peaks. By comparing the two spectra we can see that after 3 days, the activity level is reduced significantly because of the decay of the shorter lived radionuclides. In the day 3 spectrum, radionuclides such as Mn-54, Co-58, Co-60, Mo-99 and W-187 were identified, while they were not readily distinguishable the first day. This means that for some battery types that produce radionuclides with longer half-lives, such as $LiCoO_2$ batteries that yield Co-60 with a 5.27 year half-life, a slightly longer delay could reveal more radioisotopes. Therefore, in an actual deployment, multiple measurements with different time delays may be needed to obtain complete information. The gamma spectra of other batteries exposed in the OSU and UMass experiments can be found in Appendix B.

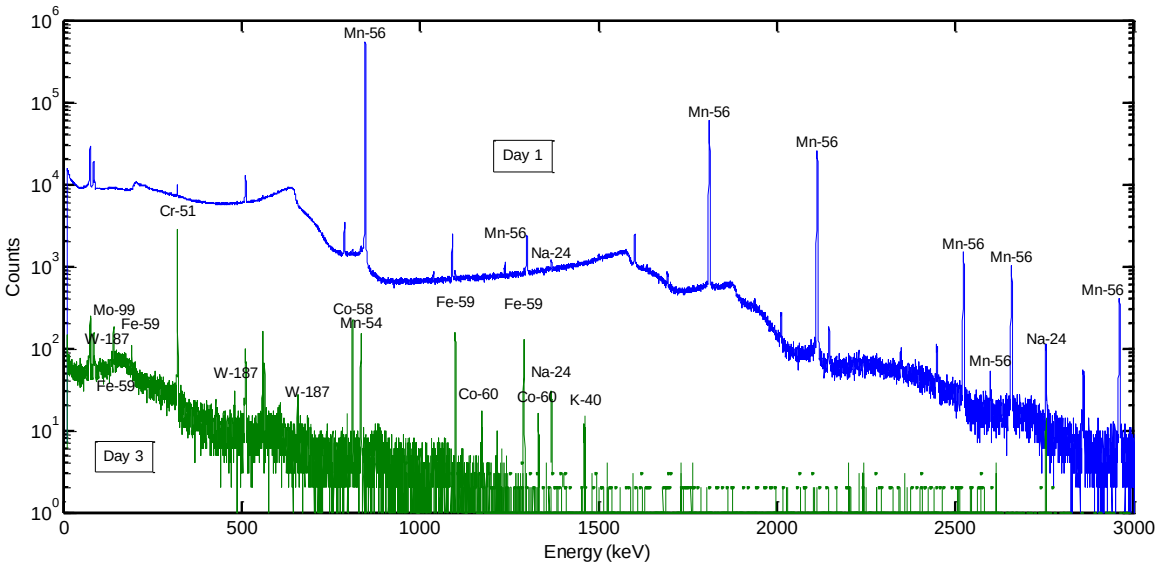

Figure 4-1. Gamma ray spectra of a CR2032 $LiMnO_2$ battery obtained 1 day and 3 days after the first OSU reactor experiment in the 10^{14} n/cm^2 fluence, counting time of 1 hour.

After obtaining the gamma spectra, an ASU researcher used the software PeakEasy [39] to identify and quantify the activities. For example,

Table 4-4 shows the induced activities measured for a MEC201 $LiCoO_2$ and a ML-2020 $LiMnO_2$ battery that were irradiated during the first UMass experiment using the gamma spectra measured 1 day after the exposure. From the table we can see that for the MEC201 battery, Cu-64 and As-76 are the most dominate radionuclides, whereas W-187, Mo-99, and Cr-51 have a higher activity in the ML-2020 battery. The measured induced activities for the other batteries and experiments can be found in Appendix C.

Table 4-4 Induced Activities for Batteries Exposed in the First UMass Experiment

Radionuclides	MEC201 $LiCoO_2$	ML-2020 $LiMnO_2$
	Activity (Bq)	Activity (Bq)
Au-198	2.03×10^{0}	3.11×10^{0}
Co-58	1.16×10^{2}	5.92×10^{1}
Co-60	5.14×10^{1}	1.02×10^{1}
Cu-64	4.14×10^{5}	N/A
As-76	4.77×10^{2}	N/A
Cr-51	N/A	4.40×10^{2}
Fe-59	N/A	1.76×10^{1}
Mn-54	N/A	1.39×10^{1}
Mo-99	N/A	1.55×10^{3}
Na-24	N/A	1.56×10^{2}
Nb-92m	N/A	1.76×10^{0}
Sb-122	N/A	3.67×10^{1}
Sb-124	N/A	5.25×10^{0}
Sn-117m	N/A	7.36×10^{-1}
W-187	N/A	1.69×10^{3}

4.2 MCNP Modeling of Battery Reactor Irradiation

With the MCNP battery models already built, as presented in Section 3.2, the reactor experiments are simulated in MCNP, using the reactor source spectra. The reactor source spectra were obtained from literature review [40] [41]. In the MCNP model, the neutron source was designed as an inward spherical distribution with a radius of 27.35 cm. The spherical distribution was chosen because it best reflects the reactor experiment irradiation environment, which neutrons travel from all directions to the samples. The radius was chosen to be 27.35 cm because it would fit all the battery samples inside, while leaving some space around. First, a point flux (F5) tally was placed in the center of the

sphere to verify the simulated flux. Then, using the experiment flux ϕ_1, initial simulated flux ϕ_2, and the initial simulation source weight wgt_2, the proper source weight $wgt_1$is calculated using:

$$\frac{\phi_1}{\phi_2} = \frac{wgt_1}{wgt_2} \tag{6}$$

This calculated source weight wgt_2 will be used in later MCNP simulations.

In order to ensure most of the ten MCNP statistics pass and to obtain a higher accuracy during the simulation, 300 million or more particle histories were used. With the help of the gamma spectra measured from the experiments, specific reactions were tallied using cell flux (F4) tallies. For example, Table 4-5 presents the MCNP simulation results of the LIR2032 $LiCoO_2$ battery during the second OSU experiment and corresponding activation product half-lives. Based on the (simulated) induced activities, reactions such as $^{27}Al(n,\gamma)^{28}Al$, $^{55}Mn(n,\gamma)^{56}Mn$, and $^{63}Cu(n,\gamma)^{64}Cu$ are the most dominate for this type of battery. However, radionuclides such as ^{28}Al and ^{56}Mn have a short half-life, less than 0.5 days as shown in the table. Therefore, judging from both induced activity and half-life standpoints, reactions such as $^{50}Cr(n,\gamma)^{51}Cr$, $^{58}Fe(n,\gamma)^{59}Fe$ and $^{59}Co(n,\gamma)^{60}Co$ are more favorable for the LIR2032 $LiCoO_2$ battery.

Table 4-5 MCNP Simulation Results of the LIR2032 $LiCoO_2$ Battery in the Second OSU Experiment

Reaction	Product Half-life (day)	Total Number of Reactions	Induced Activity (Bq)
$^{50}Cr(n,\gamma)^{51}Cr$	27.7	3.38×10^{11}	9.80×10^{4}
$^{58}Ni(n,p)^{58}Co$	70.9	4.07×10^{9}	4.61×10^{2}
$^{58}Ni(n,\gamma)^{59}Ni$	2.77×10^{7}	5.75×10^{11}	1.66×10^{-1}
$^{58}Fe(n,\gamma)^{59}Fe$	44.5	6.09×10^{9}	1.10×10^{3}
$^{56}Fe(n,p)^{56}Mn$	0.107	4.76×10^{8}	3.55×10^{4}
$^{54}Fe(n,p)^{54}Mn$	312	1.18×10^{9}	3.04×10^{1}
$^{186}W(n,\gamma)^{187}W$	1.00	7.70×10^{8}	6.20×10^{3}
$^{98}Mo(n,\gamma)^{99}Mo$	2.75	7.95×10^{7}	2.32×10^{2}
$^{55}Mn(n,\gamma)^{56}Mn$	0.107	2.60×10^{11}	1.94×10^{7}
$^{27}Al(n,\gamma)^{28}Al$	0.00156	5.65×10^{9}	2.91×10^{7}
$^{27}Al(n,\alpha)^{24}Na$	0.625	4.41×10^{6}	5.67×10^{1}
$^{59}Co(n,\gamma)^{60}Co$	1930	4.53×10^{12}	1.89×10^{4}
$^{59}Co(n,\alpha)^{56}Mn$	0.107	5.03×10^{6}	3.76×10^{2}
$^{59}Co(n,p)^{59}Fe$	44.5	5.49×10^{7}	9.90×10^{0}
$^{23}Na(n,\gamma)^{24}Na$	0.625	1.30×10^{9}	1.67×10^{4}
$^{63}Cu(n,\gamma)^{64}Cu$	0.529	5.91×10^{11}	8.96×10^{6}

4.3 Reactor Spectra Reconstruction

After the reactor experiments, the induced activity results obtained from the gamma spectroscopy analyses were then used to reconstruct the reactor neutron spectra to examine whether irradiated Li-ion batteries could be used for reconstruction. In this research, a pre-release (beta) version of the SNL-SAND-IV code was utilized to fulfill this task. SNL-SAND-IV is an unfolding tool that uses an iterative perturbation method to reconstruct a “best fit” neutron flux spectrum for a set of activation foils [42] [43]. The inputs to SNL-SAND-IV are the foil materials and reaction types, the measured activities

of each product (in units of Bq per target nucleus), and an initial (guess) spectrum form. Since SNL-SAND-IV was originally designed for foils, and the use of activation foils is a well-established methodology, as presented in Section 2.3, the irradiated foils during the UMass reactor experiments were first used to reconstruct the reference spectra. After that, irradiated Li-ion batteries were used for reconstruction and the result is compared to the reference spectra from the activation foils.

4.3.1 Reactor Spectra Reconstruction using Foil Results

During the two UMass reactor experiments, ten foils (as shown in Table 4-3) were irradiated each time and generated thirteen reactions that produced radionuclides with significant activities. Ten out of those thirteen reactions and their measured activities were utilized in the SNL-SAND-IV input deck because of the availability of their cross sections in the SNL-SAND-IV library (cstape). The relation between the activity and the irradiation time is shown as Figure 4-2. According to the exposure duration of the foils in the experiments as well as the half-lives of the foil materials, most foil activities were not saturated after the exposure. Therefore, the “time integrated” option was used in SNL-SAND-IV simulations; it is designed for the situation when the saturation activities are not reached at the end of the irradiation. SNL-SAND-IV terminates its iterative solution process when the measured-to-calculated activities become stable (to within less than one percent change per iteration). A best solution for both experiments was achieved

after 68 and 17 iterations for the first and second experiments, respectively, and the overall standard deviation of measured activities is less than 10% in both cases. Table 4-6 shows the output results for those two reconstructions.

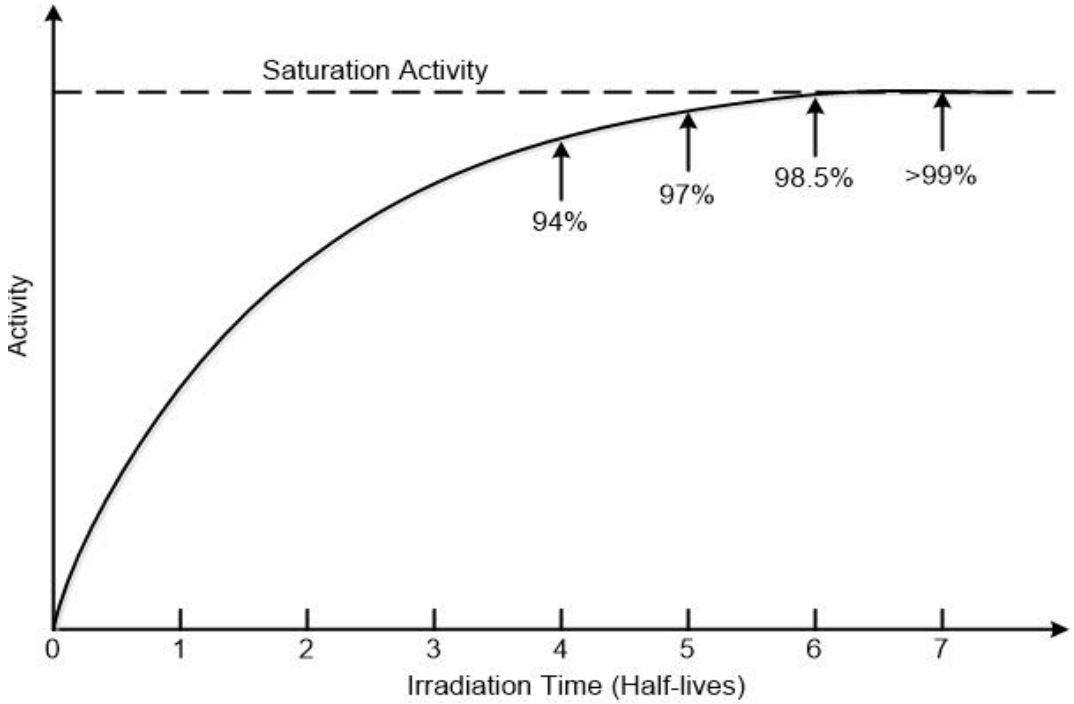

Figure 4-2. Relationship between the activity level and the irradiation time.

The reconstructed spectra from SNL-SAND-IV using activated foils for both UMass experiments are plotted in Figure 4-3. The two reconstructed spectra agree with each other and are almost identical. There is only some slight deviation at the higher energy range above 1 MeV. Therefore, these foils reconstructed results will be used as the reference reactor spectra to evaluate the performance of the reconstruction using Li-ion batteries for the same experiment.

Table 4-6 SNL-SAND-IV Output for Foils in UMass Experiments

Foil Reaction	Experiment 1		Experiment 2	
	Calculated Activity (Bq/nucleus)	Deviation from Measured	Calculated Activity (Bq/nucleus)	Deviation from Measured
^{58}Ni(n,p)	9.47×10^{-20}	–5.63%	1.71×10^{-19}	–22.8%
^{24}Mg(n,p)	1.30×10^{-19}	–7.95%	1.42×10^{-19}	–5.43%
^{27}Al(n,α)	7.53×10^{-20}	6.52%	7.54×10^{-20}	1.04%
^{46}Ti(n,p)	7.59×10^{-21}	3.05%	9.56×10^{-21}	–0.369%
^{47}Ti(n,p)	6.44×10^{-19}	3.84%	7.67×10^{-19}	16.77%
^{48}Ti(n,p)	1.34×10^{-20}	1.22%	1.22×10^{-20}	3.56%
^{54}Fe(n,p)	1.07×10^{-20}	–0.617%	2.53×10^{-20}	8.99%
^{58}Fe(n,γ)	4.49×10^{-19}	–0.185%	5.99×10^{-19}	–0.608%
^{63}Cu(n,γ)	3.13×10^{-16}	–0.134%	2.51×10^{-16}	–0.604%
^{197}Au(n,γ)	4.32×10^{-16}	–0.118%	4.04×10^{-16}	–0.559%
Overall		4.26%		10.1%

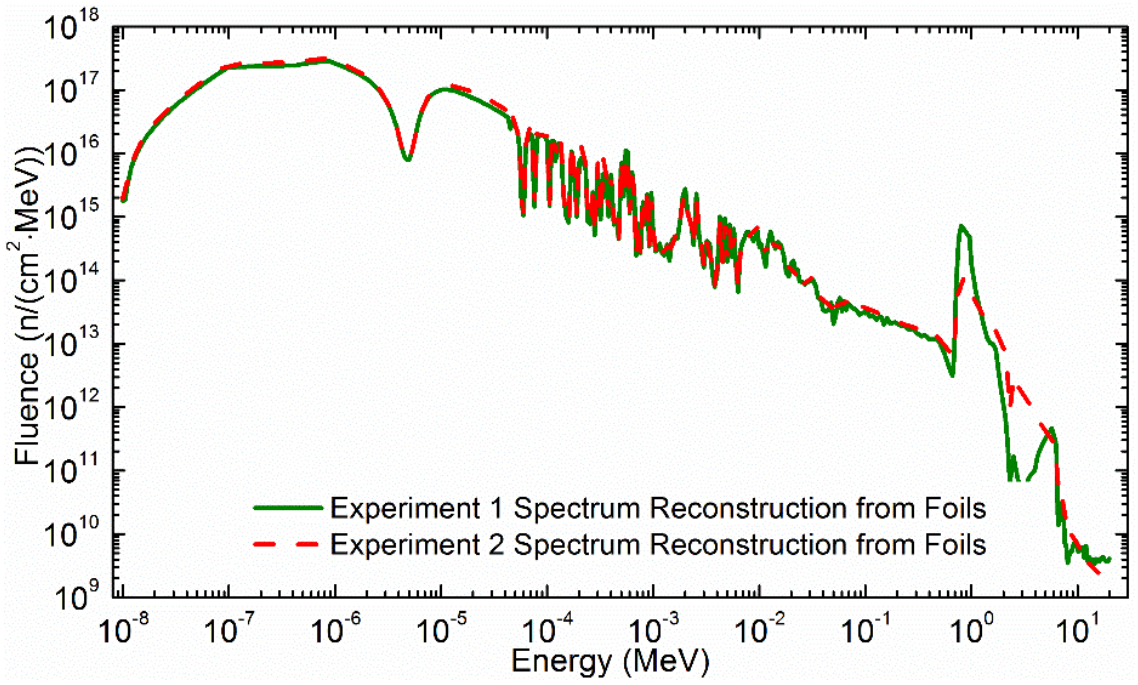

Figure 4-3. SNL-SAND-IV reconstructed source neutron spectrum comparison of the two experiments using ten activated foils at the UMass FNI facility.

4.3.2 First UMass Reactor Experiment Spectra Reconstruction using Battery Results

With the reference reactor spectra using activated foils available, irradiated Li-ion batteries in the two UMass experiments were then used for spectra reconstruction. During the first UMass experiment, the MEC201 $LiCoO_2$ and the ML-2020 $LiMnO_2$ were activated and their measured activities are first used to reconstruct the source spectrum. They are chosen because of their thinner thickness (as shown in Table 3-1) in order to minimize the uncertainty that might occur due to the self-shielding effect in thicker batteries. Five and eight reactions as well as the measured activities of each product were utilized in the SNL-SAND-IV input deck for the MEC201 and ML-2020, respectively. Table 4-7 shows the SNL-SAND-IV output results for these two batteries. The output shows that the measured and calculated activities are within 0.01% in both cases. These deviations are actually smaller than those of the foils, but there were 1.25 to 2 times more reactions to be convolved in the case of the foils. This implies that the more reactions in the input, the more difficult for the code to converge to a best fit to match all the reactions. Another reason may be that more reactions in the input will introduce more activity counting error to the reconstruction process, which will in turn result in a larger deviation. Also noteworthy is that the activities (Bq/nucleus) are similar for the foils and battery constituents.

The reason these reactions were selected is because of the quantifiable activation products after irradiation, as well as the availability of the SNL-SAND-IV cross section

library. For instance, the cross section of all five reactions for the MEC201 battery are present in the library; however, for the ML-2020 battery, two reactions, $^{75}As(n,\gamma)$ and $^{187}W(n,\gamma)$, that provided significant activities are not available in the cross section library. Therefore, those reactions were omitted in the present work.

Table 4-7 SNL-SAND-IV Output for Batteries from the First UMass Experiment

Reaction	MEC201 $LiCoO_2$		ML-2020 $LiMnO_2$	
	Calculated Activity (Bq/nucleus)	Deviation from Measured	Calculated Activity (Bq/nucleus)	Deviation from Measured
$^{23}Na(n, \gamma)$	n/a	n/a	2.69×10^{-17}	0.00%
$^{54}Fe(n, \alpha)$	n/a	n/a	5.89×10^{-23}	0.01%
$^{54}Fe(n,p)$	n/a	n/a	1.67×10^{-20}	0.00%
$^{58}Fe(n, \gamma)$	n/a	n/a	4.38×10^{-18}	0.00%
$^{58}Ni(n,p)$	1.29×10^{-19}	0.01%	n/a	n/a
$^{59}Co(n,\gamma)$	8.09×10^{-19}	0.00%	6.01×10^{-19}	0.00%
$^{59}Co(n,p)$	n/a	n/a	4.37×10^{-23}	–0.02%
$^{63}Cu(n,\alpha)$	7.17×10^{-25}	0.01%	n/a	n/a
$^{63}Cu(n,\gamma)$	2.14×10^{-16}	0.00%	n/a	n/a
$^{98}Mo(n, \gamma)$	n/a	n/a	5.11×10^{-17}	0.00%
$^{197}Au(n,\gamma)$	4.47×10^{-16}	0.00%	1.72×10^{-15}	0.00%

The SNL-SAND-IV code was originally designed to reconstruct source spectrum using activated isotopes from single reaction sources, such as those used in activation foils. However, when reconstructing using batteries, some radionuclides are produced from multiple reactions. This is a challenge for using the SNL-SAND-IV code to reconstruct spectrum from batteries since its input uses the activity per target nuclide. For example, when measuring the irradiated MEC201 battery, we can only obtain the overall ^{60}Co

activity of 51.4 Bq. However, both ^{63}Cu(n,α) and ^{59}Co(n, γ) reactions produce ^{60}Co. To overcome this problem and obtain the activity from each reaction source for a radionuclide, MCNP simulations were used to determine the fraction of reactions from each original isotope. For the example above, MCNP simulation indicates that ^{63}Cu(n,α) only contributes 0.003% of the overall ^{60}Co activity. The rest of the ^{60}Co is produced by the ^{59}Co(n, γ) reaction, which is no surprise since (n, γ) reactions are usually the most dominate reaction because of the larger cross-section compared to other reaction types and typically (n, γ) reactions do not have a reaction threshold energy. Therefore, with the help of MCNP simulation, one could attribute the overall activity of a radionuclide to each individual reaction.

In the real utilization of this method, multiple types of battery samples would be collected and studied for the same nuclear weapon incident. Because both of the MEC201 and ML-2020 batteries were irradiated during the first UMass experiment at the same time, the combined results of those two batteries were used to reconstruct the reactor source spectrum as well. Table 4-7 shows that there are two reactions, ^{59}Co(n, γ) and ^{197}Au(n, γ), that appeared in both batteries. Therefore, the activities of the same product and the mass of the same target material were added together for the combined simulation. The reactions that only occurred in one battery were kept the same. At first, all eleven reactions were used in this combined simulation. The reconstructed result showed a 12% overall difference between the measured activities and the calculated results. In order to obtain a

result with a smaller difference, ^{58}Ni(n, p) and ^{63}Cu(n, α) reactions were removed from this combined simulation and a total of 9 reactions were finally used. The SNL-SAND-IV output results are listed as Table 4-8. Even though the code took more iterations to converge, the overall deviations in the measured-to-calculated activities were decreased to less than 0.01%.

Table 4-8 SNL-SAND-IV Output for the Combined MEC201 and ML-2020 Batteries from the First UMass Experiment

Reaction	MEC201 $LiCoO_2$ and ML-2020 $LiMnO_2$ Combined	
	Calculated Activity (Bq/nucleus)	Deviation form Measured
^{23}Na(n, γ)	2.69×10^{-17}	0.00%
^{54}Fe(n, α)	5.89×10^{-23}	0.02%
^{54}Fe(n,p)	1.67×10^{-20}	0.00%
^{58}Fe(n, γ)	4.38×10^{-18}	0.00%
^{59}Co(n,γ)	7.65×10^{-19}	0.00%
^{59}Co(n,p)	4.37×10^{-23}	−0.02%
^{63}Cu(n,γ)	2.14×10^{-16}	0.00%
^{98}Mo(n, γ)	5.11×10^{-17}	0.00%
^{197}Au(n,γ)	8.09×10^{-16}	0.00%

Thereafter, the reconstructed source spectra using SNL-SAND-IV for both individual batteries, as well as the combined model, were plotted together with the reference spectrum reconstructed from foils for comparison, as shown in Figure 4-4. The plot shows that the reconstructed spectra using Li-ion batteries has similar behavior and trend as the reference spectrum reconstructed using foils. Specifically for the MEC201 battery, the reconstruction results almost overlay the reference spectrum for energy lower

than 1 MeV. Quantitatively speaking, the normalized root mean square errors compared to the reference spectrum are 7.1%, 9.3% and 8.9%, for the MEC201, ML-2020 and the combined batteries, respectively. A reason that might lead to the difference is the accuracy of the activity measurement. Generally, larger activity results in a higher counting rate, which provides a more precise activity measurement. However, the majority of the radionuclide activity levels of the experiment-exposed batteries are in the range of 10^{-5} to 10^{-2} μCi, which is relatively low, which might cause a larger relative error. This means in a real nuclear weapon detonation incident, a simple hand held radiation detector should quickly check the emission rates from the battery samples, in order to help the researchers determine which samples (those with higher activity level) to analyze first.

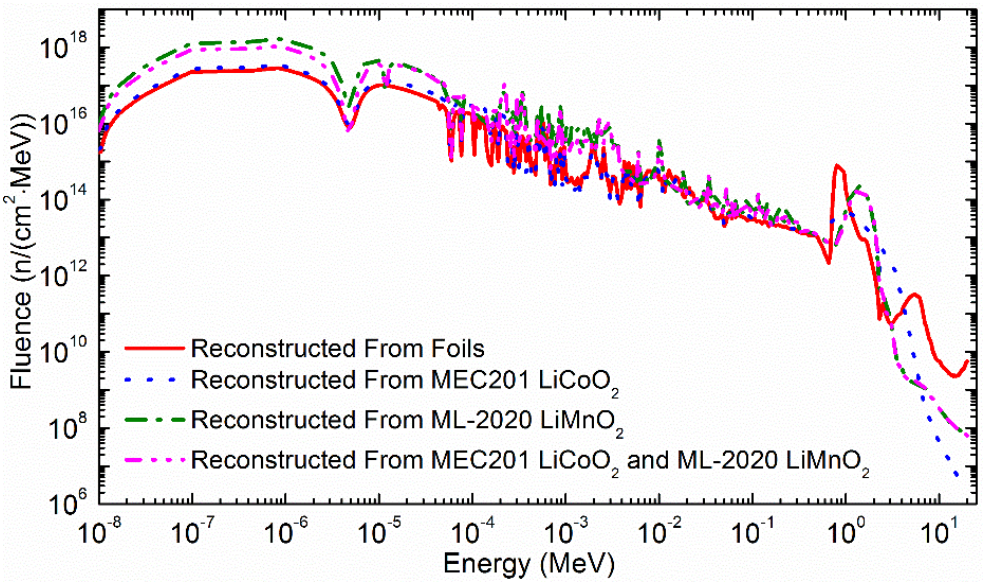

Figure 4-4. SNL-SAND-IV reconstruction of source neutron spectrum using foils and batteries in the first experiment at UMass.

Since the ML-2020 is about twelve time thicker than the MEC201 battery, the neutron self-shielding effect might lead the ML-2020 battery to having the larger difference. By looking closely at the spectrum reconstructed using the ML-2020, it better matches with the reference spectrum in the higher energy range ($> 3\times10^{-3}$ MeV), while it exhibits a positive bias within the lower energy range ($< 3\times10^{-3}$ MeV). Consideration was given as to whether this difference might be due to the ML-2020 being thicker compared to the MEC201 battery. Hence, more fast neutrons are slowed down to thermal neutron range, which leads to more neutrons in the lower energy range. Because of this possibility of self-shielding, MCNP simulations were performed to study the degree to which the battery itself perturbs the neutron flux at the measurement location. The results show that the difference is negligible. For instance, simulations with and without the MEC201 battery present at a certain location show less than 0.01% difference in neutron fluxes.

Further investigation was made to determine the cause of the bigger difference. Eventually, it was observed that if the $^{58}Fe(n,\gamma)$ and $^{23}Na(n,\gamma)$ reactions are omitted from the SNL-SAND-IV reconstruction for the ML-2020, as well as the combined battery, the reconstruction results are very close to the foils reference spectrum, as shown in Figure 4-5. The likely reason including the $^{23}Na(n,\gamma)$ reaction in the reconstruction leads to a bigger error is that the two gamma-ray peaks of ^{24}Na are located at 1368.45 keV and 2754.03 keV, and the efficiency of the Ge detector is only calibrated from 122 keV to 1332 keV. Therefore, the measured activity for ^{24}Na may be inaccurate. The peaks of ^{59}Fe were

also examined. The two peaks are located at 1099.33 keV and 1291.70 keV, which are close to the highest energy calibration point. Similarly, the ^{60}Co peaks are also located nearby at 1173.23 keV and 1332.55keV, and ^{60}Co does not introduce a large error when included in the reconstruction model. Another interesting, but noteworthy fact is that the ^{58}Fe(n,γ) and ^{23}Na(n,γ) reactions are two out of four reactions that alternative cross sections have been added in SNL-SAND-IV cross section library for evaluation purpose---it is unknown whether this means that these reactions have also given other users issues.

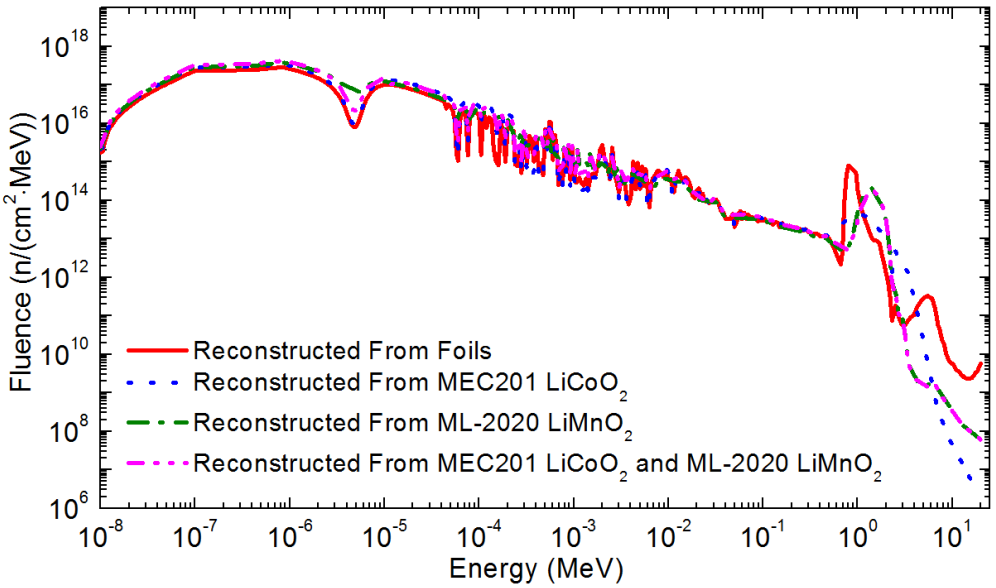

Figure 4-5. SNL-SAND-IV reconstruction of source neutron spectrum using foils and batteries in the first experiment at UMass without considering ^{58}Fe(n,γ) and ^{23}Na(n,γ) reactions in the ML-2020 and the combined batteries.

The above analyses and reconstructed results show that Li-ion batteries are capable of reconstructing the neutron source spectrum.

4.3.3 Second UMass Reactor Experiment Spectra Reconstruction using Battery Results

As listed is Table 4-2, the CR2032 $LiMnO_2$ and LIR2032 $LiCoO_2$ batteries were exposed in the second UMass experiment. Therefore, these two batteries were then used to reconstruct the UMass spectrum, just like using MEC201 and ML-2020 batteries in the first UMass experiment in Section 4.3.2. There are 3 reactions and 6 reactions that were used in SNL-SAND-IV reconstruction for the CR2032 and LIR2032, respectively. The reactions and the SNL-SAND-IV results are listed in Table 4-9.

Table 4-9 SNL-SAND-IV Output for Batteries from the Second UMass Experiment

Reaction	CR2032 $LiMnO_2$		LIR2032 $LiCoO_2$	
	Calculated Activity (Bq/nucleus)	Deviation from Measured	Calculated Activity (Bq/nucleus)	Deviation from Measured
$^{23}Na(n, \gamma)$	3.19×10^{-18}	0.00%	4.91×10^{-18}	0.00%
$^{58}Fe(n, \gamma)$	8.21×10^{-18}	0.00%	1.25×10^{-17}	0.00%
$^{58}Ni(n,p)$	3.68×10^{-19}	0.00%	2.48×10^{-19}	0.00%
$^{59}Co(n,\gamma)$	n/a	n/a	4.52×10^{-19}	0.00%
$^{63}Cu(n,\gamma)$	n/a	n/a	1.67×10^{-16}	0.00%
$^{98}Mo(n, \gamma)$	n/a	n/a	4.26×10^{-17}	0.00%

The reconstructed spectra are plotted in Figure 4-6, together with the reconstructed second UMass experiment reference spectrum using ten foils. Overall, both reconstructed spectra match with the foil reconstructed result. The CR2032 battery results exhibit a little higher deviation at higher energy, which may be caused by the lack of reconstruction reactions (only three) in the SNL-SAND-IV input. Quantitatively speaking, the normalized

RMS error for the CR2032 and LIR2032 compared to the ten foils reconstructed reference spectrum is 9.6% and 13%, respectively. The fact that both ^{58}Fe(n,γ) and ^{23}Na(n,γ) reactions are used in both reconstructions is another reason for this difference, as discussed in Section 4.3.2.

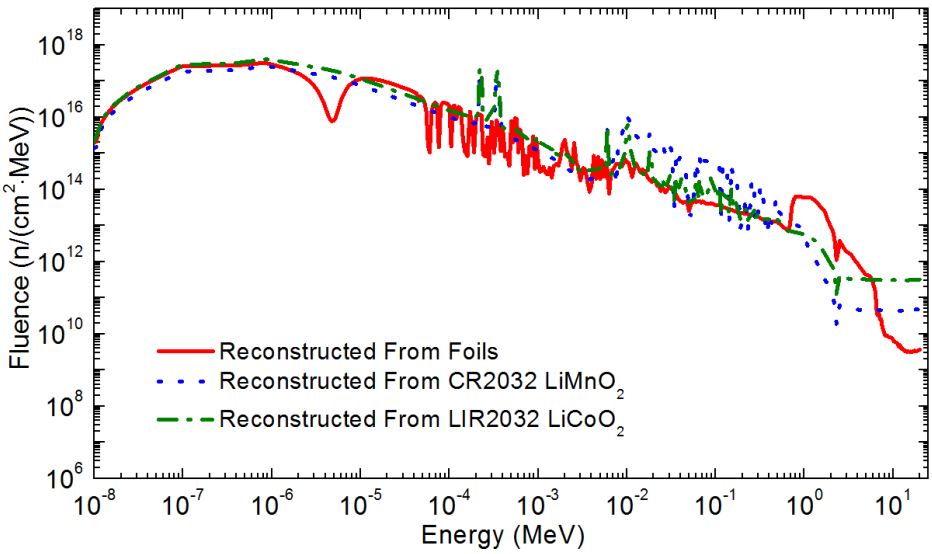

Figure 4-6. SNL-SAND-IV reconstruction of source neutron spectrum using foils and batteries in the second experiment at UMass.

Another noteworthy point is that neither the reconstructed spectrum from CR2032 nor from LIR2032 has the characteristic of a trough between energy level from 10^{-6} to 10^{-5} MeV, as the foil reconstructed spectrum does. This trough behavior is also found in the reconstructed results for the first UMass experiment using both foils and batteries, as shown in Figure 4-4. Efforts were made to understand what causes this behavior. By comparing the reactions that have been used in all reconstruction cases (Table 4-6 to Table 4-9), we found out that the ^{197}Au(n,γ) reaction was utilized in all other reconstruction cases,

expect for the CR2032 and LIR2032 cases. By examining the cross section of ^{197}Au(n,γ), as shown in Figure 4-7, we found out that there is a resonant peak between energy level from 10^{-6} to 10^{-5} MeV. This is likely the cause of the trough characteristic in the reconstructed results, (1) since the energy range matches, and (2) because of this peak in the ^{197}Au(n,γ) cross section, the reconstruction process forms a trough in the flux spectrum in order to offset the resonant peak. This confirms that the reactions used in SNL-SAND-IV input and their cross sections will have an impact of the reconstructed spectrum.

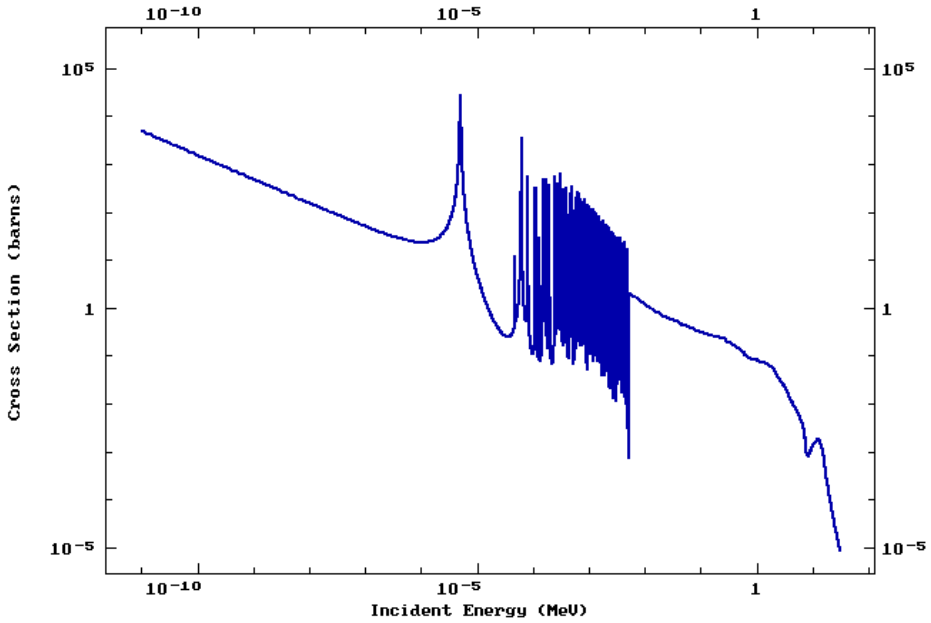

Figure 4-7. ^{197}Au(n,γ) cross section [44].

During the second OSU experiment and the second UMass experiment, an iPod shuffle music player and an additional iPod shuffle rechargeable Li-polymer battery were

also irradiated each time. In order to minimize the induced activity of the casing, an Al casing edition of the iPod was chosen, instead of stainless steel casing. Table 4-10 and Table 4-11 shows the induced activities for the iPod (with battery) and the iPod battery alone measured 1 day after the exposure to the second OSU and the second UMass experiments, respectively. It shows that the iPod has a higher activity level compared with the iPod battery alone, which is expected since the iPod has more elements in the case and other electronic components. This also explains why there are three radionuclides that are only detected in the iPod. Future work should study on the feasibility of using Li-polymer battery type, as well as the battery inside the consumer electronics.

4.3.4 Summary

Overall, by comparing the reconstructed spectra using the activation foils and the irradiated Li-ion batteries in both UMass reactor experiments, we have shown that the Li-ion batteries are capable of reconstructing the source spectrum using the SNL-SAND-IV code.

Valuable lessons were learned from these experiments too, especially from our first two experiments conducted at OSU. For example, to reduce costs, no team member was send to OSU to observe the experiments processes. Therefore, when performing the post irradiation analyses, there are some missing pieces of details about the experiments. With that lesson learned, during the latter two experiments, our colleagues actually went to

UMass and participated in the whole process. Therefore, we were able to obtain more detailed information about those experiments. Another lesson learned is that we should have irradiated foils during the OSU experiments too, just as the UMass experiments, so that more accurate information about the reactor operation condition, such as source neutron spectrum and flux level, could be calculated using the activation foils methodology and compared with the reconstructed results.

Table 4-10 Induced Activities for iPod and iPod Battery Exposed in the Second OSU Experiment

Radionuclides	iPod	iPod Battery
	Activity (Bq)	Activity (Bq)
As-76	8.97×10^{3}	6.97×10^{2}
Au-198	3.58×10^{5}	9.05×10^{3}
Co-58	2.71×10^{3}	4.18×10^{2}
Co-60	5.48×10^{4}	5.93×10^{4}
Cr-51	1.49×10^{5}	N/A
Cu-64	2.83×10^{7}	9.90×10^{6}
Fe-59	2.45×10^{3}	N/A
Ga-72	2.30×10^{4}	1.12×10^{3}
La-140	1.51×10^{1}	N/A
Mn-56	9.23×10^{7}	8.16×10^{5}
Mo-99	8.91×10^{3}	N/A
Na-24	9.85×10^{4}	5.56×10^{3}
Sb-122	1.66×10^{3}	N/A
Sn-117m	3.59×10^{2}	N/A
Ta-182	2.33×10^{4}	N/A
Tc-99m	5.56×10^{4}	N/A
W-187	1.18×10^{5}	N/A
Zn-65	1.87×10^{3}	N/A
Zn-69m	2.56×10^{4}	N/A

Table 4-11 Induced Activities for iPod and iPod Battery Exposed in the Second UMass Experiment

Radionuclides	iPod	iPod Battery
	Activity (Bq)	Activity (Bq)
As-76	3.30×10^{2}	5.51×10^{1}
Au-198	6.33×10^{3}	5.59×10^{2}
Co-58	9.88×10^{1}	4.44×10^{1}
Co-60	3.66×10^{2}	8.51×10^{2}
Cu-64	1.37×10^{5}	1.54×10^{5}
Ga-72	9.07×10^{2}	1.04×10^{2}
Mn-56	3.85×10^{5}	1.52×10^{4}
Na-24	1.92×10^{3}	2.80×10^{2}
Ta-182	6.03×10^{2}	N/A
W-187	2.86×10^{3}	N/A
Zn-69m	5.07×10^{2}	N/A

CHAPTER 5

NUCLEAR WEAPON CHARACTERISTICS DETERMINATION

In this chapter, background information about the nuclear weapons that are used in this research is first introduced. After that, MCNP models are used to simulate the nuclear weapon spectra transport. Then, the equations to calculate the weapon yield will be obtained, followed by two methods to determine the nuclear device type. Lastly, the weapon spectra will be reconstructed using the SNL-SAND-IV code.

5.1 Nuclear Weapon Background

There are mainly two basic types of nuclear weapons: fission and fusion. The fission nuclear weapons produce their explosive energy from nuclear fission reactions, whereas the fusion nuclear devices derive the energy from fusion reactions and are generally referred to as thermonuclear weapons [45]. In the fission nuclear weapons, fissile material, such as enriched uranium or plutonium, is assembled into a supercritical mass, which is the quantity needed to start an exponentially growing nuclear chain fission reaction. Based on how the reaction is triggered, there are two basic types of designs: gun type and implosion type. The gun-type device is initiated by shooting a piece of subcritical material (enriched uranium) into another to form the critical mass by conventional chemical explosion, whereas the implosion type weapon is started by compressing the subcritical material (plutonium) sphere core to many times its original density to reach the

criticality via chemical explosives using explosive lenses [46]. Diagrams of the gun-type and implosion-type nuclear weapon designs are shown as Figure 5-1.

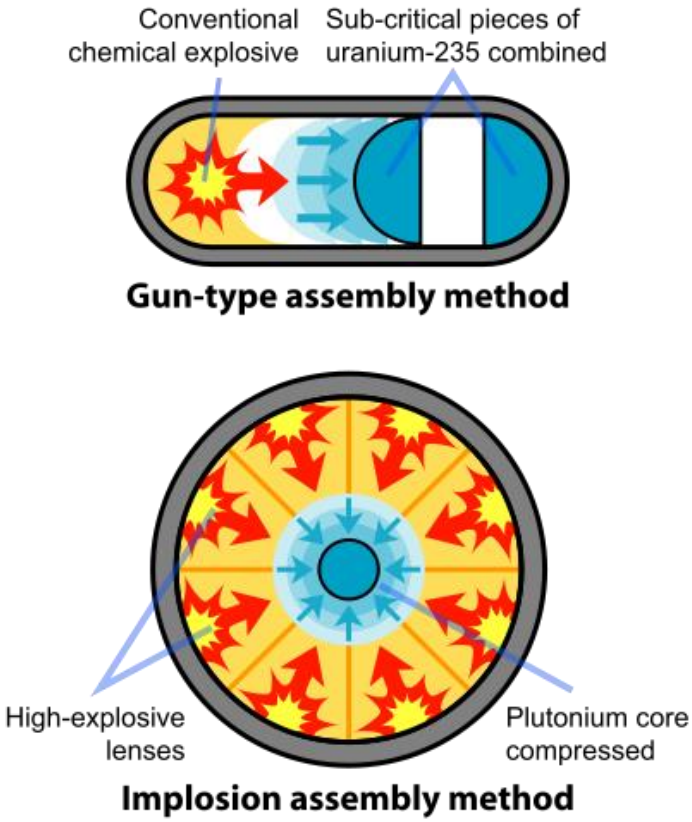

Figure 5-1. Diagrams of gun-type and implosion-type fission nuclear weapon designs. [47]

We perceive that in the case of a nuclear weapon incident, a fission weapon is presently more likely to be detonated compared with a thermonuclear device, because to manufacture a thermonuclear requires much greater technical demands. Using South Africa as an example: according to the report to the South African President F. W. de Klerk in November 1989, J. W. de Villiers and Waldo Stumpf stated that the South African Arms

Corporation (Armscor) had six gun-type nuclear devices stored, and Armscor was studying the feasibility of implosion-type nuclear weapons [48]. About three years later on March 24, 1993, President de Klerk announced in parliament that South Africa had built six gun-type nuclear weapons and then dismantled them. He also emphasized that South Africa had neither developed thermonuclear bombs nor carried out a test in the South Atlantic [48]. Therefore, our research mainly focuses on Li-ion batteries exposed to fission weapon neutrons.

5.2 Nuclear Weapon Spectra Modeling

In our research, two different types of 10 kt (kiloton) nuclear weapons were studied, in particular, the World War II era Little Boy and Fat Man type devices. Little Boy was a ^{235}U gun-type nuclear weapon, that was dropped at Hiroshima Japan on August 6, 1945, whereas Fat Man was a ^{239}Pu implosion device detonated at Nagasaki three days later. These are the only two nuclear weapons that have been used in a war [49]. Their source spectra were taken from literature [50] and transported by MCNP. In particular, as depicted in Figure 5-2, each weapon source was placed in the center of the MCNP model as a point source in open space in dry air. Then, spherical surfaces were made with radii from 200 m to 2.5 km from the source. Thereafter, the neutron spectra at those distances from the weapon detonation point were obtained using F2 surface tallies. The results are then plotted for comparison. For instance, Figure 5-3 shows the neutron spectrum from a 10 kt

Little Boy type device at different distances from the detonation point. The plot shows that from 800 to 1500 m, the total fluence decreases, however, the shape of the spectra are visually indistinguishable. Similarly, as shown in Figure 5-4, the spectra of a Fat Man type weapon behave in the same way from 800 to 1500 m, except at a lower fluence level compared to Little Boy.

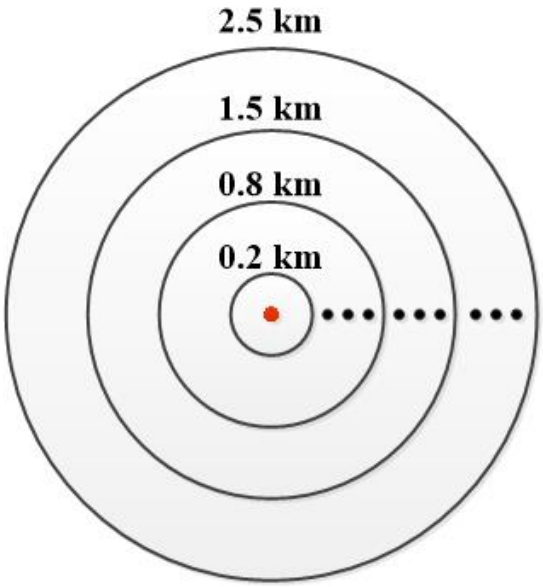

Figure 5-2. MCNP simulation geometry to obtain the nuclear weapon neutron spectra from 0.2 to 2.5 km away from the source.

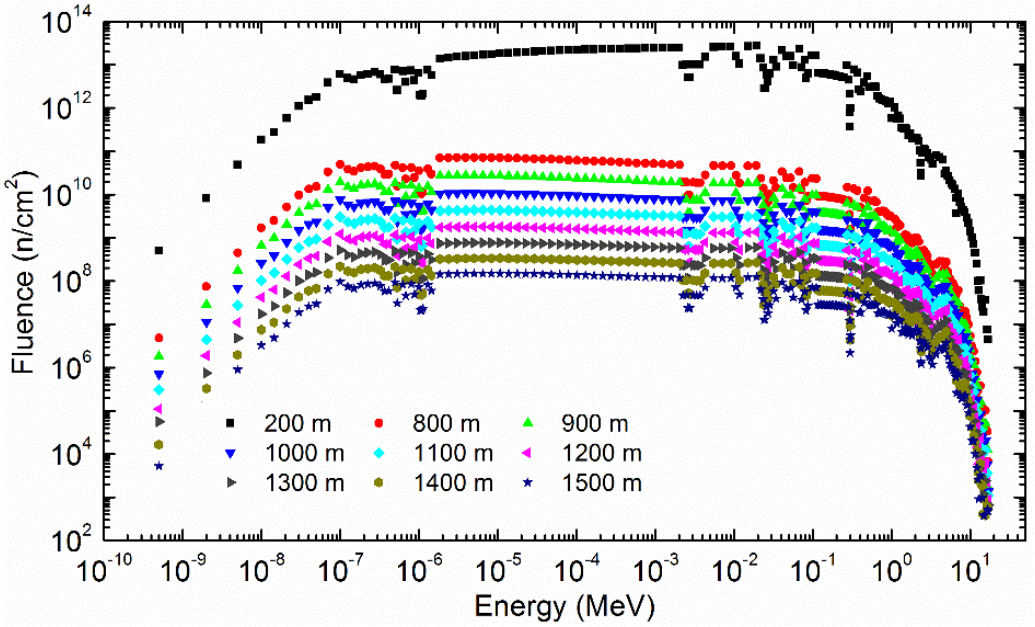

Figure 5-3. MCNP simulated neutron spectra from a 10 kt Little Boy type device at distances of 200 m and 800 to 1500 m from the detonation point.

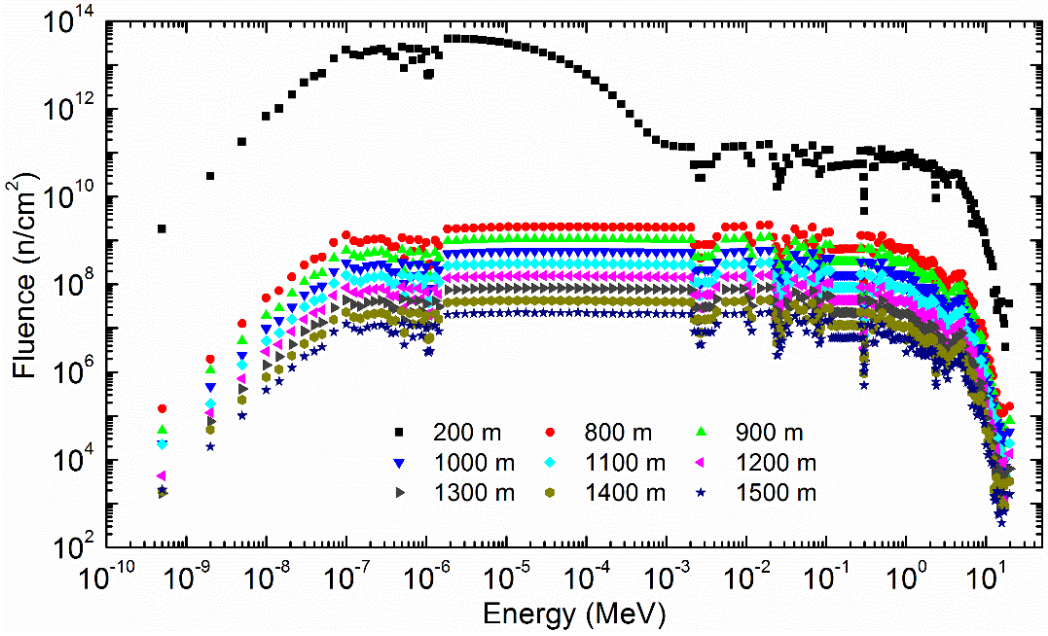

Figure 5-4. MCNP simulated neutron spectra from a 10 kt Fat Man type device at distances of 200 m and 800 to 1500 m from the detonation point.

As discussed in Section 2.5.1, this research mainly focuses on distances of 800 to 1500 m, because for a 10 kt nuclear weapon explosion, this range is considered as the moderate damage (MD) zone. Figure 5-5 shows the comparison of the neutron spectra from 10 kt Little Boy style and Fat Man type devices at 1000 m away from the detonation point as an example. From the plot we can see that at energy levels lower than 1 MeV, the two spectra have similar trends, except the Fat Man type device has a lower fluence level. This is because the neutron spectrum from Little Boy is harder (i.e., of higher energy) than that of Fat Man at the point of detonation. As stated by Whalen, Fat Man employed "tons of high explosives" that moderated the output neutron spectrum significantly [51]. Hence, for the same 10 kt size, the Fat Man type device has a lower fluence level at such distances compared to the Little Boy device.

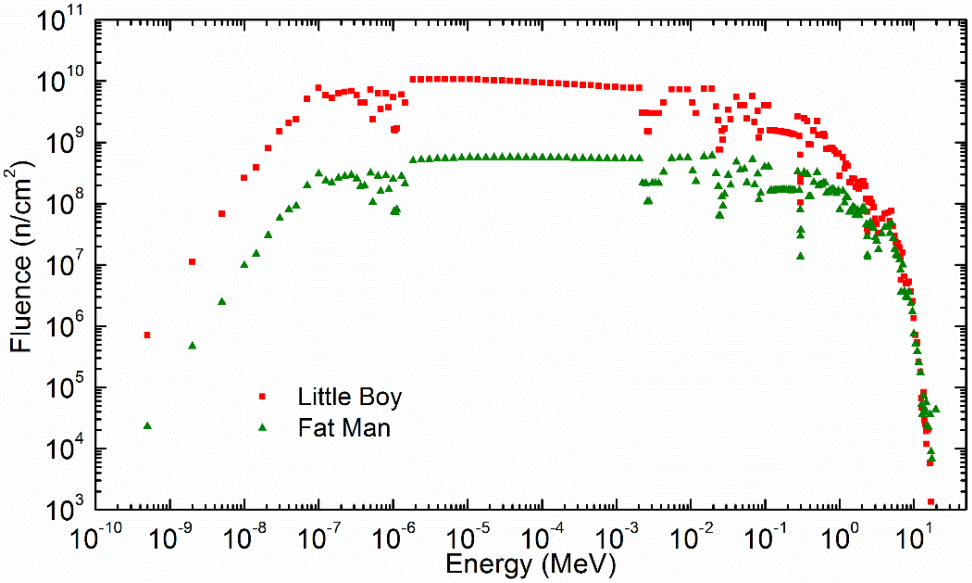

Figure 5-5. MCNP simulated neutron spectra comparison from 10 kt Little Boy and Fat Man type devices at 1000 m from the detonation point.

5.3 Nuclear Weapon Yield Calculation

In Section 2.5.2, we introduced an equation provided by Brode about half century ago to estimate the relation among the neutron fluence, yield, and distance from a nuclear weapon explosion. The equation did not specify the type of nuclear device and only provided one significant digit. As seen in Section 5.2, the neutron spectral characteristics are unique for different types of nuclear weapon devices. By comparing the calculated total fluence results at different distances from the detonation point using Brode's equation and the MCNP simulated results for Little Boy and Fat Man type devices, we found that difference exists, as shown in Figure 5-6. Therefore, it is necessary to develop a specific equation for each nuclear weapon type, in particular, a ^{235}U gun-type nuclear weapon (Little Boy type) and a ^{239}Pu implosion device (Fat Man type). By using the MCNP simulation results, two formulae, shown as Eqs. (7) and (8), were developed for the Little Boy (LB) and Fat Man (FM) type devices respectively, to provide a more accurate relation for each weapon type.

$$\text{LB}: \quad \Phi = \frac{\left(5.42\times10^{23}\ \text{n/kt}\right)Y}{r^2}\exp\left(\frac{-\rho r}{1.79\times10^{4}\ \text{g·cm/L}}\right) \tag{7}$$

$$\text{FM}: \quad \Phi = \frac{\left(4.60\times10^{21}\ \text{n/kt}\right)Y}{r^2}\exp\left(\frac{-\rho r}{2.57\times10^{4}\ \text{g·cm/L}}\right) \tag{8}$$

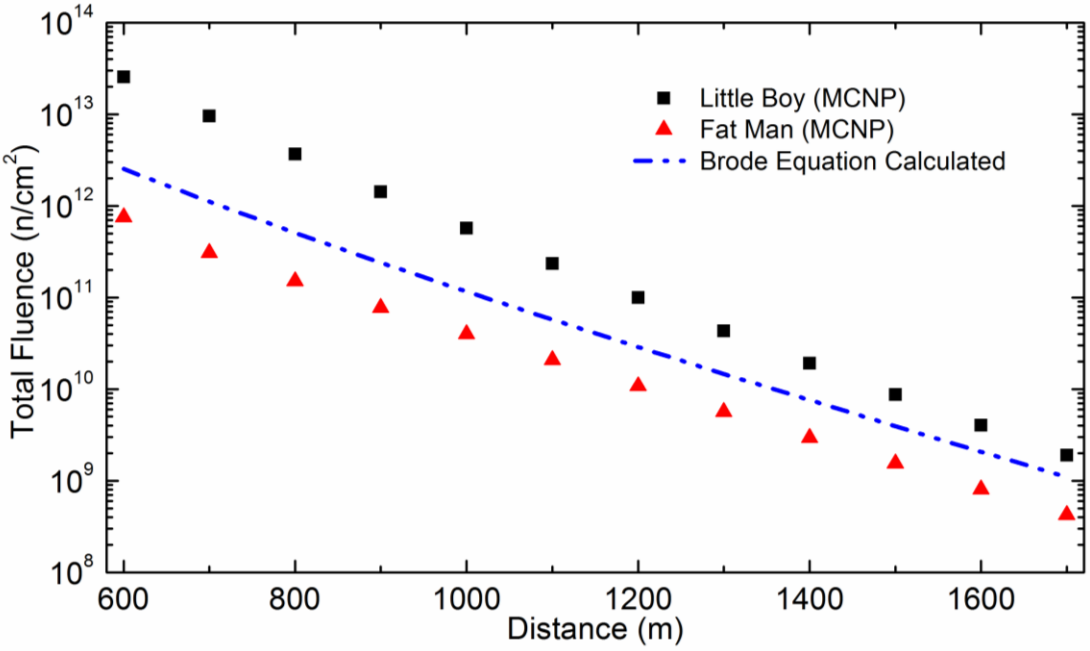

Figure 5-6. Comparison of Brode equation calculated and MCNP computed total fluence for 10 kt Little Boy and Fat Man type devices.

In the MD zone (800 to 1500 m range), the calculated results using Eqs. (7) and (8) agree with the MCNP simulated results, with less than 5% differences. The results are plotted and compared in Figure 5-7. From the plot we can see that the fitted equation calculated fluence matches well with the MCNP simulation results. It also shows that outside the MD zone, the MCNP simulated fluence starts to diverge from the fitted equations. This indicates that for the different distance ranges, unique equations might be needed to provide more accurate results. Also, it is worth mentioning that the FM equation has a similar slope as the Brode's equation as can be seen from the plot. Actually, in our early effort, we used the source spectra for Little Boy and Fat Man from earlier references [51] [52], which lead to the same exponential slope of 2.38×10^{4} g·cm/L for the Fat Man

type equation and Brode's relation [53]. This implies that his equation may have originated from an implosion type nuclear weapon device, like Fat Man.

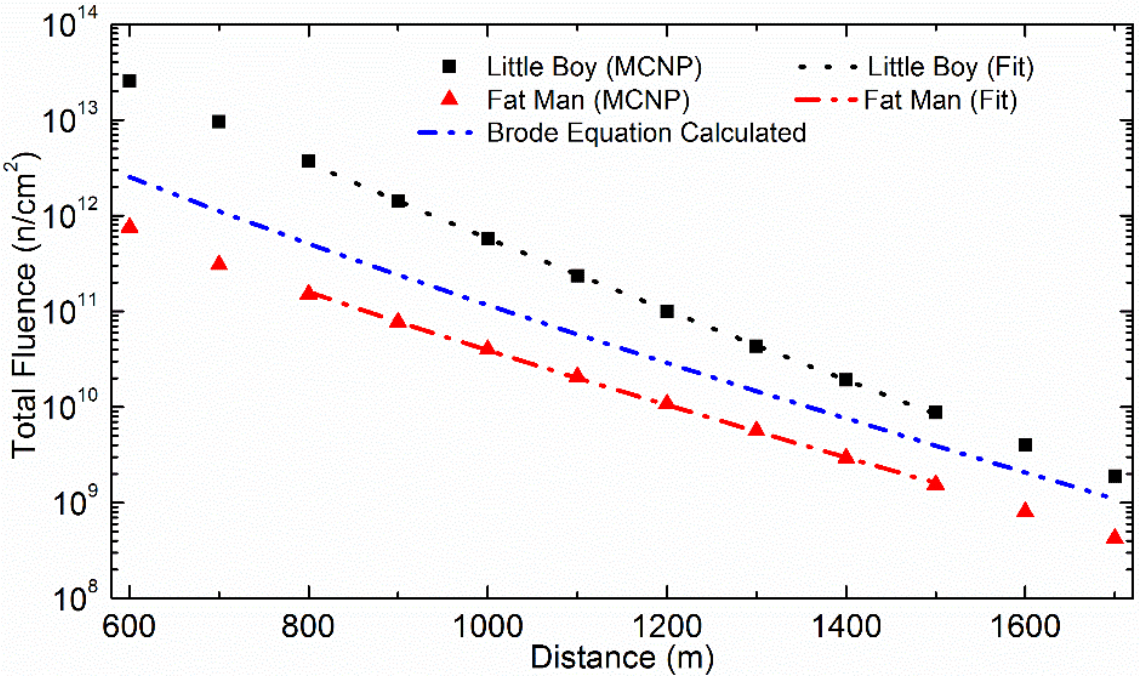

Figure 5-7. Comparison of Brode equation calculated and MCNP computed total fluence for 10 kt Little Boy and Fat Man type devices along with fits to the MCNP results.

In a similar fashion, we have developed empirical relations between the number of reactions and yield by using MCNP simulations. For instance, for the CR2032 $LiMnO_2$ battery presented in Chapters 3 and 4, ^{56}Mn is the dominant radionuclide, and the number of $^{55}Mn(n,\gamma)$ reactions were first obtained with the help of MCNP simulations for the range of 800 to 1500 m from the detonation point. Then, the number of reactions were fitted to an

equation as a function of weapon yield and distance. For example, the number of ^{55}Mn(n,γ) reactions (rxn) as a function of distance for the two fission devices are

$$\text{LB}: \quad R = \frac{\left(5.97\times10^{21}\ \text{rxn}\cdot\text{cm}^2/\text{kt}\right)Y}{r^2}\exp\left(\frac{-\rho r}{1.73\times10^4\ \text{g}\cdot\text{cm/L}}\right) \tag{9}$$

$$\text{FM}: \quad R = \frac{\left(2.63\times10^{19}\ \text{rxn}\cdot\text{cm}^2/\text{kt}\right)Y}{r^2}\exp\left(\frac{-\rho r}{2.59\times10^4\ \text{g}\cdot\text{cm/L}}\right) \tag{10}$$

In the equations above, the air density ρ and the distance of the battery sample from the detonation point r will be known in a case of a weapon detonation. Thus, there are only two unknowns in the equation, the number of reactions R and the weapon yield Y. The number of reactions can be determined using $R = A(0)/\lambda$, where $A(0)$ is the initial activity and λ is the decay constant. Therefore, R in the above equations can be calculated using the measured activities that are time corrected to the detonation instant. Hence, with the R already computed, the weapon yield Y can be solved by using the corresponding equation above.

5.4 Nuclear Weapon Spectra in Humid Air

The impact of humidity in air on the weapon spectrum is also studied. It is noteworthy that air density actually decreases with an increase in the humidity. In other words, the moist air is less dense than dry air at the same temperature. This is because water vapor contains one oxygen atom and two hydrogen atoms, and has an atomic mass of 18 atomic units. Whereas air is mainly composed of nitrogen and oxygen, which have an

atomic mass of 28 and 32, respectively. Therefore, at the same temperature, the humid air has more water vapor, which replaces the heavier air. Thus, the humid air is less dense than the dry air.

Similar to what has been done in Section 5.2 for dry air, MCNP simulations were performed to obtain the weapon neutron spectra at different distances with 20%, 40%, 60%, 80%, and 100% humidity in air. The air density, weight percentage (wt%) of water in air [54], and the MCNP input material fraction are listed in Table 5-1. The density of humid air (ρ) in g/cm^3 is calculated using an empirical relation [55]:

$$\rho = 1.2929 \times 10^{-3} \times \frac{273.15}{T} \times \frac{B - 0.3783\ \rho_V}{1.013 \times 10^5} \tag{11}$$

where T is temperature in Kelvin, B is barometric pressure in Pa, ρ_V is partial vapor pressure in Pa. The total fluence from 800 m to 1500 m for each humidity level are plotted as Figure 5-8, along with the Brode equation calculated fluence. The plot shows that with the increase in humidity from 0% to 100%, the total fluence decreases for both Little Boy and Fat Man. This is because the water vapor in the humid air moderates the neutrons more due to the presence of hydrogen. With the increase of the humidity, more water vapor is in the air. Thus, more neutrons are being moderated.

Table 5-1 Density, Water Vapor Weight Percentage in Air, and MCNP Input Material Fraction for Different Humidity Levels

Humidity		0%	20%	40%	60%	80%	100%
Density (g/cm^3)		0.001225	0.001224	0.001222	0.001221	0.001219	0.001218
wt% (Water/Air)		0	0.002140	0.004280	0.006420	0.008560	0.01070
MCNP Input Material Fraction	N	0.7556	0.7540	0.7524	0.7508	0.7492	0.7476
	O	0.2315	0.2329	0.2343	0.2357	0.2371	0.2385
	Ar	0.01289	0.01286	0.01283	0.01281	0.01278	0.01275
	H	0	0.0002	0.0005	0.0007	0.0010	0.0012

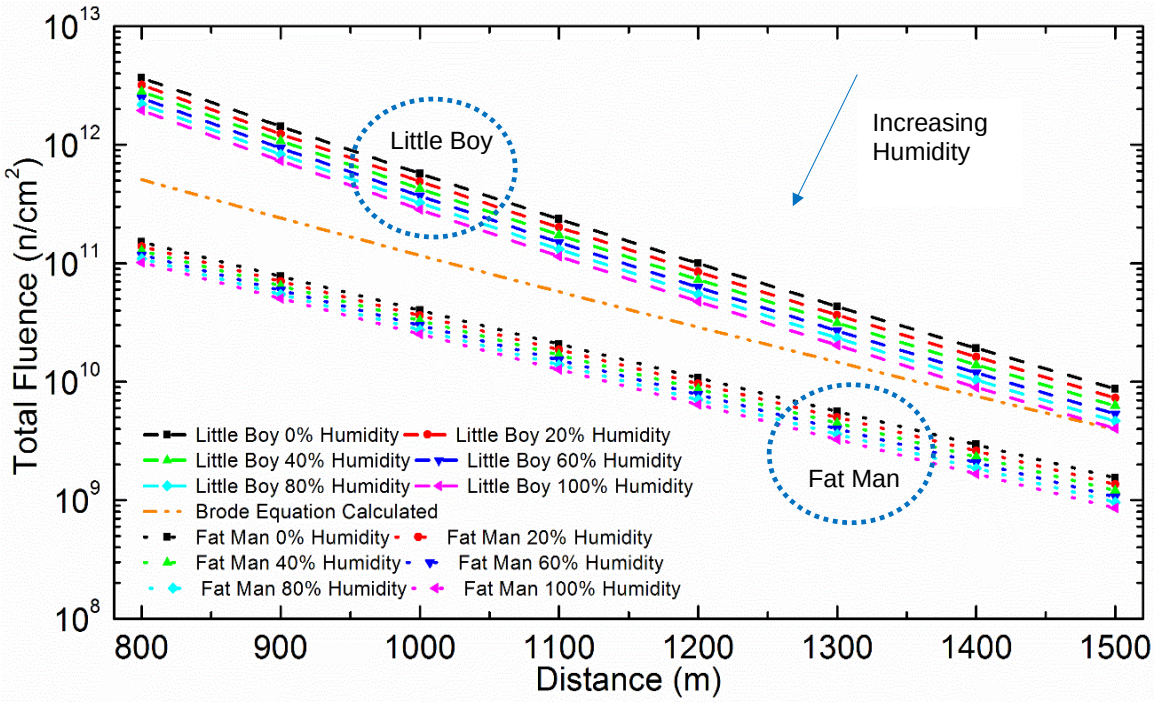

Figure 5-8. Comparison of Brode equation calculated and MCNP computed total fluence for 10 kt Little Boy and Fat Man type devices in dry air, 20%, 40%, 60%, 80%, and 100% humidity in air.

A special $S(\alpha,\beta)$ treatment of thermal neutron scattering is available in MCNP when hydrogen is in the molecular compound of water [31]. With the introduction of water vapor to model humid air, the $S(\alpha,\beta)$ cross section option for hydrogen was used in an

MCNP simulation for the 100% humidity cases of Little Boy and Fat Man to study the impact. The total fluence results from 800 to 1500 m are shown in Table 5-2. The results show that the impact from not employing the special hydrogen scattering is small. In particular, the average error for not using $S(\alpha,\beta)$ cross section is –0.31% for the Little Boy type weapon, and –0.24% for the Fat Man type device.

Table 5-2 Total Fluence with and without $S(\alpha,\beta)$ Cross Section for Hydrogen in 100% Humidity for Little Boy and Fat Man Type Weapons at Different Distances

Fluence (n/cm^2)		800 m	900 m	1000 m	1100 m	1200 m	1300 m	1400 m	1500 m
Little Boy	Without $S(\alpha,\beta)$	1.947×10^{12}	7.302×10^{11}	2.840×10^{11}	1.144×10^{11}	4.757×10^{10}	2.036×10^{10}	8.956×10^{9}	4.024×10^{9}
	Using $S(\alpha,\beta)$	1.954×10^{12}	7.328×10^{11}	2.850×10^{11}	1.147×10^{11}	4.771×10^{10}	2.042×10^{10}	8.979×10^{9}	4.034×10^{9}
Fat Man	Without $S(\alpha,\beta)$	1.015×10^{11}	5.039×10^{10}	2.526×10^{10}	1.271×10^{10}	6.427×10^{9}	3.259×10^{9}	1.669×10^{9}	8.581×10^{8}
	Using $S(\alpha,\beta)$	1.017×10^{11}	5.050×10^{10}	2.532×10^{10}	1.274×10^{10}	6.442×10^{9}	3.270×10^{9}	1.673×10^{9}	8.597×10^{8}

5.5 Nuclear Weapon Type Determination

In Section 5.3, equations are developed to calculate the weapon yield for Little Boy and Fat Man type devices. However, in order to use the correct equation for the calculation, the nuclear weapon type must be determined first. This section presents two different methods to fulfill this goal.

5.5.1 Ratio Method

One approach to distinguish the fission weapon type is using the induced activity ratio of different radionuclides from the measurements in the post detonation analysis. For example, for the $LiMnO_2$ batteries, ratios of $^{59}Fe/^{51}Cr$, and $^{51}Cr/^{60}Co$ can be utilized [56]. The neutron fluence resulting from a nuclear weapon detonation is a function of energy (E), distance (r), and yield (Y), i.e., $\Phi = \Phi(E,r,Y)$. Eqs. (7) and (8) from Section 5.3 indicate that the fluence is directly proportional to the weapon yield. However, when weapon yield changes, it only alters the total number of neutrons. The relative fluence at a particular distance remains the same. That is to say, at a specific location, when yield changes, it only changes the magnitude of the neutron spectrum. The shape of the spectrum $\varphi(E)$ remains the same, so that $\Phi = \Phi(E)$. When using this ratio method to determine the fission device type, the activities of the radionuclides are measured from the same battery. Therefore, the induced activity A of each radionuclide can be calculated using,

$$A = \int \Sigma(E)\Phi(E)\,dE = B\int \Sigma(E)\varphi(E)\,dE \tag{11}$$

where B is the fluence amplitude that can be factored out from the energy spectral shape function $\varphi(E)$. Consequently, the amplitude B can be canceled when calculating the activity ratio of two radionuclides, as shown in

$$\frac{A_1}{A_2} = \frac{\int \Sigma_1(E)\,\varphi(E)\,dE}{\int \Sigma_2(E)\,\varphi(E)\,dE} \tag{12}$$

In the equation above, the cross sections $\Sigma(E)$ are constant for each reaction. At the same time, the fluence energy function $\varphi(E)$ at the point of interest does not change. Therefore, no matter what the device yield is, the activity ratio A_1/A_2 remains the same. For example, Table 5-3 shows the activity ratios of selected radionuclides of CR2032 $LiMnO_2$ battery, 1 km from detonation point for Little Boy and Fat Man type devices.

Table 5-3 Activity Ratios of Selected Radionuclides at 1 km from Detonation Point from CR2032 $LiMnO_2$ Battery

Ratio	Little Boy Ratio	Fat Man Ratio	Percentage Difference
$^{59}Fe/^{56}Mn$	0.00101	0.00108	7.1%
$^{59}Fe/^{24}Na$	0.159	0.170	7.0%
$^{59}Fe/^{51}Cr$	0.0460	0.0532	14.6%
$^{59}Fe/^{60}Co$	220	235	6.5%
$^{56}Mn/^{24}Na$	157	157	0.1%
$^{56}Mn/^{51}Cr$	45	49	7.5%
$^{56}Mn/^{60}Co$	217,500	216,400	0.5%
$^{24}Na/^{51}Cr$	0.290	0.313	7.6%
$^{24}Na/^{60}Co$	1390	1380	0.4%
$^{51}Cr/^{60}Co$	4780	4410	8.1%

To evaluate which ratios are valuable for distinguishing the fission weapon type, the difference between the activity ratios for the same two radionuclides for the Little Boy and Fat Man type device was first examined. The ratios with the largest separation were considered most useful because they may be the least likely to be washed out by statistical error in counting. For example, the initial activity ratios of $^{59}Fe/^{51}Cr$ at 1 km from the Little Boy and Fat Man type device detonation point are 0.0460 and 0.0532 (14.6% difference),

respectively. This makes $^{59}Fe/^{51}Cr$ appear to be the most useful ratio for this battery in determining the type of fission weapon. For the same reason, the next most useful ratio is $^{51}Cr/^{60}Co$ with an 8.1% difference.

Next, the behavior of the ratios over time was also studied. The $^{59}Fe/^{51}Cr$ activity ratios for Little Boy and Fat Man type devices were plotted for the first five days after detonation, as shown in Figure 5-9. Because of the sufficiently long half-lives of ^{59}Fe and ^{51}Cr, the activity ratio remains roughly constant as expected. It is noteworthy that most of the ^{51}Cr and ^{59}Fe are originated in the steel casing of the battery, and the majority of the batteries made for personal uses nowadays have a steel casing, although the alloy may be different between batteries. Therefore, even though the results shown here are for a CR2032 $LiMnO_2$ battery, these results are extensible to other battery types.

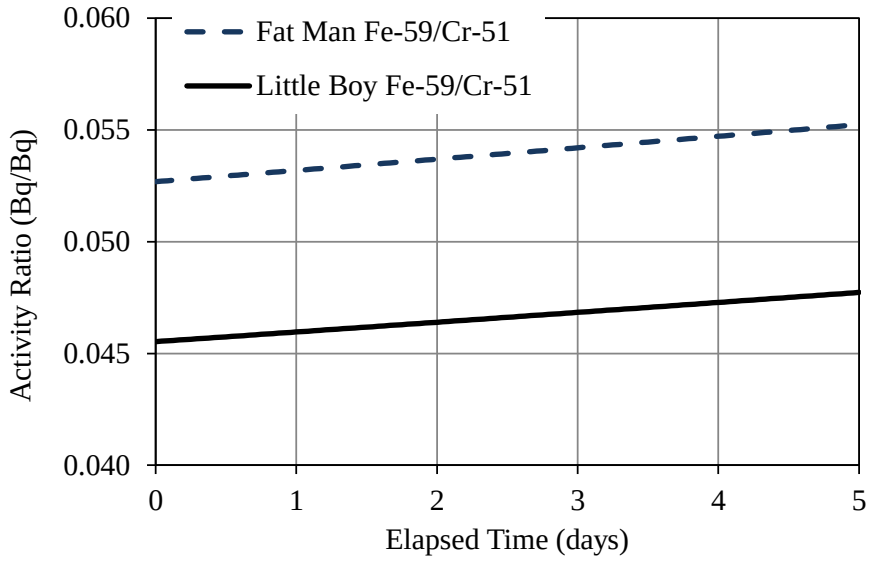

Figure 5-9. $^{59}Fe/^{51}Cr$ activity ratio for 10 kt Little Boy and Fat Man type devices as a function of time 1 km from the detonation point.

In similar fashion, the manner in which the activity ratio changes with distance was also studied. For example, Figure 5-10 shows the $^{24}Na/^{51}Cr$ ratios as a function of distance. As can be seen, the ratios exhibit a nearly constant trend. This means that the $^{24}Na/^{51}Cr$ ratio does not change significantly with the distance and can be used over a wide range of distances to distinguish the weapon type. However, not all of the ratios could provide sufficient separation between Little Boy and Fat Man devices. For example, with the $^{56}Mn/^{24}Na$, $^{24}Na/^{60}Co$, and $^{56}Mn/^{60}Co$ ratios, the ratio percentage difference is < 0.5%, as shown in Table 5-3. Therefore, they will have error bars that overlap, unlike those shown in Figure 5-10.

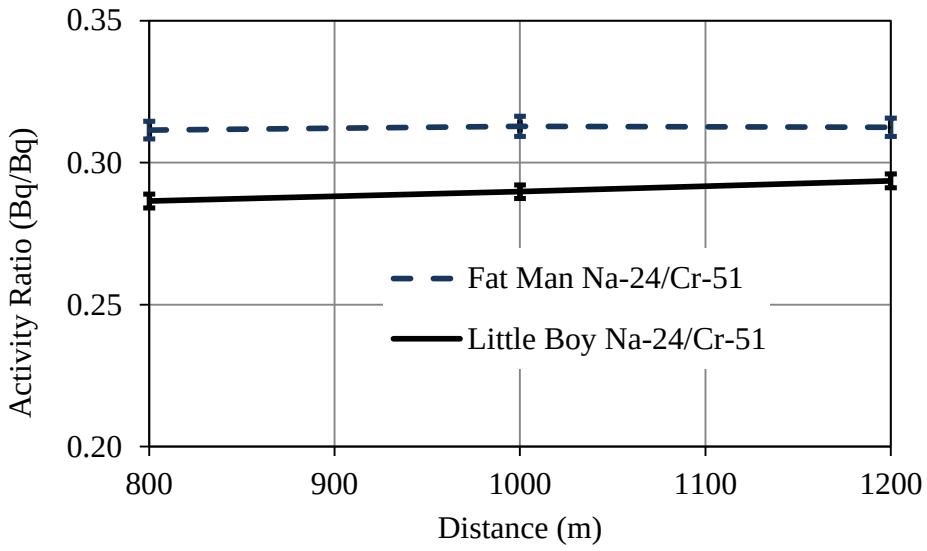

Figure 5-10. $^{24}Na/^{51}Cr$ activity ratio for 10 kt Little Boy and Fat Man type devices as a function of distance one day after exposure.

Therefore, by using the activity ratios of two radionuclides, it is feasible to determine whether a detonation is from a gun-type device or an implosion weapon. These activity ratios do vary as a function of distance.

5.5.2 Slope Method

Another approach to discriminate the fission weapon type is to use the measured activity of a specific radionuclide produced by one reaction within multiple battery samples collected at different locations. For example, Figure 5-11 shows the MCNP simulated induced number of ^{55}Mn(n,γ) reactions in the CR2032 $LiMnO_2$ battery from Little Boy and Fat Man type devices in the MD zone, together with the fitted results using Eqs. (9) and (10) presented in Section 5.3. The plot demonstrates that the number of ^{55}Mn(n,γ) reactions from the Little Boy type device decreases faster compared with Fat Man type when distance increases. This result is consistent with Eqs. (9) and (10) which indicate that the slopes for the number of reactions from Little Boy and Fat Man type weapons should be different. This is because the total number of reactions R_a is a function of total flux ϕ_T and macroscopic cross section Σ_a,

$$R_a = \phi_T \, \Sigma_a = \sum_{i=1}^{G} \phi_i(E) \, \Sigma_i(E) \tag{13}$$

where the G multigroup cross sections $\Sigma_i(E)$ and fluxes $\phi_i(E)$ are functions of energy E. Because the energy source spectrum is different for the Little Boy and Fat Man type

weapons, the distance-propagated fluxes are different, which leads to the different number of reactions. In particular, the number of ^{55}Mn(n,γ) reactions from the Little Boy type device decreases by a factor of 500 from 800 m to 1500 m, meanwhile, the Fat Man type weapon reduces by a factor of 96.6. It is also noteworthy that, as presented in Figure 5-11, the number of ^{55}Mn(n,γ) reactions per gram of Mn has a similar slope over distance as the total fluence for Little Boy type device (i.e., factor of 500 decrease). Similarly, for the Fat Man style weapon, the number of ^{55}Mn(n,γ) reactions per gram of Mn and the total fluence both reduce at the same rate (a factor of 96.6) from 800 m to 1500 m.

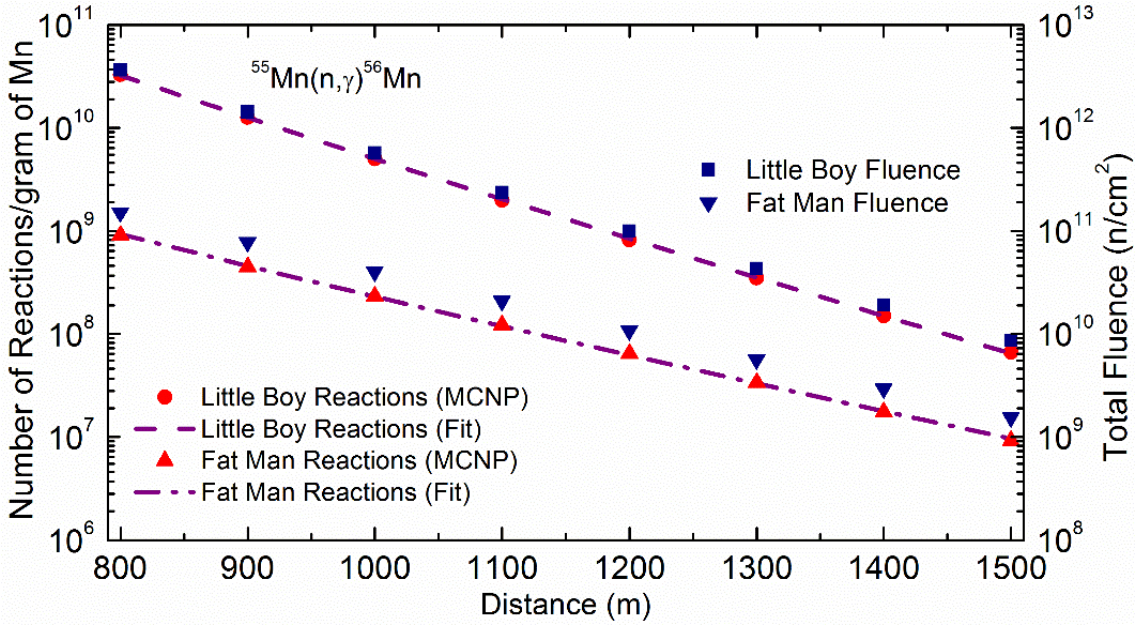

Figure 5-11. Comparison of the total number of ^{55}Mn(n,γ) reactions as computed by MCNP (symbols), the fitted equation (lines), and the total fluence as a function of distance from 800 to 1500 m for 10 kt Little Boy and Fat Man type devices.

In the real utilization of this approach in a case of nuclear detonation, with the assistance of the advanced technologies available today, the explosion time, location and the battery samples collection places can be accurately pinpointed. This indicates that the type of fission weapon can be distinguished using this method. Researchers could collect multiple battery samples at different distances, measure the ^{56}Mn activities for each battery, and calculate the slope over distances from the detonation point. By comparing the computed slope with those of Figure 5-11, one could determine whether the nuclear detonation is from a gun-type weapon, or an implosion device.

The slope method has also been studied under different humidity levels (20%, 40%, 60%, 80%, and 100%) to ascertain how humidity impacts the results of this study. The induced number of $^{55}Mn(n,\gamma)$ reactions in the CR2032 $LiMnO_2$ battery from Little Boy and Fat Man type devices are simulated in MCNP under each humidity level, and the slope of the number of $^{55}Mn(n,\gamma)$ reactions from 800 m to 1500 m are calculated. The results are plotted in Figure 5-12. The plot shows that despite the humidity level, the slope of the number of $^{55}Mn(n,\gamma)$ reactions from 800 m to 1500 m ranges from 500 to 591 for Little Boy and 96.6 to 118 for Fat Man. More importantly, the slope of the Little Boy is always 501% to 518% larger than the Fat Man cases. Therefore, the slope method can be used under a humid air situation to distinguish the Little Boy type device from the Fat Man type weapon.

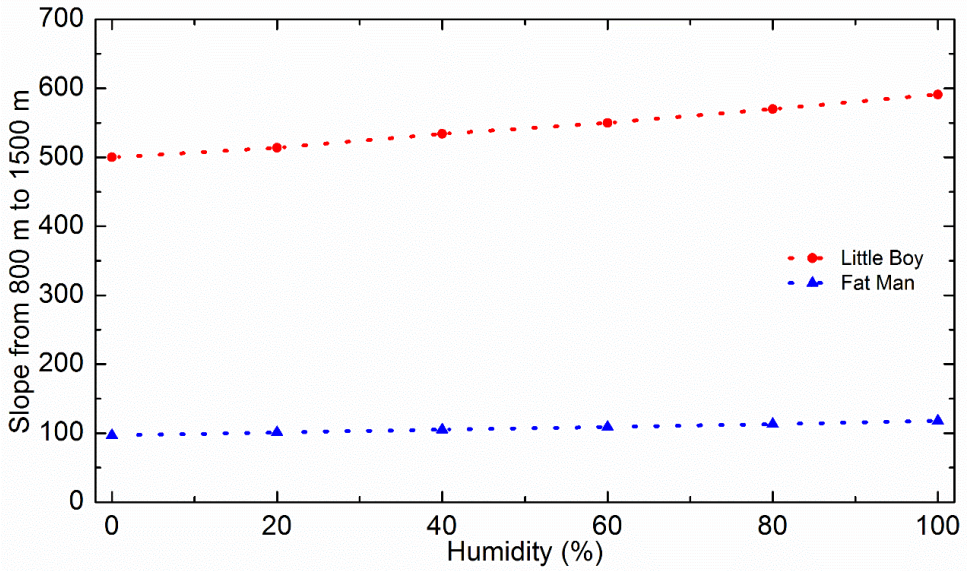

Figure 5-12. Comparison of the slope of the number of ^{55}Mn(n,γ) reactions from 800 m to 1500 m for 10 kt Little Boy and Fat Man type devices in dry, 20%, 40%, 60%, 80%, and 100% humid air.

With the weapon type determined using either of the two methods described above; one can select the corresponding equation presented in Section 5.3 and the weapon yield can be calculated accordingly.

5.6 Nuclear Weapon Spectra Reconstruction

In Chapter 4, the SNL-SAND-IV code was used to reconstruct the reactor source spectra using foils and batteries. This section will focus on reconstructing nuclear weapon spectra using Li-ion batteries. Unlike reactor experiments, it is impractical to conduct a nuclear weapon denotation experiment to collect irradiated battery samples. Therefore, MCNP was used to simulate such events. Similar to the MCNP reactor simulations presented in Section 4.2, here, the battery samples were subjected in MCNP to 10 kt Little

Boy and Fat Man type nuclear weapon explosions 1 km away in dry air. Then, the simulated battery activities were used as input to reconstruct the weapon spectra at 1 km away from the detonation point using SNL-SAND-IV. As the exposure duration during a nuclear weapon detonation is relatively short, Eq. (1) is no longer suitable to calculate the activity. Instead, since the fluence Φ is an impulse function, Eq. (14) should be used,

$$A_2(t) = n_1(0)\,\lambda_2\,\Phi\,\sigma_a^1\,e^{-\lambda_2 t} \tag{14}$$

where 1 and 2 represent the target and activated product, respectively, and *t* is the time since detonation. The derivations of Eqs. (1) and (14) can be found in Appendix D.

5.6.1 Weapon Spectra Reconstruction with Ultrathin Battery

Since the MEC 201 battery matches very well with the foils reconstructed results for the reactor experiments, it is first used for nuclear weapon spectra reconstructions. The same five reactions, as shown in Table 4-7, used to reconstruct the UMass experiment spectrum were utilized in this reconstruction as well. At first, the battery is subjected to the neutrons transported in the MCNP simulation for a 10 kt Fat Man type weapon detonation, 1 km away in dry air. Then, the simulated activities for those five reactions were used as input to the SNL-SAND-IV code, along with the Fat Man reference spectrum, for reconstruction. After that, in order to further examine how sensitive the SNL-SAND-IV results are to the initial input spectrum, the input spectrum was changed to a Little Boy type reference spectrum, while keeping the activities the same. It is noteworthy that the neutron

spectra obtained from MCNP simulation output are in the units of n/(cm^2), whereas the input and output spectra of SNL-SAND-IV are in the form of n/(cm^2·MeV), that is, differential spectra. Therefore, MCNP simulated spectrum results need to be transferred into per MeV values before being used for reconstruction and comparison; this is readily accomplished by dividing the n/cm^2 values by the energy bin width. The reconstructed results for both cases are plotted as Figure 5-13, along with the MCNP simulated spectra for Little Boy and Fat Man type devices, 1 km away. The graph shows that both reconstruction results converge to the Fat Man spectrum at 1 km, no matter which initial reference spectra were used. In particular, the calculated total neutron fluences are 4.0×10^{10}, 3.9×10^{10}, and 3.6×10^{10} n/(cm^2), for the reference Fat Man spectrum, and reconstructions using Fat Man and Little Boy as the initial spectrum, respectively. In other words, the differences between the reference and the reconstructed spectra using Fat Man and Little Boy type weapon as initial guesses are 2.5% and 11%, respectively. This indicates that the initial input spectrum does not have to be perfect to obtain the correct result. The plot shows that the reconstructed spectra effectively overlay the MCNP estimated reference spectrum, which means that the thin MEC201 battery can be used to effectively reconstruct the weapon spectrum.

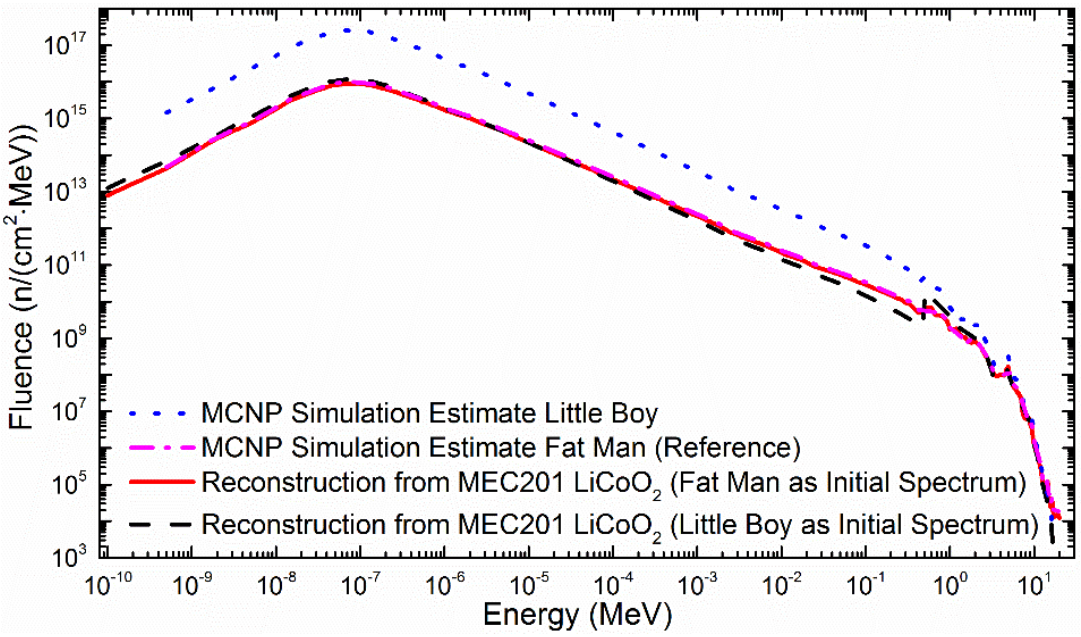

Figure 5-13. Neutron spectrum from SNL-SAND-IV reconstruction of Fat Man type weapon from MEC201 battery using the MCNP simulated activities but different initial spectra, with a comparison to the MCNP estimated reference weapon spectra for 10 kt Little Boy and Fat Man type devices at 1 km.

The same effort was make to reconstruct the Little Boy type device spectrum using the MEC201 battery as well. This time, the battery is subjected to the neutrons transported in the MCNP simulation for a 10 kt Little Boy type weapon detonation, 1 km away in dry air. Again, both a 10 kt Little Boy and a Fat Man type weapon spectra at 1 km were used as the initial spectral input, and the results are shown as Figure 5-14. Unsurprisingly, both reconstructed spectra match well with the reference spectrum of the Little Boy type device. Actually, in real practice, the correct weapon type should have already been determined by using the methods presented in Section 5.4. Hence, the correct input spectrum can be used at the beginning to minimize the error and achieve the best reconstruction result. In this

case, the calculated total neutron fluences for the reference Little Boy type spectrum and reconstruction using correct Little Boy type device as the initial input spectrum are 5.8×10^{11} and 5.7×10^{11} n/(cm^2), respectively. That is only a 0.49% difference. This further confirms that the thin batteries can be used to reconstruct the weapon spectrum.

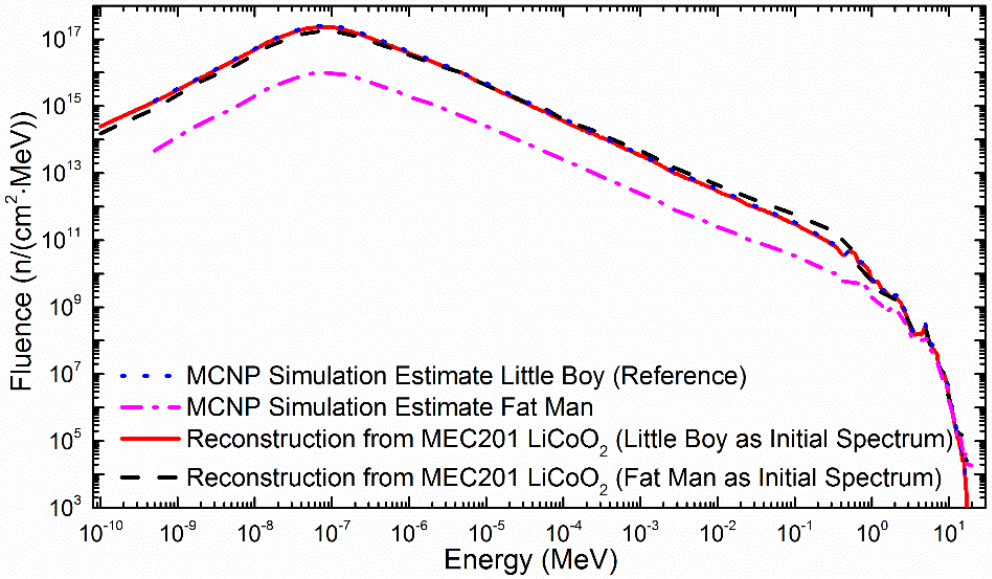

Figure 5-14. Neutron spectrum from SNL-SAND-IV reconstruction of Little Boy type device from MEC201 battery using the MCNP simulated activities but different initial spectra, with a comparison to the MCNP estimated reference weapon spectra for 10 kt Little Boy and Fat Man type weapons at 1 km.

5.6.2 Weapon Spectra Reconstruction with Thin Battery

Next, the thicker ML-2020 battery used in the reactor experiment spectrum reconstruction is also used to reconstruct the weapon spectrum as well. In similar fashion as above, the ML-2020 battery is first used to reconstruct the Little Boy type weapon spectrum, and the result is shown in Figure 5-15. As expected, the reconstructed spectra

converge to the Little Boy type reference spectrum regardless of the initial input. Even though there is some oscillation at the higher energy, one can easily distinguish that the reconstructed spectrum matches the Little Boy type device, instead of a Fat Man weapon.

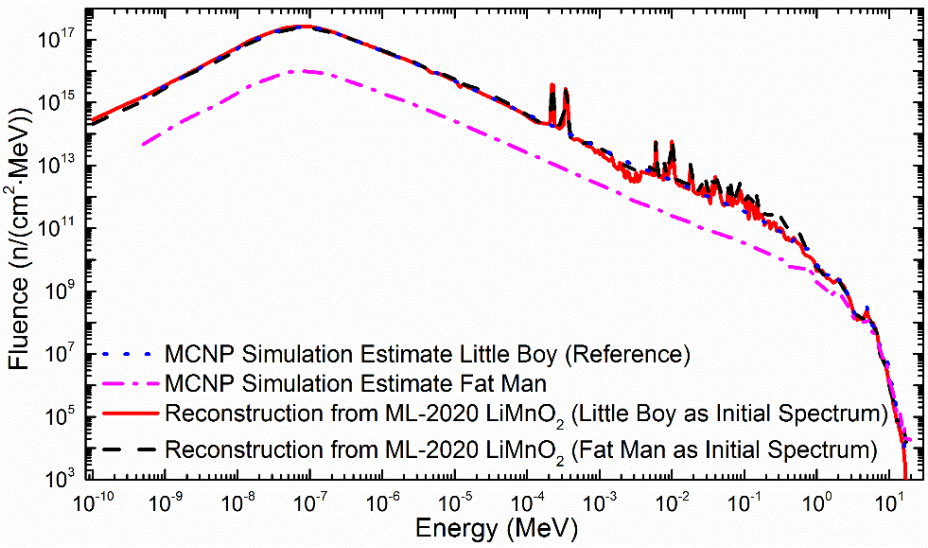

Figure 5-15. Neutron spectrum from SNL-SAND-IV reconstruction of Little Boy type device from ML-2020 battery using the MCNP simulated activities but different initial spectra, with a comparison to the MCNP estimated reference weapon spectra for 10 kt Little Boy and Fat Man type weapons at 1 km.

Then, ML-2020 battery is also used to reconstruct the Fat Man type device spectrum. The result is shown as Figure 5-16. Unsurprisingly, the reconstructed spectra converge to the Fat Man type reference spectrum no matter what the initial input spectrum is. Similar to the Little Boy spectrum reconstruction results using ML-2020, the trend, shape, and magnitude of the reconstructed spectra are very similar to the reference spectrum, except some oscillations at higher energies. The ML-2020 battery used 11

reactions for reconstruction, while the thinner MEC201 battery used only 5 reactions. Just like in Figure 4-3 where 10 foil reactions were used to reconstruct the reactor spectrum, these additional reactions lead to the introduction of the additional fitting features (deviations). However, it does not impair the ability to discriminate the Little Boy versus Fat Man type weapon.

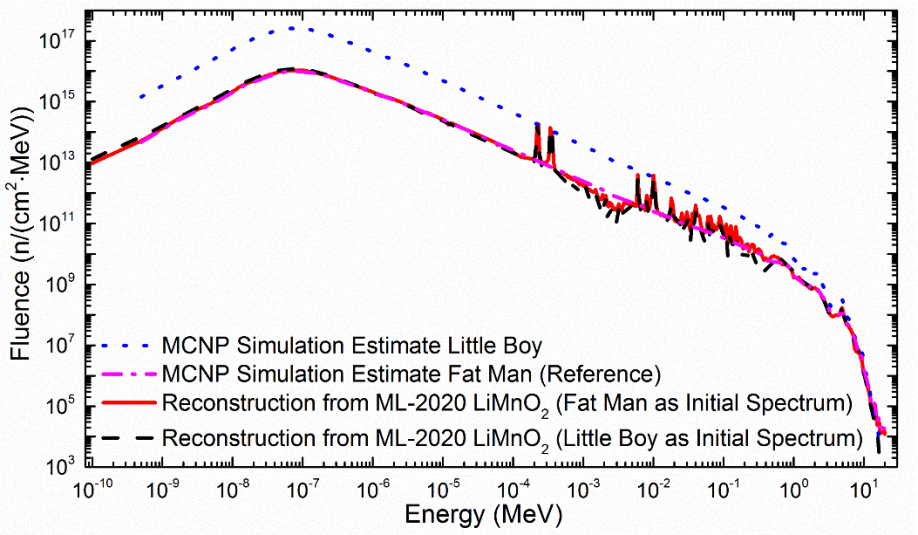

Figure 5-16. Neutron spectrum from SNL-SAND-IV reconstruction of Fat Man type device from ML-2020 battery using the MCNP simulated activities but different initial spectra, with a comparison to the MCNP estimated reference weapon spectra for 10 kt Little Boy and Fat Man type weapons at 1 km.

5.6.3 Weapon Spectra Reconstruction with Combined Battery

In the real utilization of this approach, multiple battery samples will be exposed to the same incident spectrum and collected for analysis. Therefore, the activities of both MEC201 and ML-2020 batteries are combined together to reconstruct the neutron

spectrum, just like for the reactor spectrum reconstruction in Section 4.3.2. The two batteries have 12 unique reactions in total, and they are all used in the reconstructions. First, the activities from the MCNP Little Boy 1 km simulation were utilized. Similar to the reconstruction using a single battery, both Little Boy and Fat Man spectra were used as SNL-SAND-IV input initial spectrum. The overall SNL-SAND-IV calculated activities are within 1.6% of the MCNP simulated activities for both cases. The reconstructed results are shown as Figure 5-17. The reconstructed results look similar to the results using the thicker ML-2020 battery alone. Regardless of the input spectrum, the results match with the Little Boy spectrum. There are oscillations at higher energy range, however, not enough to blur the judgement of Little Boy versus Fat Man spectrum.

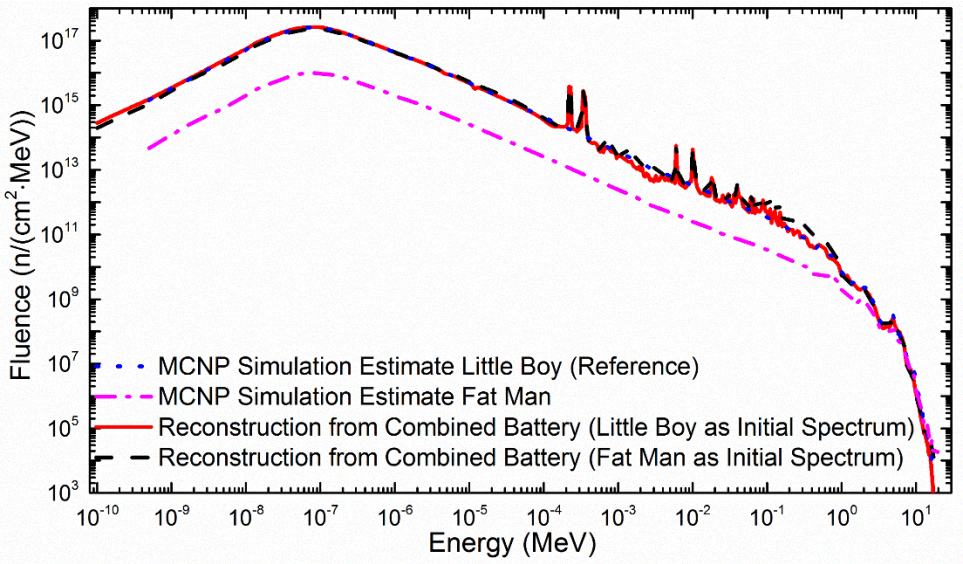

Figure 5-17. Neutron spectrum from SNL-SAND-IV reconstruction of Little Boy type device from MEC201 and ML-2020 combined battery using the MCNP simulated activities but different initial spectra, with a comparison to the MCNP estimated reference weapon spectra for 10 kt Little Boy and Fat Man type weapons at 1 km.

Similarly, the MCNP simulated results of the Fat Man case for the combined battery are also used to reconstruct the neutron spectrum, using both Little Boy and Fat Man spectra at 1 km as SNL-SAND-IV input. This time, the overall SNL-SAND-IV calculated activities are within 0.2% of the MCNP simulated results. The reconstructed spectra are shown as Figure 5-18. As expected, both cases converge to Fat Man spectrum, and the reconstructed spectra have similar characteristics as the ML-2020 results. The reason that the combined battery results are more like the results using the ML-2020 alone might be that out of the 12 reactions of the combined battery, ML-2020 has 11 of them, whereas MEC201 has only 5. Thus, the ML-2020 battery is more dominate in the combined battery.

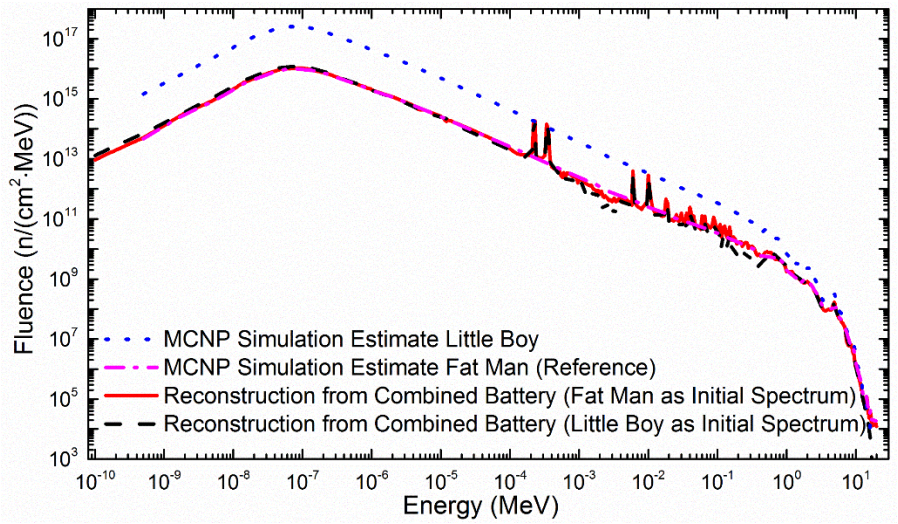

Figure 5-18. Neutron spectrum from SNL-SAND-IV reconstruction of Fat Man type device from MEC201 and ML-2020 combined battery using the MCNP simulated activities but different initial spectra, with a comparison to the MCNP estimated reference weapon spectra for 10 kt Little Boy and Fat Man type weapons at 1 km.

5.6.4 Weapon Spectra Reconstruction with Battery Next to a Water Cube

Next, efforts were made to study how the person carrying the battery will impact the reconstruction results. Since the majority of the human body is water, to simplify the simulation, a water cube is placed next to the battery to serve as a human phantom. The water cube is 70 cm × 40 cm × 20 cm to mimic the torso of an adult. First, this water cube is placed right next to the battery in the MCNP battery model of Section 3.2. Then, the battery plus water cube model is exposed to the MCNP weapon simulation model, shown as Figure 5-19, as discussed in Section 5.5.1.

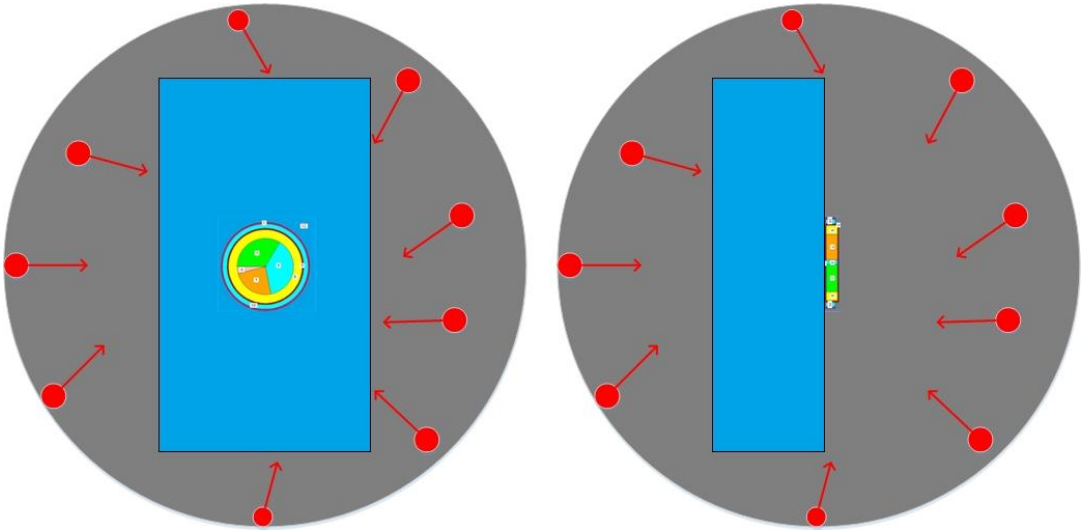

*Note: Not to scale. Battery is actually much smaller.

Figure 5-19. MCNP simulation model of battery exposed in weapon spectrum with water cube.

Similar to the reconstruction effort introduced in Section 5.5.1, the MEC201 $LiCoO_2$ battery with the water cube was first used to reconstruct the weapon spectrum at 1

km. The results are shown in Figure 5-20 and Figure 5-21, respectively, for the Little Boy and Fat Man devices. The plots show that even with the water cube placed next to the battery, the reconstructed result almost overlay with the result without the water cube, as well as the correct reference spectrum.

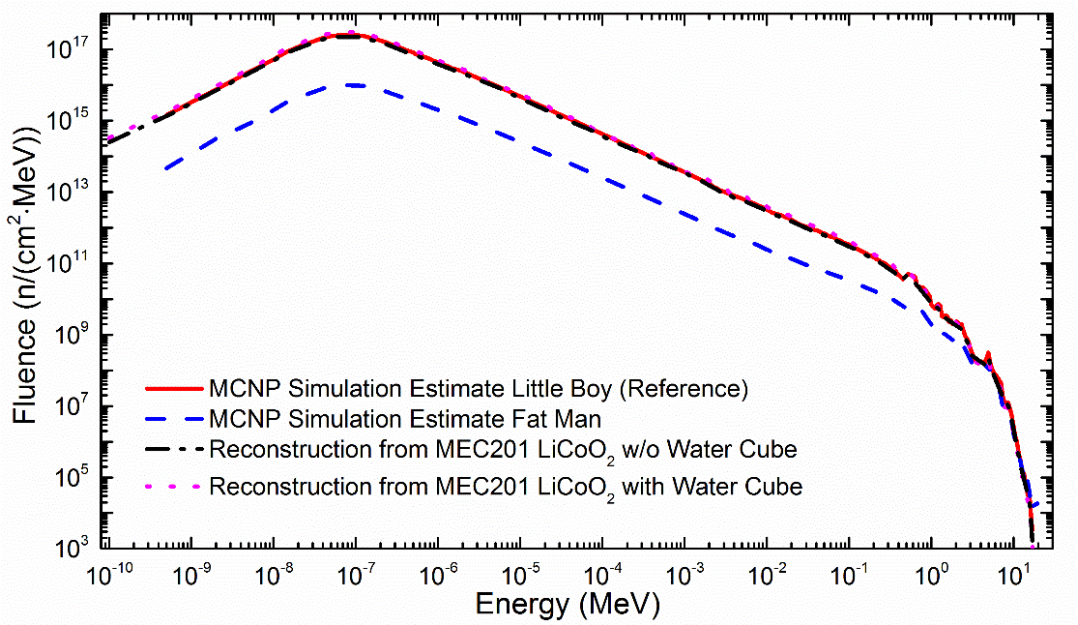

Figure 5-20. Neutron spectrum from SNL-SAND-IV reconstruction of Little Boy type device from MEC201 battery using the MCNP simulated activities with and without water cube, with a comparison to the MCNP estimated reference weapon spectra for 10 kt Little Boy and Fat Man type weapons at 1 km.

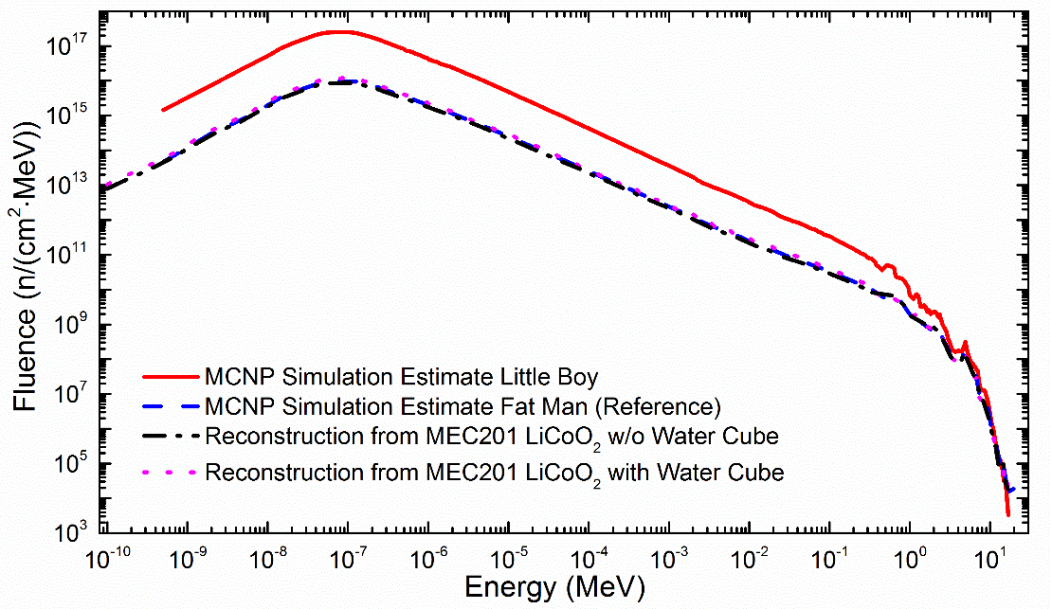

Figure 5-21. Neutron spectrum from SNL-SAND-IV reconstruction of Fat Man type device from MEC201 battery using the MCNP simulated activities with and without water cube, with a comparison to the MCNP estimated reference weapon spectra for 10 kt Little Boy and Fat Man type weapons at 1 km.

Next, similar to Section 5.5.2, the ML-2020 $LiMnO_2$ battery is used to further valid this simulation with a water cube. The results are shown as Figure 5-22 and Figure 5-23 for Little Boy and Fat Man devices, respectively. As expected, the reconstructed result with the water cube matches well with the spectrum reconstructed without the water cube, as well as the reference spectrum. This further substantiates that even with a water cube next to the battery, the Li-ion batteries are capable of reconstructing the correct weapon spectrum. In the real utilization, this means that even if the battery sample is placed next to a human, it can still be used to correctly reconstruct the incident weapon spectrum and distinguish the Little Boy type weapon from the Fat Man type device.

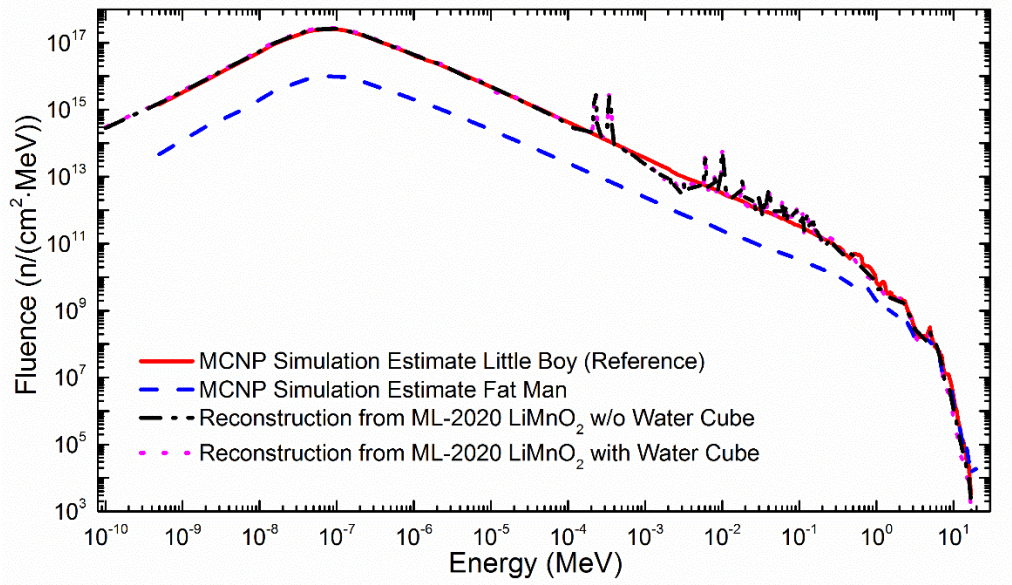

Figure 5-22. Neutron spectrum from SNL-SAND-IV reconstruction of Little Boy type device from ML-2020 battery using the MCNP simulated activities with and without water cube, with a comparison to the MCNP estimated reference weapon spectra for 10 kt Little Boy and Fat Man type weapons at 1 km.

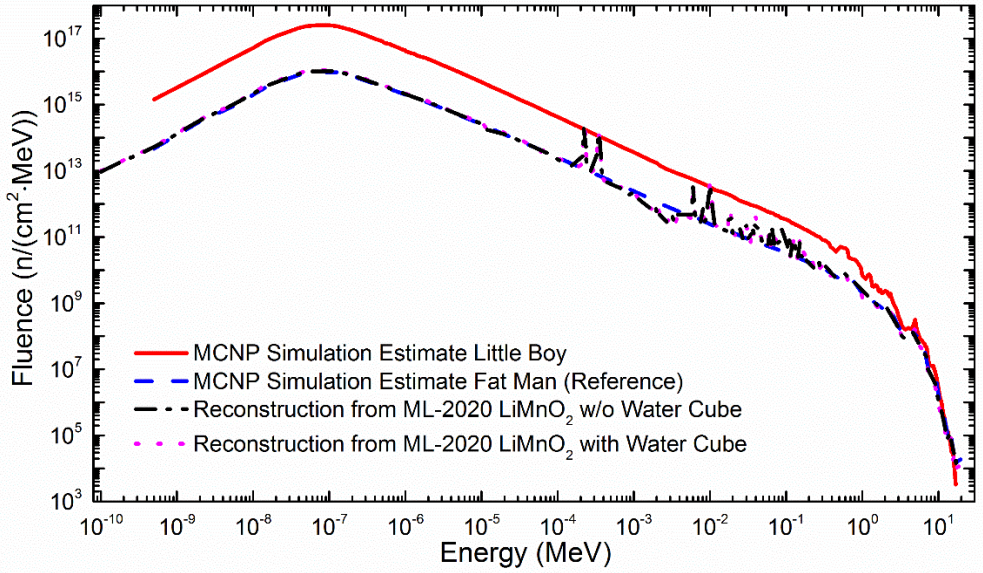

Figure 5-23. Neutron spectrum from SNL-SAND-IV reconstruction of Fat Man type device from ML-2020 battery using the MCNP simulated activities with and without water cube, with a comparison to the MCNP estimated reference weapon spectra for 10 kt Little Boy and Fat Man type weapons at 1 km.

5.7 Summary

Overall, the results presented in this chapter demonstrate that, in a case of a nuclear weapon detonation incident in an open area, the irradiated Li-ion batteries are capable of being analyzed to calculate the nuclear weapon yield, determine the device type, and reconstruct the weapon spectrum.

CHAPTER 6

CONCLUSIONS AND FUTURE WORK

This research utilizes thin Li-ion batteries as widely spread sensors for nuclear forensics. In particular, by performing post detonation analyses using irradiated Li-ion batteries after a nuclear weapon explosion, the yield, type, and the spectrum of the device can be determined.

For decades, people have been studying different ways of performing nuclear forensics. With the large deployment of consumer electronics nowadays, the Li-ion batteries are chosen in this study because the desired samples can be collected in many locations after a nuclear weapon detonation. Detailed information about representative Li-ion batteries was introduced in Chapter 3. The battery samples were first disassembled and analyzed using ICP-MS to obtain the accurate geometry and mass for each chemical element. Then, with above information available, MCNP models were built for those battery samples.

In order to validate the method, in Chapter 4, four reactor experiments were performed to irradiate the batteries. The experiments were simulated using MCNP models as well. The reactor source spectrum was first validated using the activation foils through SNL-SAND-IV reconstruction. Then, the irradiated battery activities were used to reconstruct the experiment spectrum, and the results are compared with the foils reconstructed reference. The results shows that the thin batteries are able to reconstruct

the reactor spectrum, just like the activation foils methodology, especially by using the ultrathin battery.

Next, in Chapter 5, basic information about nuclear weapons was provided. The only two nuclear weapons that have been detonated in war, Little Boy and Fat Man, were chosen for this study. Because it is unpractical to conduct a real nuclear weapon detonation for experimentation, the source spectra of those two weapon types were obtained from literature, and the incident neutron spectra at different distances from the detonation point are simulated using MCNP. Subsequently, two equations that relate the total neutron fluence and weapon yield were developed for Little Boy type and Fat Man style weapons in the MD zone (800 to 1500 m from detonation point for a 10 kt device). The Li-ion batteries were then subjected to those neutron spectra in MCNP simulations. Thereafter, two equations that relate the weapon yield to the number of reactions as a function of distance were also developed for each weapon type.

Two different methods to determine the type of nuclear weapon were presented as well. One approach uses the induced activity ratio of different radionuclides from the measurements in the post detonation analysis to distinguish the fission weapon type. The other approach utilizes the measured activity of a specific radionuclide produced by one reaction within multiple battery samples collected at different locations to discriminate the fission weapon type. Both methods provide the ability to determine the type of the nuclear weapon.

Lastly, the Li-ion batteries were used to reconstruct the weapon neutron spectrum using SNL-SAND-IV, in a similar approach as for the reactor spectrum reconstruction. The battery reconstructed results were compared with the MCNP simulated reference spectra. The result shows that the irradiated Li-ion batteries are capable of reconstructing the nuclear weapon spectrum.

In conclusion, in the case of a real nuclear weapon detonation incident, irradiated battery samples in the MD zone can be collected for post detonation analyses. By using either the slope method or the ratio method presented in this research, one can determine whether the weapon is a gun-type or an implosion-type device. Then, by using the corresponding equations developed in this study, the weapon yield can be calculated. Lastly, by utilizing the irradiated battery activities, the incident neutron spectrum can be reconstructed using SNL-SAND-IV. The most desirable battery type for determining each of the nuclear weapon characteristics is listed as Table 6-1 based on the batteries investigated in this research. In a real nuclear weapon detonation incident, the best battery samples could be separated out from all batteries collected, depending on what characteristic(s) are to be determined. In other words, this research indicates that Li-ion batteries can be used as neutron detectors to determine the yield, type, and the spectrum of nuclear weapon devices.

Table 6-1 Best Battery Choice to Determine Different Nuclear Weapon Features

Unknown	Best Battery	
Yield	Mn Based	
Device Type	Ratio Method	Steel Casing
	Slope Method	Mn Based
Spectrum	High Activity, Thin	

There are future works that can be done to further improve the methodology. As mentioned in Section 4.3.2, the $^{75}As(n,\gamma)$ and $^{187}W(n,\gamma)$ reactions are not available in the SNL-SAND-IV cross section library, and those reactions were omitted in the present work. Therefore, it is desirable to expand the SNL-SAND-IV cross section library to include these and other reactions that may be of importance in Li-ion batteries. It would be desirable to find out why including $^{58}Ni(n, p)$ and $^{63}Cu(n, \alpha)$ reactions in reconstructing the UMass reactor spectrum using the combined MEC201 and ML-2020 batteries leads to a 12% overall difference, too. In the same section, because ^{24}Na has gamma ray peaks that are located outside of the calibrated Ge detector range, including the $^{23}Na(n,\gamma)$ reaction in the spectrum reconstruction led to a large error. Hence, a better calibrated gamma ray detector should be used to measure the activities of activated battery samples in the future. The next battery type that might be studied is Li-polymer, as it is used more and more in consumer electronics. Also, it will be nice to model all the batteries inside an electronic device, such as a cell phone or music player, in the future work. Just like the iPod and iPod Li-polymer battery exposed during the second UMass experiment, if the stainless steel

casing edition iPod is used, people may be able to determine the nuclear weapon type using the $^{59}Fe/^{51}Cr$ activity ratio method, without taking the battery out to measure.

A lesson learned during this research is that it is very beneficial to have at least one colleague to present during the reactor experiments. During the two OSU experiments, no team members were sent there in order to reduce the cost. When analyzing the irradiated battery samples after the experiments, there are always some missing pieces of information. Another lesson learned from the two OSU experiments is that foils should have also been irradiated so that activation analysis could be performed to obtain accurate information about the reactor, such that the reconstructed reactor spectrum using SNL-SAND-IV could be readily compared. With these lessons learned, the latter two UMass experiments irradiated ten foils along with the batteries each time, and were actually performed by one of our colleagues in Boston, which provided more detailed information to support the research. Also, it is highly desirable to have a "battery material library" in which the accurate constituency of each battery type are listed. This could eliminate the time required and the errors introduced during (1) disassembling the battery in preparation for ICP-MS analysis, and (2) performing the ICP-MS analysis. By having a more accurate battery constituency, the MCNP battery models are more precise, which will reduce the error of the post detonation analysis as a result.

REFERENCES

[1] "North Korea conducts fourth nuclear test, claims to have H-bomb technology," The Japan Times, 6 January 2016. [Online]. Available: http://www.japantimes.co.jp/news/2016/01/06/asia-pacific/north-korean-nuclear-test-suspected-artificial-earthquake-detected-near-atomic-site/#.VwNe6PkrKUk. [Accessed 4 April 2016].

[2] J. Mullen, "North Korea says it can miniaturize nuclear weapons," CNN, 20 May 2015. [Online]. Available: http://edition.cnn.com/2015/05/20/asia/north-korea-nuclear-weapons/. [Accessed 4th April 2016].

[3] "Nuclear Security Summit 2016," [Online]. Available: http://www.nss2016.org/. [Accessed 4 April 2016].

[4] K. Kwon and D. Ford, "North Korea: Nukes need to be ready for use," CNN, 4 March 2016. [Online]. Available: http://www.cnn.com/2016/03/03/asia/north-korea-nuclear-warheads/. [Accessed 4 April 2016].

[5] S. Lewis, "North Korea's Kim Jong Un Orders More Nuclear Weapons Tests," Time, 10 March 2016. [Online]. Available: http://time.com/4255081/north-korea-kim-jong-un-nuclear-tests/. [Accessed 4 April 2016].

[6] "Iraq rebels 'seize nuclear materials'," BBC, 10 July 2014. [Online]. Available: http://www.bbc.com/news/world-middle-east-28240140. [Accessed 4 April 2016].

[7] O. Beck, "ISIS Plundered Nuclear Material That Could Be Used in Weapons," Vice News, 10 July 2014. [Online]. Available: https://news.vice.com/article/isis-plundered-nuclear-material-that-could-be-used-in-weapons. [Accessed 4 April 2016].

[8] L. Moftah, "ISIS Nuclear Weapon? Islamic State Claims It Can Buy Nukes From Pakistan Within A Year In Dabiq Propaganda Magazine," International Business Times, 23 May 2015. [Online]. Available: http://www.ibtimes.com/isis-nuclear-weapon-islamic-state-claims-it-can-buy-nukes-pakistan-within-year-dabiq-1936029. [Accessed 4 April 2016].

[9] J. A. Siegel and K. Mirakovits, Forensic Science: The Basics, 3rd ed., CRC Press, 2015.

[10] Nuclear Forensics Support, Vienna: International Atomic Energy Agency, 2006.

[11] The Convention on the Physical Protection of Nuclear Material, Vienna: International Atomic Energy Agency, 1980.

[12] Nuclear Forensics in Support of Investigations, Vienna: International Atomic Energy Agency, 2015.

[13] J. Qiu, L. Cao, P. Mulligan, D. Turkoglu, S. C. Nagpure, M. Canova and A. Co, "The Potential of Using Li-Ion Batteries for Radiation Detection," *IEEE Transactions on Nuclear Science,* vol. 60, no. 2, pp. 662-667, April 2013.

[14] N. J. Dorrell, "Retrospective Thermal Neutron Fluence Determination Using Lithium-Ion Mobile Telephone Batteries," MS Thesis, Oregon State University, 2011.

[15] G. G. Eichholz and J. W. Poston, Principles of Nuclear Radiation Detection, Ann Arbor: Ann Arbor Science Publisher, Inc., 1979.

[16] S. Tripathy, C. Sunil, M. Nandy, P. Sarkar, D. Sharma and B. Mukherjee, "Activation Foils Unfolding for Neutron Spectrometry: Comparison of Different Deconvolution Methods," *Nuclear Instruments and Methods in Physics Research A,* vol. 583, no. 2-3, pp. 421-425, 2007.

[17] Glenn F. Knoll, Radiation Detection and Measurement, 3rd ed., New York: John Wiley & Sons, Inc., 2000.

[18] W. N. McElroy, S. Berg and T. Crockett, "A Computer-Automated Iterative Method for Neutron Flux Spectra Determination by Foil Activation," Air Force Weapons Laboratory, 1967.

[19] S. I. Tanaka, "Summary of the JCO Criticality Accident in Tokai-mura and a Dose Assessment," *Journal of Radiation Research,* vol. 42, pp. S1-S9, September 2001.

[20] K. Fujimoto, ed, "Final report on dose estimation for three victims of JCO accident," National Institute of Radiological Sciences, 2002..

[21] M. Kohno and Y. Koizumi, "Neutron Dose Estimates from 5-Yen Coins," *Nature,* vol. 406, p. 693, 2000.

[22] J. Gasparro, M. Hult, K. K. D. Arnold, L. Holmes, P. Johnston, M. Laubenstein, S. Neumaier, J.-L. Reyss, P. Schillebeeckx, H. Tagziria, G. Van Britsom and R. Vasselli, "Measurements of 60Co in Spoons Activated by Neutrons During the JCO Criticality Accident at Tokai-mura in 1999," *Journal of Environmental Radioactivity,* vol. 73, pp. 307-321, 2004.

[23] M. May, J. Davis and R. Jeanloz, "Preparing for the Worst," *Nature*, vol. 443, pp. 907-908, 2006.

[24] National Security Staff Interagency Policy Coordination Subcommittee, Planning Guidance for Response to a Nuclear Detonation, 2nd ed., 2010.

[25] H. L. Brode, "Review of Nuclear Weapons Effects," *Annual Review of Nuclear Science,* vol. 18, pp. 153-202, 1968.

[26] B. Watt, "Energy Spectrum of Neutrons from Thermal Fission of U^{235}," *Physical Review,* vol. 87, no. 6, pp. 1037-1041, 1952.

[27] J. Watterson, "The Fission Spectrum," Indico, 2007.

[28] D. P. Kroese, T. Brereton, T. Taimre and Z. I. Botev, "Why the Monte Carlo Method is so Important Today," *WIREs Computational Statistics*, vol. 6, no. 6, pp. 386-392, 2014.

[29] D. E. Raeside, "Monte Carlo Methods," in *Handbook of Radiation Measurement and Protection*, vol. II, A. Brodsky, Ed., Boca Raton, Florida: CRC Press, 1982, pp. 591-595.

[30] J. K. Shultis and R. E. Faw, "An MCNP Primer," Manhattan, KS, 2010.

[31] X.-5. M. C. Team, MCNP — A General Monte Carlo N-Particle Transport Code, Version 5, Los Alamos National Laboratory, 2008.

[32] A. E. Profio, Radiation Shielding and Dosimetry, John Wiley & Sons, 1979.

[33] D. G. Miller, Radioactivity and Radiation Detection, Gordon and Breach Science Publishers, 1972.

[34] G. Gilmore and J. D. Hemingway, Practical Gamma-Ray Spectrometry, John Wiley & Sons, 1995.

[35] "Cellphone Battery Market Steadies," 12 January 2007. [Online]. Available: www.eetasia.com/ART_8800449124_499486_NT_6dc4206b.HTM. [Accessed 25 April 2016].

[36] A. Kaczmarowski, "Use of Lithium Ion Batteries for Nuclear Forensic Applications," Arizona State University, Tempe, 2012.

[37] "Oregon State TRIGA Reactor," Oregon State University, [Online]. Available: http://radiationcenter.oregonstate.edu/content/oregon-state-triga-reactor-0. [Accessed 01 June 2016].

[38] "Neutron Facilities," University of Massachusetts Lowell, [Online]. Available: https://www.uml.edu/Research/RadLab/Neutron-Facilities.aspx. [Accessed 1 June 2016].

[39] "Welcome to PeakEasy Home Page," Los Alamos Natinal Laboratory, [Online]. Available: https://peakeasy.lanl.gov/. [Accessed 5 June 2016].

[40] R. Schickler, W. Marcum and S. Reese, "Comparison of HEU and LEU neutron spectra in irradiation facilities at the Oregon State TRIGA® Reactor," *Nuclear Engineering and Design*, vol. 262, p. 340–349, September 2013.

[41] J. R. White, A. Jirapongmed, L. Bobek and T. M. Regan, "Design and Initial Testing of an Ex-Core Fast Neutron Irradiator or the UMass-Lowell Research Reactor," in *Radiation Protection and Shielding Topical Conference*, Santa Fe, 2002.

[42] W. McElray, S. Berg, T. Crockett and R. Hawkins, "A Computer Automated Iterative Method for Neutron Flux Spectra Determination by Foil Activation," Air Force Weapons Laboratory, New Mexico, 1967.

[43] P. Griffin, J. Kelly and J. VanDenburg, "User's Manual for SNL-SAND-II Code," Sandia National Laboratories, New Mexico, 1994.

[44] "National Nuclear Data Center," Brookhaven National Laboratory, 22 December 2011. [Online]. Available: http://www.nndc.bnl.gov/exfor/endf00.jsp. [Accessed 10 December 2016].

[45] C. Sublette, Nuclear weapons frequently asked questions, The Nuclear Weapon Archive: A Guide to Nuclear Weapons, 2001.

[46] S. Glasstone, The effects of nuclear weapons, US Department of Defense, 1964.

[47] "Science Behind the Atom Bomb," Atomic Heritage Foundation, [Online]. Available: http://www.atomicheritage.org/history/science-behind-atom-bomb. [Accessed 01 08 2016].

[48] Z. Masiza, A chronology of South Africa's nuclear program, vol. 1, The Nonproliferation Review, 1993, pp. 34-53.

[49] J. Hakim, A History of US: War, Peace, and All That Jazz: 1918-1945, New York: Oxford University Press, 2012.

[50] S. W. White, P. P. Whalen and A. R. Heath, "Source term evaluations, Chap. 2, Reassessment of the atomic bomb radiation dosimetry for Hiroshima and Nagasaki, Dosimetry System 2002," *Radiation Effects Research Fundation,* vol. 1, 2005.

[51] P. Whalen, "Source Terms for the Initial Radiations," *U.S.–Japan Joint Workshop of the Reassessment of A-Bomb Radiation Dosimetry in Hiroshima and Nagasaki, Nagasaki, Japan,* 1983.

[52] W. Preeg, "Neutron and Gamma-Ray Output for Fat Man and Little Boy. Reevaluations of Dosimetric Factors, Hiroshima and Nagasaki.," *DOE Symposium Series 55,* 1976.

[53] K. E. Holbert, T. Zhang, T. Stannard and E. B. Johnson, "Feasibility of using LiMnO2 batteries for nuclear forensics," in *2013 IEEE Nuclear Science Symposium and Medical Imaging Conference (2013 NSS/MIC)*, Seoul, South Korea, 2013.

[54] "Relative humidity," Lenntech, [Online]. Available: http://www.lenntech.com/calculators/humidity/relative-humidity.htm. [Accessed 20 December 2016].

[55] R. C. Weast and D. R. Lide, Handbook of Chemistry and Physics, Boca Raton, Florida: CRC Press Inc., 1986.

[56] K. Holbert, T. Stannard, T. Zhang, A. Christie and E. B. Johnson, "Discriminating fission weapons using lithium-ion batteries," in *Transactions of the American Nuclear Society*, Washington D.C., vol. 109, p. 501-503, 2013.

[57] J. Haby, "Why is Moist Air Less Dense than Dry Air at Same Temperature," [Online]. Available: http://www.theweatherprediction.com/habyhints/260/. [Accessed 10 December 2016].

APPENDIX A

ICP-MS RESULTS FOR LI-ION BATTERIES

A.1. LIR2032 $LiCoO_2$ Battery

Element	$LiCoO_2$ Positive Electrode	Foil--Shiny	Square Foil #2	Aluminum Foil	LiCo+ Cellulose	Copper	Carbon	Negative Electrode
Mass (mg)	900	9	7	366	117	98	146	706
Fe	893719.35	4884.79	4275.31	520.84	347.67	BDL	217.50	875353.41
Cr	297385.49	183.53	105.75	8.48	84.74	30.21	51.55	265549.99
Co	2357.24	263.38	185512.31	576556.81	2246.82	45.35	351.37	2221.47
Cu	3603.35	220.46	654.47	2234.36	9144.20	1756920.18	26716.06	2247.72
Ni	123262.92	108.45	199.62	51.92	42.92	77.62	35.56	114559.93
O	0.00	0.00	0.00	313052.00	0.00	0.00	0.00	0.00
P	522.04	10948.26	9018.18	4130.82	19454.17	971.60	10986.50	461.22
Al	4034.83	1027527.03	841214.91	140993.39	BDL	BDL	BDL	BDL
C	0.00	0.00	132318.80	0.00	0.00	0.00	32497.50	0.00
Li	106.20	3072.83	20906.85	52599.11	7890.87	278.30	5772.12	77.08
Mn	11090.77	41.45	66.35	110.03	5.58	16.21	6.21	12463.62
Na	BLQ	271.07	337.62	353.28	535.43	BDL	352.38	BLQ
Mo	2343.54	19.14	11.67	1.39	2.10	14.31	6.45	761.18
V	1264.11	129.16	196.69	26.83	2.65	2.84	4.53	1155.02
K	205.54	224.70	814.71	160.30	158.76	214.53	187.80	125.09
Ti	BLQ	198.98	391.32	731.75	77.87	15.95	89.23	BLQ
Zn	21.93	677.25	834.41	41.85	123.85	338.46	104.06	22.73
W	163.93	3.50	2.66	0.69	0.67	0.26	0.63	65.21
Nb	54.33	0.65	0.46	0.10	0.29	BLQ	0.46	30.75
Mg	BDL	1340.26	1970.70	BLQ	BDL	BDL	BDL	BDL

Element	$LiCoO_2$ Positive Electrode	Foil--Shiny	Square Foil #2	Aluminum Foil	LiCo+ Cellulose	Copper	Carbon	Negative Electrode
Ce	0.05	2.61	1.37	0.28	1.08	0.05	2.64	0.04
Ba	BLQ	0.78	1.27	1.31	0.90	0.37	2.21	BDL
La	0.04	2.13	0.75	0.15	0.79	0.04	1.65	0.03
Cd	3.80	BLQ	BLQ	BDL	BDL	BLQ	BLQ	1.18
Nd	BLQ	0.78	0.27	0.08	0.42	BLQ	1.01	BDL
Pb-208	0.13	9.14	5.91	1.32	0.26	0.10	0.35	1.03
Sr	BDL	BLQ	0.23	0.31	0.33	BLQ	0.82	BDL
Pb-207	BLQ	8.89	5.79	1.31	0.26	BLQ	0.34	1.01

A.2. CR2032 $LiMnO_2$ Battery

Element	Panasonic Pellet	Positive Tab	Negative Tab	Metal Screen	Negative Electrode Casing
Mass (mg)	21	1129	101	847	687
Fe	BDL	1083796.50	914942.32	241749.35	723988.89
Cr	BDL	269125.09	227349.07	61037.03	179927.42
Mn	390000.00	14886.64	12344.82	13209.93	10062.45
Al	BDL	166.35	161.12	706880.08	424.34
O	300000.00	BDL	BDL	BDL	BDL
Ni	BDL	146948.22	121810.03	39812.12	92664.12
F	180000.00	BDL	BDL	BDL	BDL
C	120000.00	BDL	BDL	BDL	BDL
Mo	BDL	2735.35	2264.56	6954.11	1796.14
Li	BDL	3.54	2.88	39170.31	80.65
Cu	BDL	4106.50	3386.14	850.51	3376.63
Co	BDL	1872.32	1551.96	835.61	1624.71
V	BDL	861.70	726.51	313.21	699.07
Sn	BDL	3173.36	5956.95	23.79	87.28
P	BDL	476.62	385.89	111.25	348.81
K	BDL	BDL	BDL	BDL	BDL
S	1000.00	BDL	BDL	BDL	BDL
Cl	750.00	BDL	BDL	BDL	BDL
W	BDL	201.89	165.79	101.74	319.76
Na	BDL	146.98	164.59	146.89	48.54
Ge	BDL	96.79	78.78	26.40	75.54
Ga	BDL	38.29	31.83	64.18	28.04
As	BDL	39.94	32.63	11.04	28.98
Zn	BDL	22.85	245.78	21.14	11.02
Ca	BDL	53.77	73.26	37.62	BDL
Ru	BDL	28.90	27.75	1.35	24.12
Ti	BDL	4.88	3.52	129.42	8.62
Cd	BDL	3.27	2.68	8.45	2.13
Sb	BDL	13.99	11.62	3.14	12.48
Hg	BDL	6.51	4.97	2.93	8.70
Mg	BDL	5.79	5.24	3.72	2.53
Pb	BDL	0.60	0.48	5.97	0.11
Rb	BDL	1.62	1.50	0.19	1.21

Element	Panasonic Pellet	Positive Tab	Negative Tab	Metal Screen	Negative Electrode Casing
Re	BDL	0.36	0.30	1.07	0.31
Zr	BDL	1.38	0.76	3.41	0.27
Ba	BDL	0.31	0.33	3.88	0.21
Ta	BDL	0.03	0.01	0.08	1.21
Au	BDL	0.76	0.56	0.34	0.29
Rh	BDL	0.36	0.33	0.04	0.34

A.3. MEC201 $LiCoO_2$ Battery

Element	Silver Side	Green Side
Mass (mg)	279	161
Cu	565713.15	759614.10
Ni	423967.11	81555.58
Co	23247.38	67.02
Mn	13220.61	1.37
Li	9347.88	5321.55
Fe	4003.12	40.16
Ti	2057.70	2.76
P	1451.76	443.86
Al	1445.85	122.36
Cr	295.74	67.99
Na	122.85	121.96
Zn	189.85	12.86
Mg	76.35	3.44
Ca	41.93	41.17
Sn	25.80	2.15
Mo	24.21	2.95
Pb	22.26	0.51
Pd	11.14	15.77
Se	19.89	BDL
As	10.13	0.53
K	BDL	14.75
Rh	5.06	7.12
Ge	4.46	4.32
Au	1.04	6.37
Sb	4.51	0.06
V	2.77	0.11
W	2.64	0.17
Ru	1.06	0.35
Te	1.14	BDL

Note:
BDL: Below Detection Limit; BLQ: Below the Limit of Quantitation. BDL means that the quantity is lower than the minimum detection limit; whereas BLQ means that the mass is so small that it cannot be quantified.

APPENDIX B

GAMMA SPECTRA OF BATTERIES EXPOSED IN EXPERIMENTS

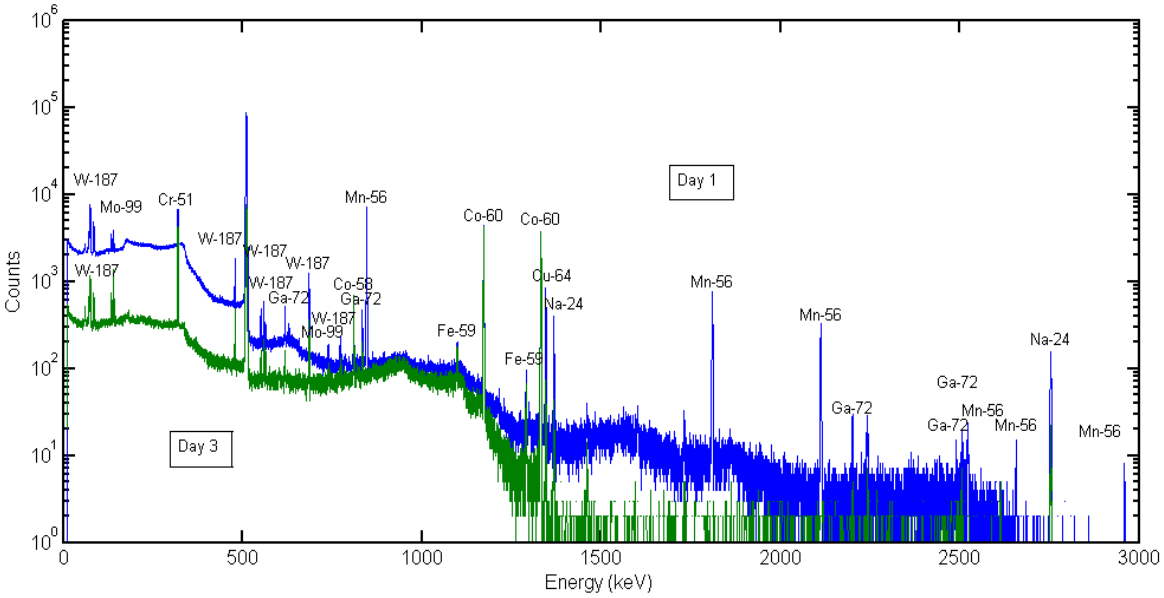

Figure B-1. Gamma ray spectra of a LIR2032 $LiCoO_2$ battery obtained 1 day and 3 days after the first OSU reactor experiment.

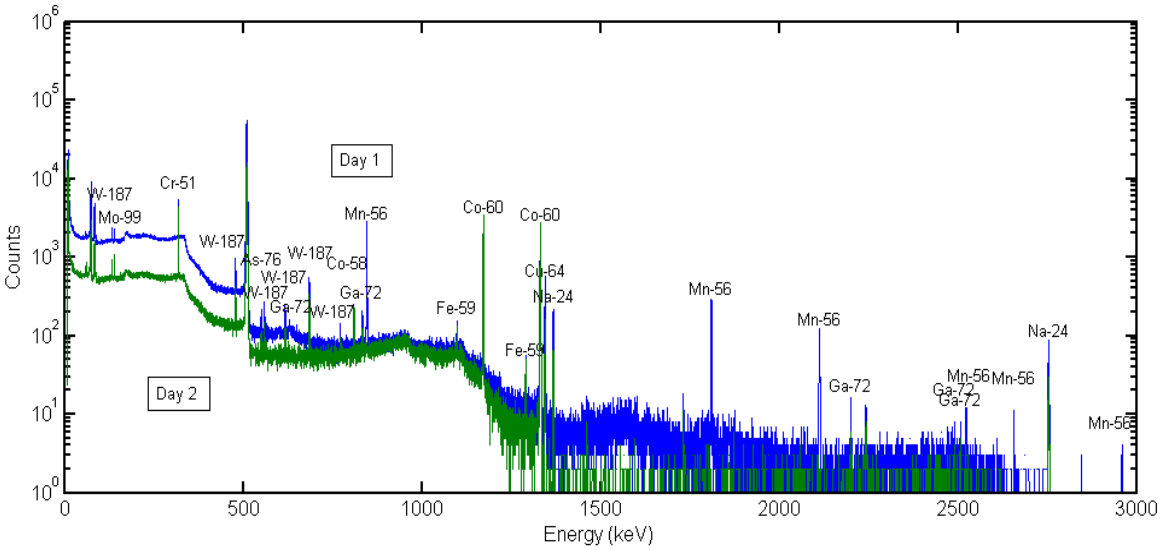

Figure B-2. Gamma ray spectra of a LIR2032 $LiCoO_2$ battery obtained 1 day and 2 days after the second OSU reactor experiment.

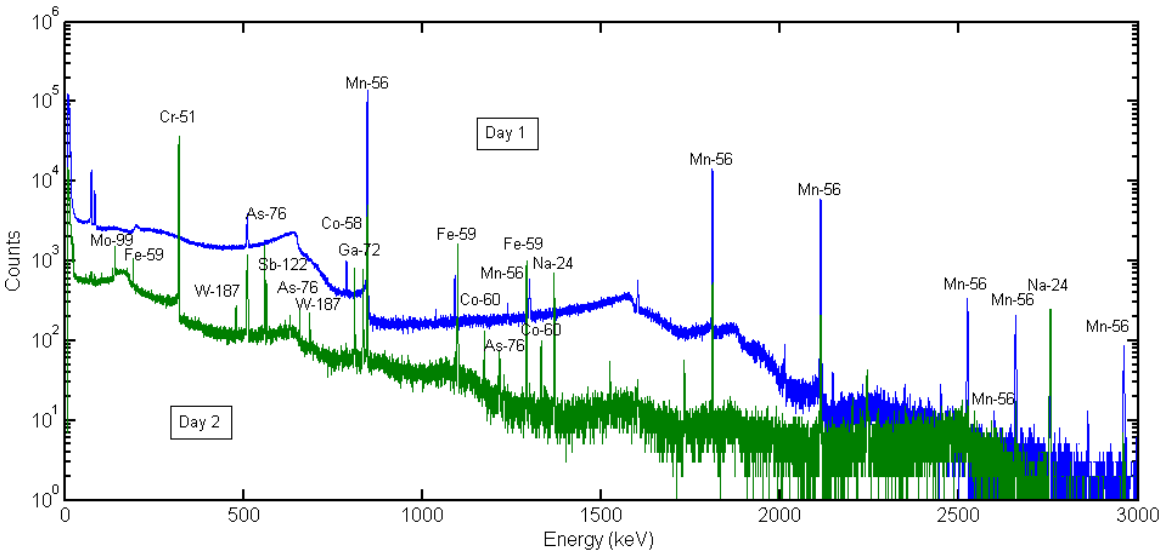

Figure B-3. Gamma ray spectra of a CR2032 $LiMnO_2$ battery obtained 1 day and 2 days after the second OSU reactor experiment.

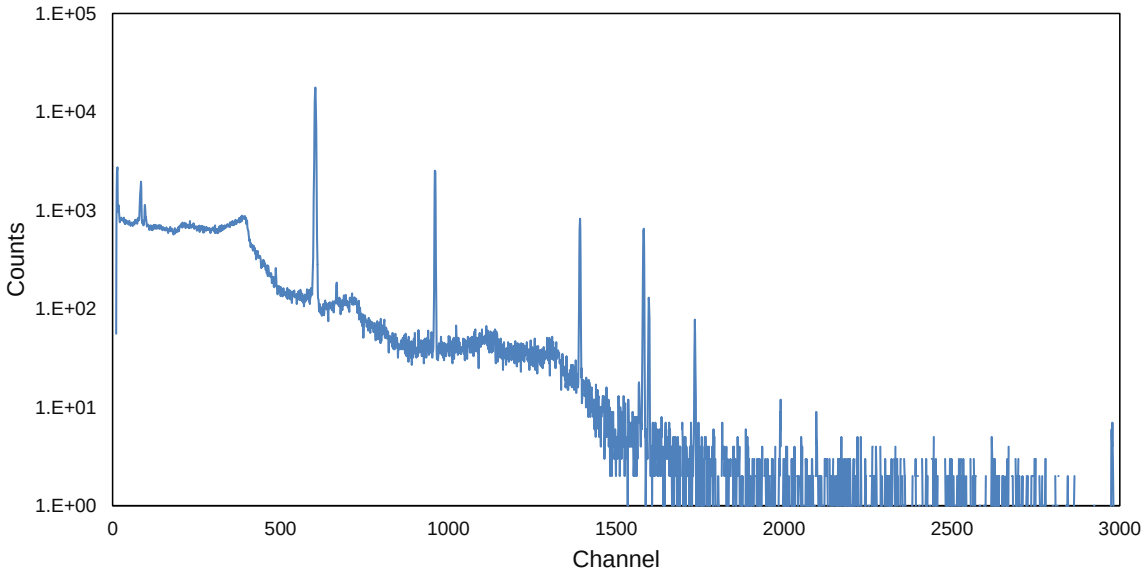

Figure B-4. Gamma ray spectrum of a MEC201 $LiCoO_2$ battery obtained 1 day after the first UMass reactor experiment.

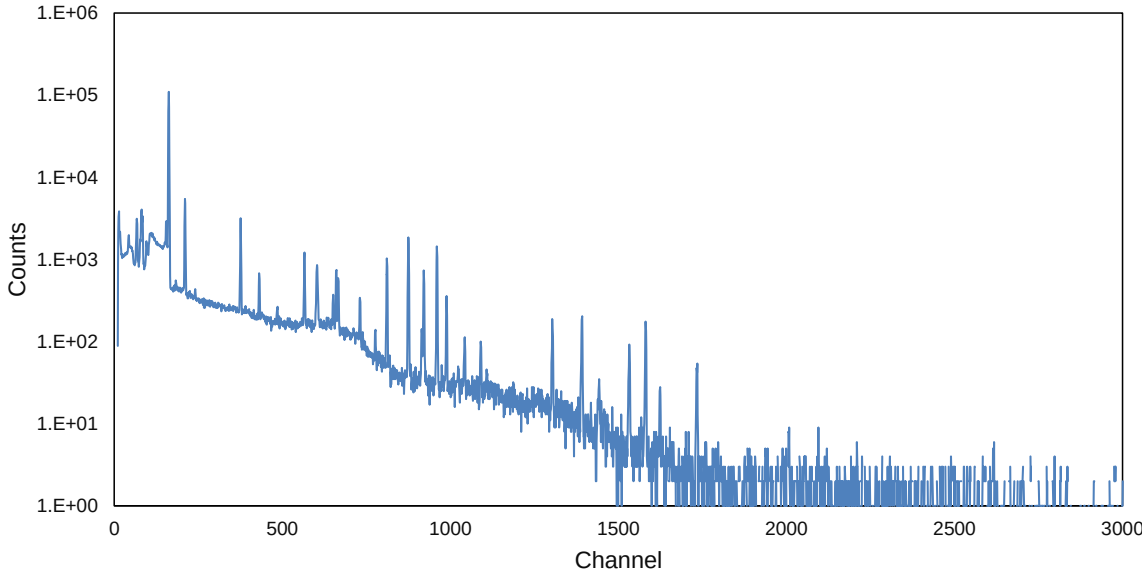

Figure B-5. Gamma ray spectra of a ML-2020 $LiMnO_2$ battery obtained 1 day after the first UMass reactor experiment.

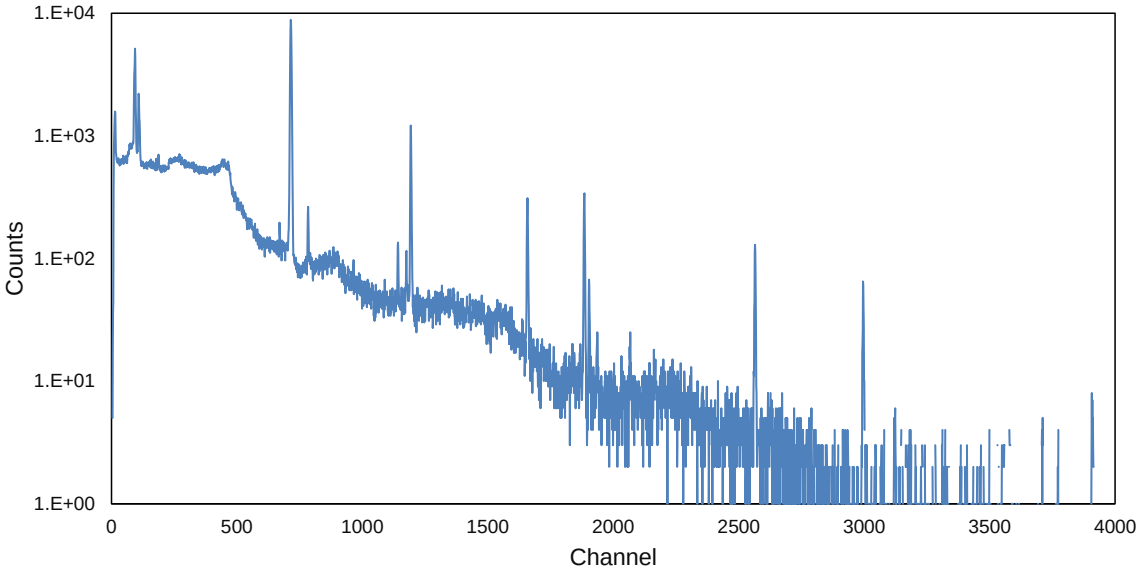

Figure B-6. Gamma ray spectra of a LIR2032 $LiCoO_2$ battery obtained 1 day after the second UMass reactor experiment.

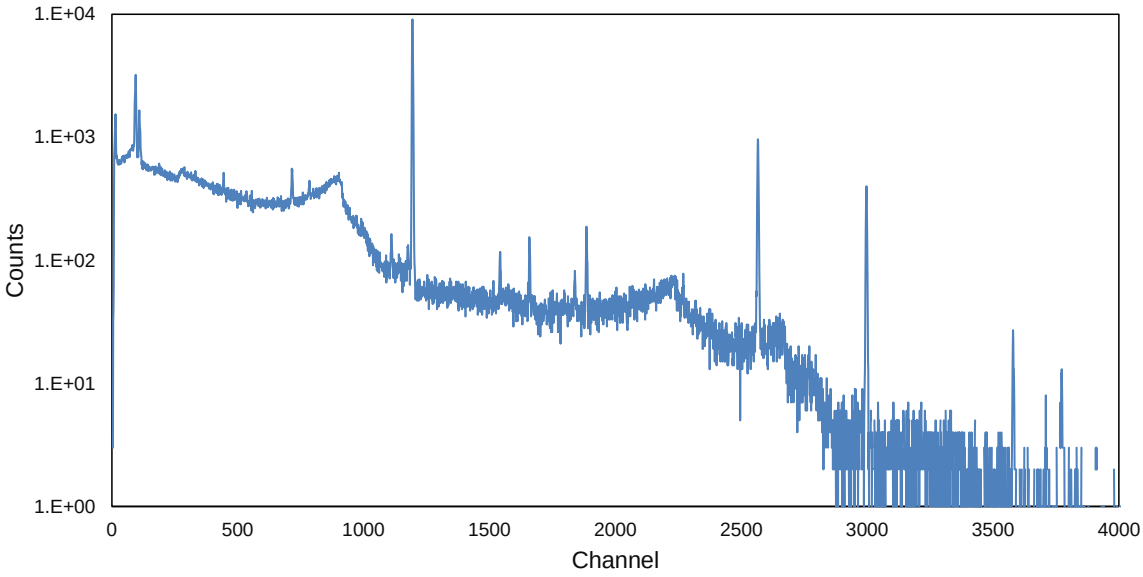

Figure B-7. Gamma ray spectra of a CR2032 $LiMnO_2$ battery obtained 1 day after the second UMass reactor experiment.

APPENDIX C

INDUCED ACTIVITIES FOR BATTERIES EXPOSED IN EXPERIMENTS

C.1. Induced Activities for Batteries Exposed in the First OSU Experiment

Radionuclides	LIR2032 $LiCoO_2$	CR2032 $LiMnO_2$
	Activity (Bq)	Activity (Bq)
Mn-56	1.04E+07	4.95E+08
Fe-59	6.45E+02	9.63E+02
Co-60	1.56E+04	4.75E+02
Cu-64	2.80E+06	2.42E+05

C.2. Induced Activities for Batteries Exposed in the Second OSU Experiment

Radionuclides	LIR2032 $LiCoO_2$	CR2032 $LiMnO_2$
	Activity (Bq)	Activity (Bq)
Mn-56	2.08E+07	5.18E+08
Fe-59	9.44E+02	9.84E+02
Co-60	3.00E+04	3.50E+01
Co-58	8.77E+02	1.70E+02
Na-24	9.32E+03	2.83E+03
Ga-72	2.91E+03	1.49E+03
W-187	1.51E+04	3.53E+02
Cu-64	5.29E+06	1.53E+04
Cr-51	6.85E+04	2.84E+04
As-76	2.23E+03	1.64E+03
K-40	1.20E+03	1.49E+03
Mo-99	7.96E+02	5.18E+01
Sb-122	4.03E+02	1.59E+02

C.3. Induced Activities for Batteries Exposed in the Second UMass Experiment

Radionuclides	LIR2032 $LiCoO_2$	CR2032 $LiMnO_2$
	Activity (Bq)	Activity (Bq)
As-76	1.47E+03	7.22E+02
Co-58	2.53E+02	3.31E+01
Co-60	9.44E+02	4.55E+00
Cr-51	7.88E+02	8.84E+02
Cu-64	1.97E+05	N/A
Fe-59	4.14E+01	3.67E+01
Ga-72	1.82E+03	1.01E+03
Mn-54	1.98E+01	3.42E+01
Mo-99	1.30E+02	N/A
Na-24	3.02E+02	5.40E+01
W-187	4.37E+02	3.77E+02

APPENDIX D

ACTIVITY EQUATIONS DERIVATION

This Appendix shows the derivation of the activity equations for constant neutron flux and impulse neutron flux conditions. The general differential equation in both cases is:

$$\frac{dn_2}{dt} = n_1(0)\Phi(t)\sigma_a^1 - n_2(t)\lambda_2$$

where

n_2 = the number of activation product nuclei,

n_1 = the number of target nuclei,

$\Phi(t)$ = the neutron flux,

σ_a^1 = the microscopic absorption cross section of the target nuclide, and

λ_2 = the decay constant of the activation product.

(1) For constant neutron flux during irradiation:

$$\Phi(t) = \phi$$

Then, perform the Laplace transform and get:

$$sn_2(s) - n_2(0) = \frac{n_1(0)\phi\sigma_a^1}{s} - n_2(s)\lambda_2$$

Since $n_2(0) \approx 0$, therefore,

$$n_2(s) = \frac{n_1(0)\phi\sigma_a^1}{s(s+\lambda_2)}$$

Next, inverse the Laplace transformation to obtain:

$$n_2(t) = \frac{n_1(0)\phi\sigma_a^1}{\lambda_2}(1 - e^{-\lambda_2 t})$$

where *t* is the time since that irradiation starts.

Hence, the activity $A_2(t)$ is

$$A_2(t) \triangleq \lambda_2 n_2(t) = n_1(0)\phi\sigma_a^1(1 - e^{-\lambda_2 t})$$

(2) For an impulse neutron flux:

$$\Phi(t) = \Phi_0\delta(t)$$

where $\delta(t)$ is the Dirac delta function. Therefore,

$$\frac{dn_2}{dt} = n_1(0)\Phi_0\delta(t)\sigma_a^1 - n_2(t)\lambda_2$$

Then, perform a Laplace transform and obtain:

$$sn_2(s) - n_2(0) = n_1(0)\Phi_0(1)\sigma_a^1 - n_2(s)\lambda_2$$

Since $n_2(0) \approx 0$, therefore,

$$n_2(s) = \frac{n_1(0)\Phi_0\sigma_a^1}{s + \lambda_2}$$

Next, take the inverse Laplace transformation to get:

$$n_2(t) = n_1(0)\Phi_0\sigma_a^1 e^{-\lambda_2 t}$$

where *t* is the time since the irradiation occurred.

Hence, the activity $A_2(t)$ is,

$$A_2(t) \triangleq \lambda_2 n_2(t) = n_1(0)\lambda_2\Phi_0\sigma_a^1 e^{-\lambda_2 t}$$